

FABRICATION AND APPLICATION OF
SELF-MASKED SILICON NANOSTRUCTURES
IN DEEP REACTIVE ION ETCHING
PROCESSES

DISSERTATION

zur Erlangung des akademischen Grades

DOKTORINGENIEUR
(DR.-ING.)

vorgelegt am der

Fakultät für Maschinenbau der
Technischen Universität Ilmenau

von Herrn

DIPL.-ING. CHRISTOPH KREMIN

geboren am 10.10.1978 in Erlangen

Einreichung am 9. April 2010

Öffentliche Aussprache am 30. September 2010

Vorsitzender Prof. Dr. rer. nat. habil. Stefan Sinzinger, TU Ilmenau

1. Gutachter (Betreuer) Prof. Dr.-Ing. habil. Martin Hoffmann, TU Ilmenau
2. Gutachter Prof. Dr. rer. nat. habil. Peter Schaaf, TU Ilmenau
3. Gutachter Dr.-Ing. Uwe Schnakenberg, RWTH Aachen

Danksagung

Hiermit möchte ich mich bei allen Personen bedanken, die mich bei der Erstellung dieser Arbeit unterstützten.

Dabei möchte ich mich zunächst bei meinem Betreuer Herrn Prof. Martin Hoffmann bedanken, welcher mir die Möglichkeit gab, die Erforschung des Themas "Siliciumgras" fortzuführen und in Form dieser Dissertation schriftlich zu verfassen. Für seine zahlreichen nützlichen Hinweise und Ratschläge, mit denen er mir dabei zur Seite stand, möchte ich mich herzlich bedanken.

Ich danke auch meinen Kollegen Mike Stubenrauch, Michael Fischer und Dr. Arne Albrecht, die mich dem Thema näherbrachten und mich durch zahllose Diskussionen und Ratschläge während meiner Jahre im Zentrum für Mikro- und Nanotechnologien (ZMN) unterstützten.

Besonderer Dank gebührt Steffen Leopold, Lutz Müller, Angela Keppler sowie Anja Kieseewetter, welche durch verschiedene Untersuchungen maßgeblich an der vorliegenden Arbeit mitwirkten.

Weiterhin gedankt sei Dr. Thomas Kups, Dr. Aniket Thete, Dr. Henry Romanus, Dr. Jörg Petzold, Dr. Gernot Ecke, Dr. Marcel Himmerlich, Dr. Stefan Krischok, Dr. Katja Tonisch und Matthias Mach für ihre freundliche Unterstützung durch die Durchführung verschiedener Messungen sowie für die wissenschaftliche Diskussion und Interpretation der Ergebnisse.

Dank gilt auch Thorsten Sändig, Lothar Dressler und André Hiess, welche mir bei der Instandhaltung und Wartung der Anlagentechnik mit Rat und Tat zur Seite standen.

Einen herzlichen Dank möchte ich den Kolleginnen und Kollegen vom Team ZMN aussprechen. Besonders hervorheben möchte ich Karin Friedel, Birgitt Hartmann und Gabriele Harnisch, welche mir durch ihre praktische Unterstützung und nützlichen Rat halfen, die zahlreichen technologischen Herausforderungen zu meistern.

Weiterhin möchte ich mich auch bei meinen Kolleginnen und Kollegen des Fachgebietes Mikromechanische Systeme und sämtlichen Mitarbeiterinnen und Mitarbeitern des ZMN bedanken. Die Zusammenarbeit war stets geprägt von einem respektvollen und freundschaftlichen Umgang und trägt maßgeblich dazu bei, dass mir die vergangenen Jahre als eine sehr angenehme und schöne Zeit in Erinnerung bleiben wird.

Bei meinen Freunden Roman Mitterer, Knut Schäfer, Thomas Herre, Adam Williamson, Mary Donahue und Dr. Heike Bartsch möchte ich mich für die Hilfe, die Zerstreungen sowie manch nötige Aufmunterung bedanken.

Vor allem danke ich meiner Freundin Elisabeth Steinhagen, welche mich während der gesamten Zeit begleitete, geduldig ertrug und mich auch bei der Fertigstellung der Arbeit unterstützte.

Schließlich möchte ich mich bei meinen Eltern Marie und Horst Kremin bedanken, welche mir nicht nur meine Ausbildung ermöglichten, sondern in jeder Hinsicht und jederzeit hinter mir stehen.

Ilmenau im April 2010

Publications

Parts of this work are already published in:

KREMIN, C.; LEOPOLD, S.; HOFFMANN, M.: Untersuchung zur selbst-organisierten Nanomaskierung in zyklischen Tiefenätzprozessen für die reproduzierbare Erzeugung von nanostrukturiertem Silicium. In: *GMM-Fachbericht Mikro-Nano-Integration/ Beiträge des 2. GMM-Workshops*, Erfurt, Germany, March (2010). - VDE Verlag GmbH Berlin ISSN 1432-3419; ISBN 978-3-8007-3216-6, CD-ROM

KREMIN, C.; LEOPOLD, STEFFEN; STUBENRAUCH, M.; HOFFMANN, M.: Variation von nanostrukturiertem Silicium aus DRIE-Tiefenätzprozessen zur Integration in Si-basierte MEMS. In: *GMM-Fachbericht Mikro-Nano-Integration/ Beiträge des 1. GMM-Workshops*, Seeheim, Germany March (2009). - VDE Verlag GmbH Berlin ISSN 1432-3419; ISBN 978-3-8007-3155-8, CD-ROM

KREMIN, C.; STUBENRAUCH, M.; HOFFMANN, M.: Variations of nanostructured silicon in deep reactive ion etching processes. In: *Proceedings of 19th MicroMechanics Europe Workshop*, Aachen, Germany, September (2008) ISBN 978-3-00-025529-8, CD-ROM

STUBENRAUCH, M.; SCHWANDT, M.; KREMIN, C.; HECHT, S.; HOFFMANN, M.: Statische und dynamische Prüfung von Silizium-Nano-Klettverschlüssen. In: *GMM-Fachbericht Mikro-Nano-Integration/ Beiträge des 2. GMM-Workshops*, Erfurt, Germany, March (2010). - VDE Verlag GmbH Berlin ISSN 1432-3419; ISBN 978-3-8007-3216-6, CD-ROM

Abstract

Silicon Grass is a nano-scale surface modification formed by self-organizing processes in plasma etching. It can be actively used to enable new functionalities or enhance the performance of Micro-Electro-Mechanical-Systems (MEMS), Biological MEMS (BioMEMS) or Micro-Opto-Electro-Mechanical-Systems (MOEMS). Its low-cost generation with standard fabrication equipment makes it a promising research subject.

This doctoral thesis investigates the formation, modification and application of Silicon Grass resulting from the cyclic Deep Reactive Ion Etching (c-DRIE) process. The central goal is the reproducible and controlled generation as well as the selected modification of the Silicon Grass intended for specific applications. Therefore, the work focuses on three main subjects: nanomasking - the self-organized mechanism that initiates Silicon Grass generation, Silicon Grass processing - for controlled structure etching and subsequent modification, and finally the integration and application in MEMS.

In order to investigate the nanomasking process and its influences and to subsequently derive a formation theory for the c-DRIE process, different morphological and chemical studies by Scanning Electron Microscopy (SEM), Atomic Force Microscopy (AFM), X-Ray Photoelectron Spectroscopy (XPS) and Auger Electron Spectroscopy (AES) as well as process analysis methods are used. It is shown that the nanomask consists of carbon-rich, filament-like clusters, whose morphology can be changed by various process parameters.

The reproducible generation of a nanomask in the c-DRIE is based on the controlled abrasion of the inhibiting film in the etching step. This can be achieved by process control via Optical Emission Spectroscopy (OES) which allows for the initiation of nanomasking even for varying process conditions and thus enables the transfer of the process to other systems. Various influences on nanomask formation and morphology are investigated and it is found that the phenomenon of carbon dust formation in C_4F_8 polymerizing plasmas has a profound effect.

Next, Silicon Grass processing, consisting of etching and subsequent modification, is investigated. It is shown that the characteristic geometrical features of the structures undergo significant changes during the process. In addition, depending on the applied process parameters, the resulting profiles and the sidewall morphology of the Silicon Grass can be changed.

Furthermore, the metallization of Silicon Grass by physical vapor deposition and electroless plating as well as the suitability of different Silicon Grass types for mechanical bonding and infrared optical applications are investigated.

Finally, the integration of Silicon Grass in MEMS is discussed. In this discussion, fundamental information about possible integration methods, requirements and limitations are given. These range from recommended technological processes to appropriate instructions for handling and general design rules. The possible integration and practical application of Silicon Grass in MEMS is demonstrated by the fabrication of a thermo-mechanically actuated cantilever.

Kurzfassung

Siliciumgras ist eine nano-skalige Oberflächenmodifikation, welche durch selbstorganisierte Prozesse während des Plasmaätztes hervorgerufen wird. Sie kann genutzt werden, um neue Funktionalitäten zu ermöglichen oder die Effizienz von Mikro-Elektro-Mechanischen-Systemen (MEMS), Biologischen MEMS (BioMEMS) oder Mikro-Opto-Electro-Mechanischen-Systemen (MOEMS) zu verbessern. Diese Eigenschaften in Kombination mit der kostengünstigen Herstellung mit handelsüblichen Ätzanlagen macht sie zu einem vielversprechenden Forschungsthema.

Diese Dissertation untersucht die Herstellung, Modifizierung und Anwendung von Siliciumgras aus dem zyklischen reaktiven Ionentieftätzprozess (c-DRIE). Zielstellung ist dabei sowohl die reproduzierbare und kontrollierte Erzeugung als auch die entsprechende Modifizierung des Siliciumgrases, um es an bestimmte Anwendungen anzupassen. Dabei konzentriert sich die Arbeit auf folgende drei Hauptthemen: den selbst-organisierten Nanomaskierungsprozess, welcher die Herstellung von Siliciumgras initiiert, die Prozessierung von Siliciumgras für die kontrollierte Erzeugung der Strukturen mit ihrer anschließende Modifikation und schließlich die Integration und Anwendung in MEMS.

Um den Nanomaskierungsprozess und seine Einflüsse zu untersuchen und im Folgenden eine Entstehungstheorie für den c-DRIE Prozess abzuleiten, werden sowohl verschiedene morphologische und chemische Analysen mittels Rasterelektronenmikroskopie (SEM), Rasterkraftmikroskopie (AFM), Röntgen-Photoelektronenspektroskopie (XPS) und Auger-Elektronen-Spektroskopie (AES) genutzt, als auch prozessanalytische Verfahren eingesetzt. Es wird gezeigt, dass die Nanomaskierung aus kohlenstoffreichen, filamentartigen Clustern besteht, deren Morphologie über eine Variation von Prozessparametern verändert werden kann.

Die reproduzierbare Erzeugung der Nanomaskierung im c-DRIE Prozess basiert auf dem kontrollierten Abtrag der abgeschiedenen Passivierungsschicht im Ätzschritt. Dies wird durch eine Prozesskontrolle mittels optischer Emissionsspektroskopie erreicht, welche es erlaubt, den Nanomaskierungsprozess selbst bei variierenden Prozessbedingungen zu initiieren und dadurch die Übertragung des Prozesses in andere Systeme ermöglicht.

Es werden verschiedene Einflüsse auf die Entstehung der Nanomaskierung und deren Morphologie untersucht und festgestellt, dass dabei das Phänomen der Kohlenstoffpartikelerzeugung in C_4F_8 polymerisierenden Plasmen eine große Wirkung hat.

Im Folgenden wird die Prozessierung von Siliciumgras, bestehend aus Strukturätzung und anschließender Modifizierung, analysiert. Es wird gezeigt, dass die charakteristischen geometrischen Merkmale der Strukturen signifikanten Veränderungen während des Entstehungsprozesses unterworfen sind. Außerdem können, abhängig von den angewendeten Prozessparametern, die resultierenden Profile und Seitenwandmorphologien des Siliciumgrases verändert werden.

Weiterhin wird sowohl die Metallisierung von Siliciumgras mittels physikalischer Gasphasenabscheidung und stromloser Galvanik als auch die Eignung unterschiedlicher Typen von Siliciumgras für die

Aufbau- und Verbindungstechnik und die optische Anwendung im infraroten Bereich untersucht. Schließlich wird die Integration von Siliciumgras in MEMS beschrieben. Dabei werden grundlegende Informationen zu möglichen Integrationsverfahren, Anforderungen und Einschränkungen gegeben. Sie reichen von empfohlenen technologischen Prozessen bis hin zu Hinweisen für eine angemessene Handhabung oder für das Design von Mikrosystemen mit integriertem Siliciumgras. Eine mögliche Integration und praktische Anwendung von Siliciumgras in MEMS wird anhand eines hergestellten, thermo-mechanisch aktuierten Cantilevers demonstriert.

Table of Contents

Danksagung	III
Publications	V
Abstract	VII
Kurzfassung	IX
Nomenclature	XIII
1 Introduction	3
1.1 Motivation	3
2 Fundamentals	7
2.1 Deep Reactive Ion Etching	7
2.1.1 History	7
2.1.2 Process Description	7
2.1.3 Kinetics	9
2.1.4 Inductively Coupled Plasmas	12
2.1.5 Etching Effects	14
2.2 Silicon Grass - a Self-Organized Nanostructure	18
2.2.1 Discovery and Formation	18
2.2.2 Applications	20
3 Nanomasking - Initiation of Silicon Grass Formation	23
3.1 Formation Theory	23
3.2 Surface Analysis	27
3.2.1 Morphology Analysis	27
3.2.2 Chemical Analysis	31
3.3 Process Analysis	37
3.3.1 Pyrometry	37
3.3.2 Passivation	39
3.3.3 Etching	45

3.3.4	Controlled Nanomasking	51
3.3.5	Parametrical Study	54
3.4	Influences on Nanomasking	61
3.4.1	Carbon Dust Formation and Film Flaking	61
3.4.2	Oxygen	63
3.4.3	Contaminations	64
3.4.4	Masking	65
4	Silicon Grass Processing	67
4.1	Silicon Grass Formation	67
4.1.1	Experimental Set-up and Structure Characterization	68
4.1.2	Structure Development	72
4.1.3	Parametrical Influences	73
4.2	Metallization of Silicon Grass	78
4.2.1	Physical Vapour Deposition	78
4.2.2	Electroless plating	82
4.3	Adapted Silicon Grass	85
4.3.1	Silicon Grass for Packaging	86
4.3.2	Silicon Grass for Infrared Applications	89
5	Silicon Grass in Micro-Electro-Mechanical-Systems	93
5.1	Integration of Silicon Grass	93
5.1.1	Recommended Technological Processes	94
5.1.2	Health Hazards and Handling Instructions	97
5.2	Feasibility Test - A Thermo-Mechanical Actuator with Integrated Silicon Grass	99
5.2.1	Actuator Performance	100
5.2.2	Influence of Silicon Grass on the Thermal Properties and Performance	104
5.2.3	Technology	108
6	Summary and Outlook	111
6.1	Summary	111
6.2	Outlook	113
	Bibliography	115
	List of Figures	127
	List of Tables	129
	Appendix	129

A	Flowchart Cantilever	131
B	Chemicals	137
C	Theses	139
C.1	Theses	139
C.2	Thesen	141

Nomenclature

Abbreviations

AC	alternating current
AES	Auger Electron Spectroscopy
AFM	Atomic Force Microscopy
ARDE	Aspect Ratio Dependend Etching
ASE[®]	Advanced Silicon Etching
BioMEMS	Biological Micro-Electro-Mechanical-Systems
CCP	capacitatively coupled
c-DRIE	Cyclic Deep Reactive Ion Etching
CMOS	Complementary Metal Oxide Semiconductor
DoE	Design of Experiments
DRIE	Deep Reactive Ion Etching
EADF	electron angle distribution function
FIR	far infrared
HF	high frequency
IADF	ion angle distribution function
ICP	inductively coupled
LWIR	long-wavelength infrared
MEMS	Micro-Electro-Mechanical-Systems
MOEMS	Micro-Opto-Electro-Mechanical-Systems
NIR	near-wavelength infrared
OES	Optical Emission Spectroscopy
PECVD	Plasma Enhanced Physical Vapour Deposition
PVD	Physical Vapour Deposition
RCA	Radio Corporation of America
RF	radio frequency
RIE	Reactive Ion Etching
SEM	Scanning Electron Microscopy
SOI	Silicon on Insulator
STS[®]	Surface Technology Systems

SWIR	short-wavelength infrared
TADTOP	Trench Area Dependent Tapering of Profiles
TEM	Transmission Electron Microscopy
TSV	Through-Silicon-Vias (Technology)
UHV	ultra high vacuum
UV	ultraviolet
VIS	visible spectrum
XPS	X-Ray Photoelectron Spectroscopy

Symbols

α	attenuation coefficient, thermal expansion
β	scattering angle
ΔT	difference in temperature
λ	thermal conductivity
Λ	thermal conductivity ratio
ν	<i>Poisson</i> number
ϕ	heat flow
Φ	frequency ratio
ρ	density
σ	tensile strength
τ	time constant
τ_{crit}	critical etch step time
τ_{dep}	deposition step time
τ_{etch}	etch step time
τ_{opt}	etch step time optimum
Θ	contact angle
A	area
\mathcal{A}	absorption
a_i	model parameters
AR	aspect ratio
c	specific heat
c_i	model constants
C_{th}	thermal capacity
D	element density
D_w	wafer diameter
e	surface enlargement factor
E	<i>Young's</i> modulus
e_i	model parameters (etching)

f	frequency
h, \bar{h}	height, mean height
k	extinction coefficient
l	length
p	pressure
P_b	bias power
P_c	coil power
p_i	model parameters (passivation)
Q	flow rate
R, r	radius
R^{-1}	deflection
R_a	average roughness
R_{dep}	deposition rate
R_{etch}	etch rate
R_{FC}	fluor to carbon ratio (FC-ratio)
R_t	maximum height of profile
R_{th}	thermal resistance
R_w	wafer resistivity
\mathcal{R}	reflection
S	selectivity
s	distance
t	thickness
T	temperature
t_W	wafer thickness
\mathcal{T}	transmission
U_b	bias voltage
u_i	input parameters
V	area coverage
V_{AE}	ratio of etched area to wafer area
w	width
x	output parameter
\bar{x}	mean distance
z	height, depth
z_{dep}	deposited film thickness
$z_{etch,inh}$	etch yield of inhibiting film

1 Introduction

1.1 Motivation

The discovery of the macroscopic effects of nanometer-sized structures has led to a great popularity of Nanotechnology in the last couple of years. Nano-structures exhibit unique properties, which enable new functionalities (e.g. Lotus Effect) or enhance the performance of existing devices (e.g. catalysts). These effects have become a subject of international research and have brought about the development and commercialization of various techniques of surface engineering and technology. The machined materials vary from metals to semiconductors, polymers and glasses. However, even though the fundamental research in the complex field of Nanotechnology is advanced, the marketability is still on the way to reach its full potential. One of the reasons for this is that there is often a lack of ideas and means for an intelligent integration in common devices.

An integration of nano-scale features in microsystems can provide a way to tap the capabilities of 'Nano' via the established Microtechnology. Here, the surface modification Silicon Grass is a good example for this 'Micro-Nano-Integration'. It is generated in Reactive Ion Etching (RIE) processes by a self-masking mechanism, which provides an alternative, cost-efficient way to fabricate nano-structured *Si* surfaces directly in the Micro-Electro-Mechanical-Systems (MEMS) fabrication process, without the use of high-resolution lithography. Due to its appearance and optical properties the structure is called 'Silicon Grass' or 'Black Silicon' and can be described as an artificial surface roughness consisting of a high density array of needle-like features. It leads to remarkable physical and chemical properties of the surfaces.

The effect of artificial surface roughening in RIE processes was discovered in the 1980's, during the rise of plasma processing techniques for semiconductor manufacturing. In most publications the roughening is described as an unwanted side effect since it strongly affects the etching and prevents accurate fabrication. Hence, the studies deal with strategies for an effective prevention of this surface roughening.

In 1995 JANSEN *et al.* published the so-called Black Silicon Method [JDLE95], a useful procedure to optimize highly anisotropic RIE processes. Here, Black Silicon is utilized as an indicator to find the optimal process conditions. Despite the indirect use of the structures, the prevention of surface roughness is ultimately intended. However, over time more applications of the surface structure emerged.

Today's applications range from opto-electronics (e.g. silicon solar cells, optical sensors) and functional elements in microfluidics or biosensors to new techniques for micro- and nanointegration. With the rising number of these new applications and the advancements in plasma etching, the demand for reproducible generation and control of the geometry has been steadily increasing.

In contrast to RIE, the investigated cyclic Deep Reactive Ion Etching (c-DRIE) of silicon (Si) does not use a continuous process, but switches between two states of Si etching and the deposition of a passivating film. This passivating film prevents the lateral undercutting of the features and guarantees a highly anisotropic etch into depths of several hundreds of microns at high etch rates. This turns the c-DRIE process into one of the most important bulk Si etching techniques.

The formation of Silicon Grass is also observed in c-DRIE processing, but the initiating mechanism, the appearance of a so-called nanomask (also referred to as micromask), is significantly different from the well-known RIE. The resulting Silicon Grass also exhibits different geometrical and chemical properties. To the human eye the Silicon Grass from RIE process appears black, while the one from c-DRIE processes has a grayish or greenish color. This is why, within this work, the RIE Silicon Grass is referred to as Black Silicon while the term Silicon Grass is used to describe the surface modification in general.

Because of the improved capabilities of process control in the c-DRIE process and the resulting advancement of selectivity, anisotropy and profile control, producing Silicon Grass with a wide range of possible geometries is feasible. Therefore, the reproducible and simple generation of Silicon Grass via the established c-DRIE process is of considerable interest.

This is where this work starts.

Goals and Structure of the Work

The goal of this work is to deepen the understanding of the initiating mechanisms for Silicon Grass formation in the c-DRIE process. It shall provide a basis to enable a reproducible and controlled generation of the surface modification, even for varying process conditions. Therefore, various material analysis methods and experiments are performed to gain information about the mechanisms involved. The findings are subsequently used to derive a formation theory of nanomasking in c-DRIE processes (Chapter 3).

The following objective is to enable a process control of Silicon Grass in order to be able to adjust, optimize and modify the structures for selected applications. Hence, experimental studies are performed to identify relevant process parameters and analyze their influence on the formed Silicon Grass structures. As a subsequent modification, the metalization of Silicon Grass by physical vapor deposition

and electroless plating are investigated. Finally, different Silicon Grass types are used to evaluate their adaptability and applicability for two exemplary applications (Chapter 4).

Furthermore, the goal is to provide information on the integration of Silicon Grass in MEMS and demonstrate a successful application. Therefore, general information on requirements and limitations as well as recommended technological processes, handling instructions and design rules are discussed. As an example, a thermally actuated microcantilever with integrated Silicon Grass is presented (Chapter 5).

Finally the results are summarized and an outlook is given with suggestions for future works on the subject (Chapter 6).

2 Fundamentals

In this Chapter the fundamentals concerning this work are discussed. At first, the basics of the c-DRIE process (Section 2.1) are covered. It is the fabrication method used for the self-organized nanostructure Silicon Grass. In Section 2.2 information about Silicon Grass characteristics, is given.

2.1 Deep Reactive Ion Etching

2.1.1 History

RIE of *Si* plays a decisive role for Micro-Electro-Mechanical-Systems (MEMS). It allows for the realization of mechanical sensor structures of highly integrated sensor elements. For corresponding circuit fabrication, standard Complementary Metal Oxide Semiconductor (CMOS) techniques are used.

Cyclic Deep Reactive Ion Etching (c-DRIE) is an advanced RIE process and was originally developed at the beginning of the 1990's by F. LAERMER and A. SCHILP, employees of Robert Bosch GmbH. The process was later patented by the company in 1996 [LS96] and therefore became known as the 'Bosch-Prozess' among experts. After this, the process was further developed by employees of Surface Technology Systems (STS) and Alcatel Vacuum Technology and gained marketability. Since 1997, STS has distributed the process with the appropriate equipment under the trademark Advanced Silicon Etching (ASE®).

The process is mainly used to generate high aspect-ratio structures up to hundreds of microns in height to manufacture micromechanical sensor structures, electrostatic microactuators or holes for the so-called Through-Silicon-Vias (TSV) technology. Compared to RIE, it has a better performance with respect to etch rate, anisotropy, selectivity and process control.

2.1.2 Process Description

The c-DRIE is a dry etching plasma process that anisotropically structures *Si* without dependence on the crystal orientation of the *Si*. Reduced damage by high energy ions, high aspect ratios (> 100) [MRS⁺05], high etch rates ($> 20 \mu\text{m min}^{-1}$) [JBU⁺09], large etching depths ($> 500 \mu\text{m}$) [KF99a] and high selectivities are realized.

Common mask materials are different types of photoresists or thermally grown silicon dioxide (SiO_2). Other materials (e.g. metals or nitrides) are also used depending on the actual requirements of the

setup (e.g. material compatibility, layer thicknesses, selectivity).

The process consists of two repeating steps: passivation and subsequent etching. Sidewalls are protected from a lateral undercut by the passivating film, which permits high aspect ratios. The commonly used precursor gases are sulfur hexafluoride (SF_6) in combination with oxygen (O_2) for the etching and octafluorocyclobutane (C_4F_8) for the passivating step. In both steps argon (Ar) can be added to dilute the reactive gases. Figure 2.1 gives a schematic of the process sequence. During the first process

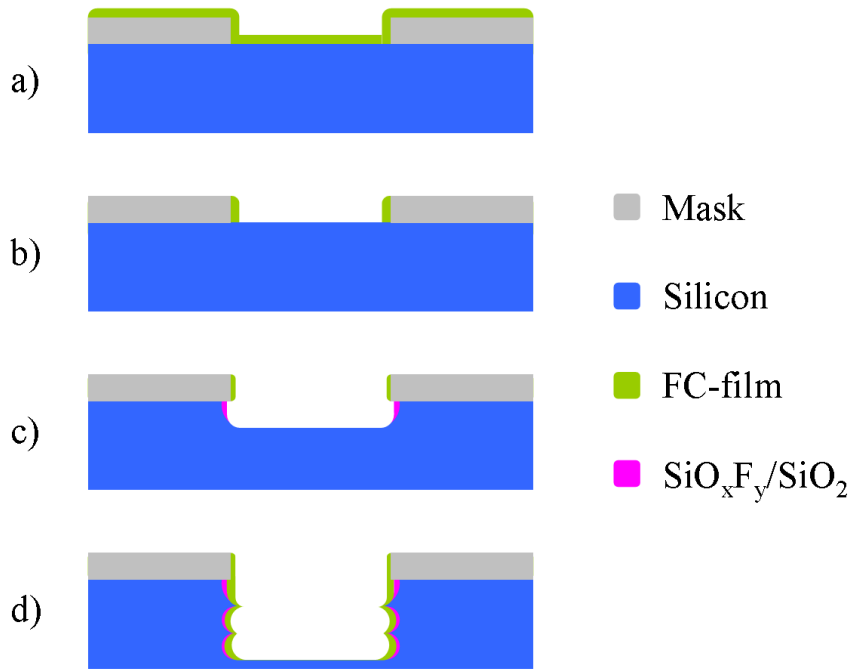


Figure 2.1: c-DRIE process sequence.

step a thin passivating film is isotropically deposited on the substrate, uniformly covering the masked structures, see Figure 2.1 a). The subsequent etching is a combination of a chemical and a physical part, where the physical component is more effective at the beginning of the etching step, see Figure 2.1 b). The directional sputtering of high energy ions leads to an anisotropic removal of the passivating film and an increase in temperature on the horizontal areas. This enhances the chemical etching of the affected areas and leads to an increase of the isotropic component, see Figure 2.1 c). It is noted that due to the oxygen addition in most SF_6 plasmas, a secondary passivation effect occurs during etching. This passivation film consists of SiO_xF_y and SiO_x . The process consists of the described steps, which, through their periodic cycling, lead to the appearance of the characteristic scallops on the sidewalls, see Figure 2.1 d). A SEM image depicting these scallops in trench and hole etching is shown in Figure 2.2. If smooth sidewalls are needed, this scalloping is a disadvantage of c-DRIE but it can be reduced by adequate process control [VHHR99].

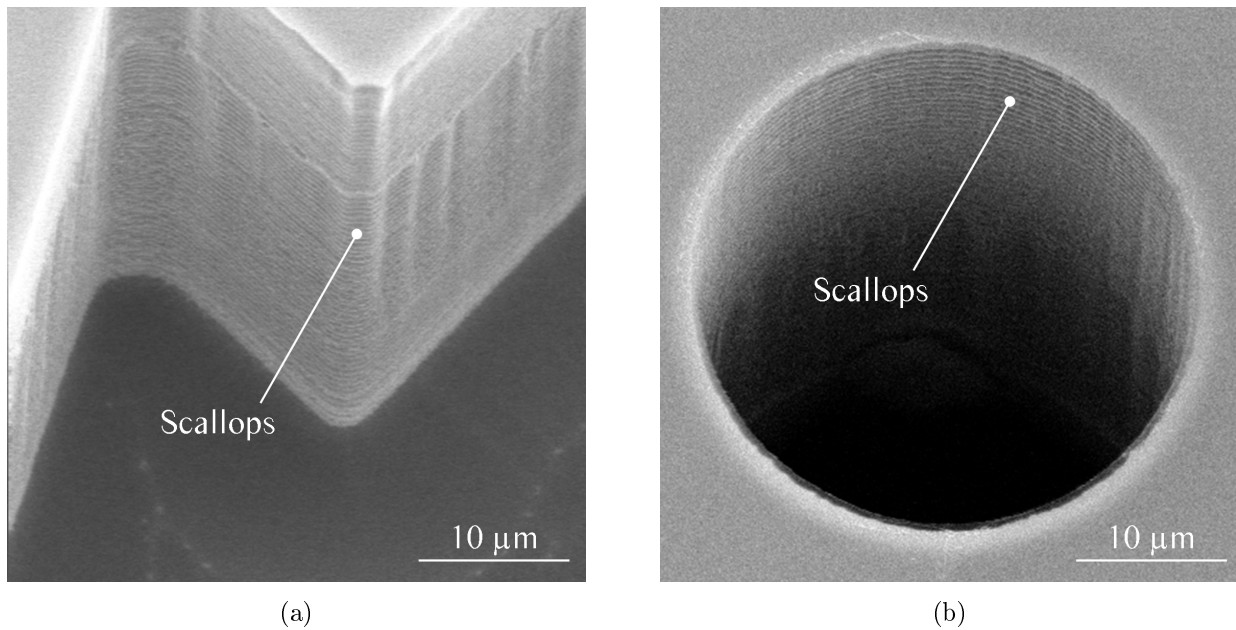
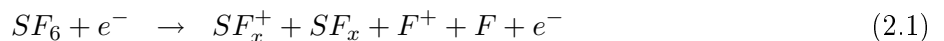


Figure 2.2: c-DRIE scalloping in a) trench and b) hole etching.

2.1.3 Kinetics

Generally, fluorine-based precursor gases are used for the dry etching of *Si*. Primarily, SF_6 and tetrafluoromethane (CF_4) are used. Chlorine-based gases have also been widely utilized but bear reduced selectivity and low etch rates and thus remain the exception for the deep structuring of *Si*. The following kinetic description after [AML86] and [RP90] concentrates on SF_6 in combination with O_2 for etching and C_4F_8 for passivation.

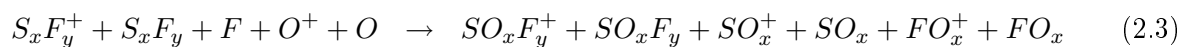
Fluorine radicals are generated by electron impact dissociation of SF_6 within the plasma. Simultaneously, different kinds of ions and neutrals are being formed by ionization, dissociation, recombination and excitation reactions. The formation of negative ions by recombination or electron attachment reactions is also possible but is neglected in this consideration:



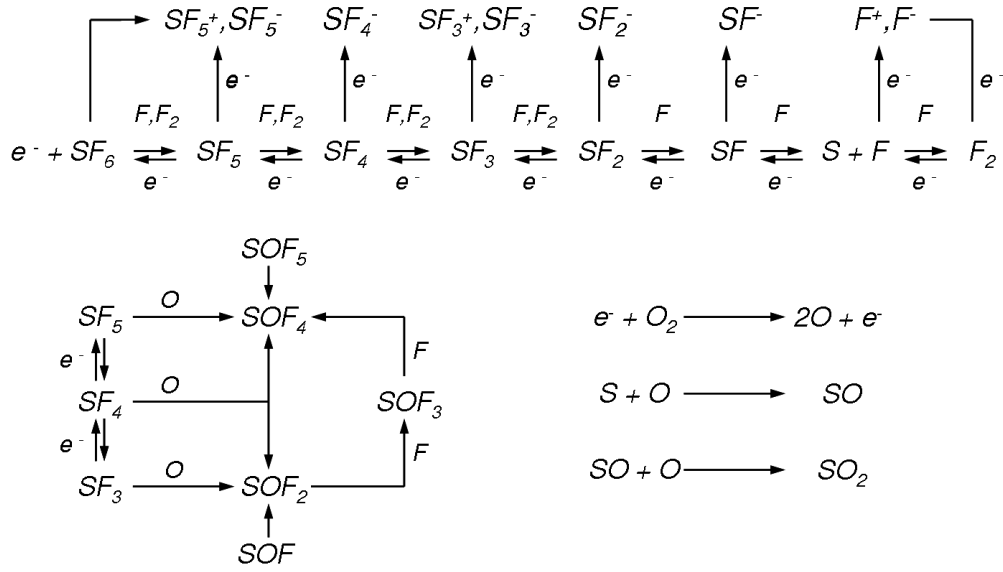
A dissociation of O_2 also takes place:



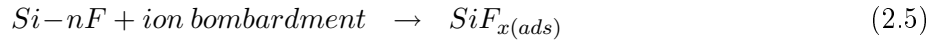
The reaction products can further react with each other and form SO_xF_y , SO_x and FO_x molecules:



The following Figure 2.3 schematically depicts the main reaction paths for plasmas of SF_6 and SF_6 with O_2 addition: The *Si* is etched by radical reactions with the generated atomic fluorine (F). Gaseous

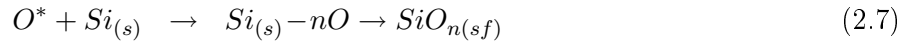

 Figure 2.3: Main reaction paths of SF_6/O_2 plasmas [AML86].

products (e.g. silane SiF_4) are formed:



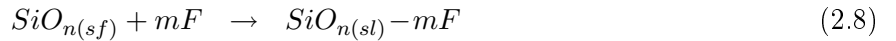
The indices (ads) and (gas) account for the surface bound state and the unbound, gaseous state of the molecule, respectively.

In addition to the chemical abrasion of Si , there is also the continuous formation of a passivating SiO_2 film by the reaction of oxygen with the Si surface:

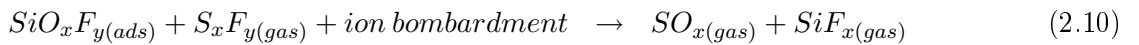
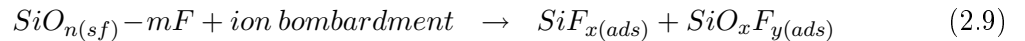


Here, the indices (s) and (sf) account for surface and surface film, respectively.

The subsequent fluorination of this SiO_2 film leads to the formation of silicon oxyfluoride (SiO_xF_y):



Ion-assisted chemical etching by F and S_xF_y removes this SiO_xF_y film:



It is because of these reaction kinetics that anisotropic etching with SF_6 and O_2 can be achieved. The simultaneous deposition and removal of the passivating film have to be carefully adjusted to guarantee

good control of the anisotropy. This is hampered by the physical and chemical boundary conditions (e.g. gas transport, redeposition) of the reactions which consistently change with increasing etch depth. Therefore, other precursor gases like polymer formers (e.g. CF_4 , CHF_3) or hydrogen (H_2) are introduced to assist. High ion energies (several hundred eV) are needed to remove the passivation film inside deep trenches. Standard photoresist materials have poor selectivity under heavy ion bombardment and thus SiO_2 or metals are preferred as mask material for deep etching ($> 100 \mu m$) in RIE.

The cyclic nature of the c-DRIE process allows for advanced process control, since the adjustment of deposition and removal of the passivation film is possible.

Next to C_4F_8 , other fluor-carbon gases like hexafluoropropene (C_3F_6 , $CF_2=CF-CF_3$), hexafluoro-1,3-butadiene (C_4F_6 , $CF_2=CF-CF=CF_2$) or octafluorocyclopentan (C_5F_8) can be utilized. Depending on the characteristics of the precursor gas (e.g. fluor-carbon ratio, saturated/unsaturated state), different passivation properties are found (e.g. the difference in passivation between C_4F_6 and C_4F_8 reported in [RKK⁺08]). In [KGCG08] an extensive reaction model is presented, which covers a great amount of gas phase reactions and surface reactions. The main reactions of the passivation process are given below.

C_4F_8 is fractionated by electron impact dissociation:

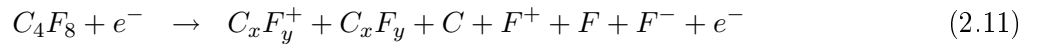


Figure 2.4 schematically depicts the main reaction paths: The different C_xF_y molecules adsorb on the

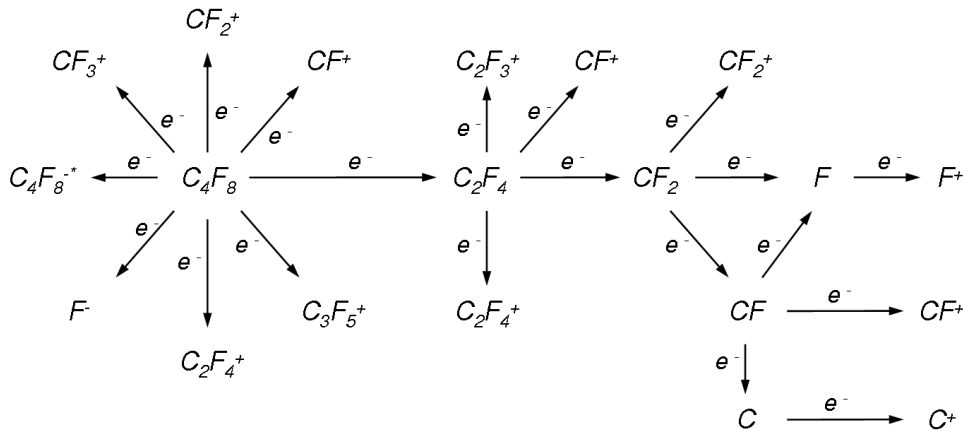
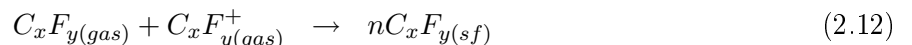
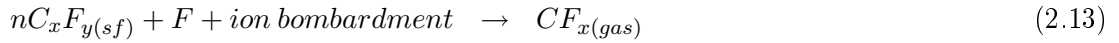


Figure 2.4: Main reaction paths of C_4F_8 plasmas [VLOK04].

surface of the substrate and form a teflon-like fluor-carbon film (FC-film):



This FC-film is continually removed by physical sputtering and ion-assisted chemical reactions with F and O [dAg90]:



The morphological and chemical changes of the FC-film during its removal play an important role in this work and are therefore studied in greater detail in Chapter 4.

2.1.4 Inductively Coupled Plasmas

In c-DRIE processing, inductively coupled plasmas (ICP) are used. The plasma is generated by an high-frequency (HF) electromagnetic field (commonly $13,56\text{ MHz}$), which is induced inductively by a coil surrounding or on top of the reactor. Figure 2.5 shows two typical coil configurations in cylindrical and planar arrangements. This non-capacitative coupling of power through a dielectric chamber material

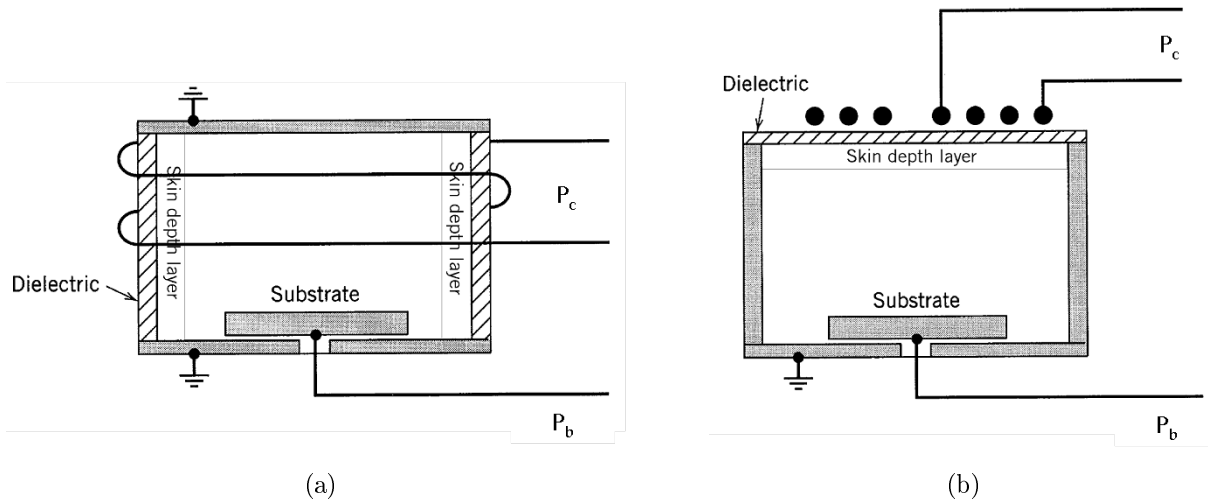


Figure 2.5: a) Cylindrical and b) planar ICP coil configuration [LL05].

results in a low voltage drop across the debye sheaths at the electrode and the chamber walls, bringing about lesser acceleration for the incident bombarding ions. To control the ion energy, the substrate electrode is powered separately by a second HF source. This configuration enables independent control of ion and radical densities (by coil power P_c) and kinetic energy of the bombarding ions (by bias power P_b). The independent control and the achievable high plasma densities ($10^{11} < n_0 < 10^{12}\text{ cm}^{-3}$) which are five to ten times greater than capacitatively coupled RIE reactors, are the basis for the high etch rates, good anisotropy and profile control.

Because no large-area counter electrode is used and the voltage drop across the debye sheaths is low, the effect of contaminants from sputtered chamber material or deposits of former processes is reduced,

making ICP reactors also a preferred tool for plasma-enhanced chemical vapor deposition. In these processes, high plasma purity plays an important role for the generation of defect-free films.

For the experiments in this work, an ICP-multiplex from Surface Technology Systems has been used, see Figure 2.6. An overview of the system parameters is given in Table 2.1. In addition to the

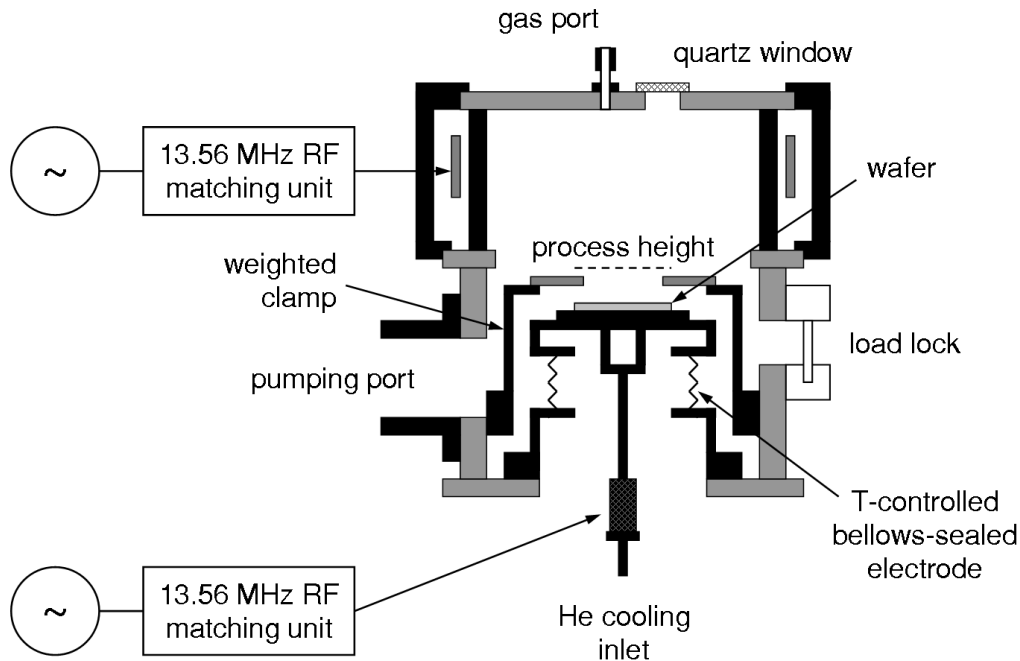


Figure 2.6: ICP-multiplex from STS.

Table 2.1: System parameters.

Parameter	Passivation	Etching
C_4F_8 gas flow ($Q_{C_4F_8}$) (sccm)	0 – 200	-
SF_6 gas flow (Q_{SF_6}) (sccm)	-	0 – 300
O_2 gas flow (Q_{O_2}) (sccm)	-	0 – 100
Coil power (P_c) (W)	0 – 1000	
Bias power (P_b) (W)	0 – 300	
Pressure (p) (Pa)	0 – 13.3	
Chamber temperature (T_S) ($^{\circ}C$)	40	
Substrate temperature (T_C) ($^{\circ}C$)	10 – 30	

controlled input parameter coil and electrode power, pressures, flow-rates, temperature and time constants, several boundary conditions have an effect on the process. These conditions are for example: chamber geometry, chamber conditioning, substrate and mask material and the geometry of the mask.

Furthermore, the change in physical and chemical conditions during the ongoing etch also affects the process. Finally, perturbations by hysteresis or instabilities can occur and pose a challenge for process control. This is especially the case for the c-DRIE where, due to the quick exchange of process gases and pressure, the source power network must compensate for the corresponding change in system impedance.

2.1.5 Etching Effects

A number of publications deal with the study and explanation of etching effects in c-DRIE processes that cause deviations from the desired geometry. These effects originate from the given and varying physical and chemical boundary conditions during etching. Two of the most important phenomena responsible for these deviations are related to transport and consumption of the precursor gases (referred to as loading) or electrical charging of the etched structures. In the following section, the most relevant of these effects are discussed. A distinction between the causal phenomena and the resulting effects must be made, since some of the described effects are caused by multiple phenomena occurring simultaneously.

Loading

The loading effect describes the dependency of etch rates on the etched surface area (Macroloading) or on local element density (Microloading) [VHKR01]. It is caused by the faster depletion of reactive species at etched surface areas in combination with the given gas flow of the chamber. The effect can be reduced by supplying sufficient precursor molecules.

A radial alteration of etch rate, often referred to as the ‘Bullseye effect’, is often related to the effect of Macroloading. Other explanations are inhomogeneous substrate cooling or radially varying plasma densities due to a non-uniform plasma generation, which are found in ICP reactors with cylindrical coil configurations. Figure 2.7 shows the radial variation of etch rate R_{etch} of the STS ICP-multiplex used for this work for different ratios of etched area to wafer area V_{AE} .

RIE-Lag

One of the most prominent effects is the so-called RIE-lag, which can be included in the group of Aspect Ratio Dependent Etching (ARDE) effects. It designates the faster (negative lag) or slower (positive lag) etching of trenches in comparison to neighboring wider ones [LJW06] [Kii00] [KF99b] [KF99a] [JdE96] see Figure 2.8. In the following multiple theories are given to explain this effect.

The positive RIE-lag is caused due to the reduced radical and ion flow with increased aspect ratio and the subsequent depletion of reactive species inside of the etched trenches [CW89]. This effect is most significant at high pressures and temperatures, where the isotropic component, and thus the lateral etch of the sidewalls, leads to this faster depletion at the upper part of the trench. Furthermore,

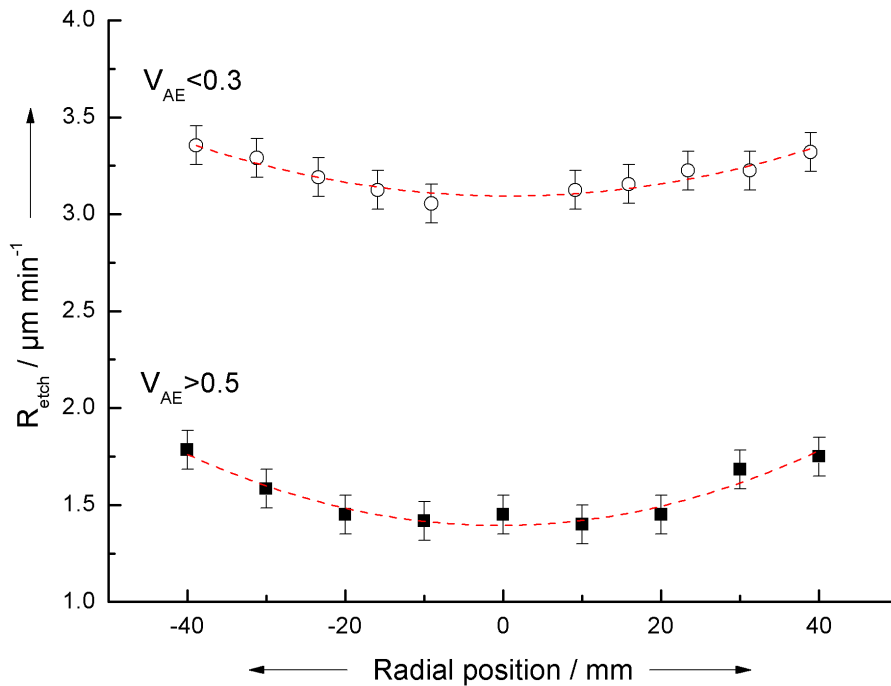


Figure 2.7: Radial variation of etch rate of the ICP-multiplex.

incident angular ions are obstructed by the mask and the sidewalls of the trenches (Ion Shadowing), while the incident vertical ions are deflected towards the negatively charged sidewalls (Charging) and are likewise not able to reach the bottom of the trench.

The negative RIE-lag for *c*-DRIE (also called inverse RIE-lag), is described in [CC04]. Here, the high concentration of C_xF_y radicals and the simultaneous reduction of $S_xF_y^+$ Ions at high process pressures are given as an explanation. They lead to an enhanced passivation at the bottom of wider trenches causing a delayed onset of chemical etching in the subsequent etching step resulting in a slower progression of the etch.

Bowing and TADTOP

Bowing and Trench Area Dependent Tapering Of Profiles (TADTOP) are caused by electrical surface charging of dielectric materials (e.g. SiO_2 etch mask, FC-film). The disparity between the Electron and Ion Angular Distribution Function (EADF/ IADF) lead to an uneven charge distribution inside the etched trenches. Due to the broader distribution of the EADF compared to the IADF, a significant amount of angular electrons is obstructed by the sidewalls, and thus is unable to reach the trench bottom. This results in a positively charged bottom and a negatively charged upper portion of the sidewalls. These charges affect incoming ions which are deflected towards the sidewalls. A negatively

tapered profile is caused (bowing). The influence of the trench width (aka. critical dimension) on bowing is referred to as TADTOP [JdE96]. Here, the charges on the sidewalls of smaller trenches attenuate or even cancel each other, thereby reducing the effect. Figure 2.8 a) gives an example of both types of RIE-lag as well as bowing. The negative RIE-lag in the outermost trench on the left is explained by the differing flank angles of the photoresist mask.

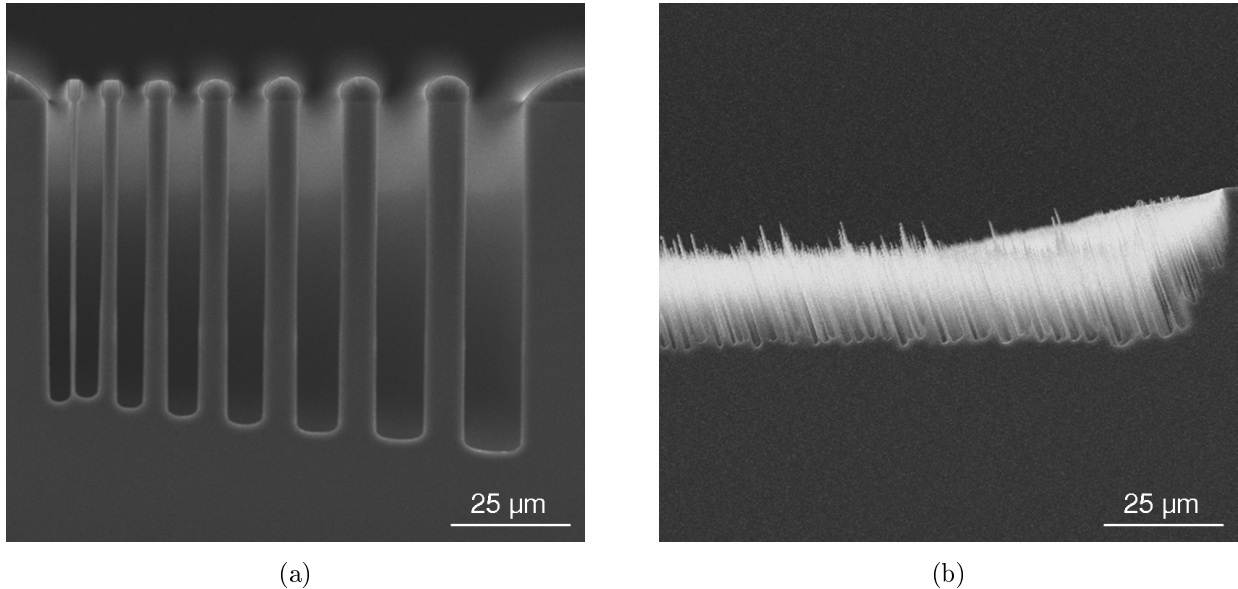


Figure 2.8: a) RIE-lag and Bowing, and b) Tilted Silicon Grass

Trenching and Notching

Likewise bowing and TADTOP, trenching and notching are caused by the uneven distribution of charge inside the structure. That is why these effects often occur simultaneously. During the etching of low-doped *Si* or the incomplete removal of the FC-film, a pronounced positive charge can build up on the trench bottom, because the accumulated charges are not drained. While incident ions are deflected to the sides hitting the sidewalls or their base point, non-reacted, scattered angular ions are also hitting this spot, causing a characteristic curved trench bottom.

Notching is observed in etching Silicon On Insulator (SOI) substrates and occurs at the moment when the dielectric layer is reached [HG97]. The mechanism is basically the same as described above but the deflection of the ions can get so intense that ions perpendicularly hit the sidewalls causing a characteristic profile ('elephant foot').

Bottling

Bottling is mainly observed at higher process pressures and is ascribed to ion shadowing and a sharpening of the IADF inside the trench. The frequent contact of angular ions with the sidewalls leads to

a high reaction probability of these species, thus depleting them rapidly. At a certain aspect ratio and critical angle, scattering and sticking become more probable and a change in profile occurs [JdE96].

Tilting

The tilting effect describes the tilted etching of trenches. It is related on the one hand to the distortion of the electromagnetic field by the clamp ring or other peripherals, on the other hand on local differences of radical densities in the gas flow. Figure 2.8 b) shows the effect of tilting on Silicon Grass.

2.2 Silicon Grass - a Self-Organized Nanostructure

A multitude of methods to fabricate micro- and nanostructured silicon surfaces are described in literature. They can be classified into organized and self-organized methods. Here, the term 'organized' describes a fabrication method where fundamental geometrical properties (e.g. shape, arrangement and density) are defined by an additional process step (e.g. lithography). In the context of this work, the term 'self-organized' is used to designate a process where the complexity of the structures is not directly managed by an outside source, but arises from physical and chemical principles dominating the system. The advantage of self-organized fabrication is the abandonment of additional techniques to define the geometries and consequently the independence from limiting factors of these techniques (e.g. resolution). However, the possible geometries of self-organized structures are given by in-process relations and interactions and therefore are mostly limited and difficult to control. In respect to plasma processes, the complexity of internal interrelations, effects and interference factors of a system can lead to instabilities, fluctuations or even breakdown, preventing a reproducible fabrication process.

Silicon Grass is a surface modification consisting of a high density array of needle-like nanostructures, created in a self-organized process. The phenomenon is originally described as an unwanted side-effect of RIE etching. Since the middle of the 1990's, this special form of surface roughness has successfully been used for various applications

2.2.1 Discovery and Formation

The effect of roughening of silicon surfaces in RIE processes was already described in the middle of the 1980's [RTM⁺86] [OSJ86]. Because of the microscopic appearance and the low reflectivity in the visible spectrum, the terms 'Silicon Grass' and 'Black Silicon' were established. Figure 2.9 shows typical Silicon Grass from RIE and c-DRIE processes. In several studies that followed, different theories about the origin of Silicon Grass were developed and discussed. The majority discussed the occurrence of a so-called nanomask (also referred to as micromask) as explanation for the origination of the structures. Depending on processes and systems, this nanomask is caused by different mechanisms. In chlorine-based RIE, the nanomask is found to consist of redeposited, oxidized etch products [ORP90] or of hydroxyl groups (SiOH) [TSFG89]. Furthermore, sputtered material from masks, electrode, chamber, clamping mechanism or general chamber contamination are determined to be responsible. An increased aluminum (*Al*), *O* and *F* concentration is detected by Auger Electron Spectroscopy (AES) within the nanomask, proving sputtering of chamber materials to have a significant effect [OSJ86]. In [RTM⁺86] clusters of aluminium oxide (Al_2O_3) and SiO_2 are cited.

Another formation mechanism is presented in [HSUM98], where Silicon Grass formation in bromine-based plasmas is studied. Here, interstitial oxygen atoms inside the silicon substrate are assumed to be nucleation zones for the nanomask, since a distinct dependence of structure density on oxygen

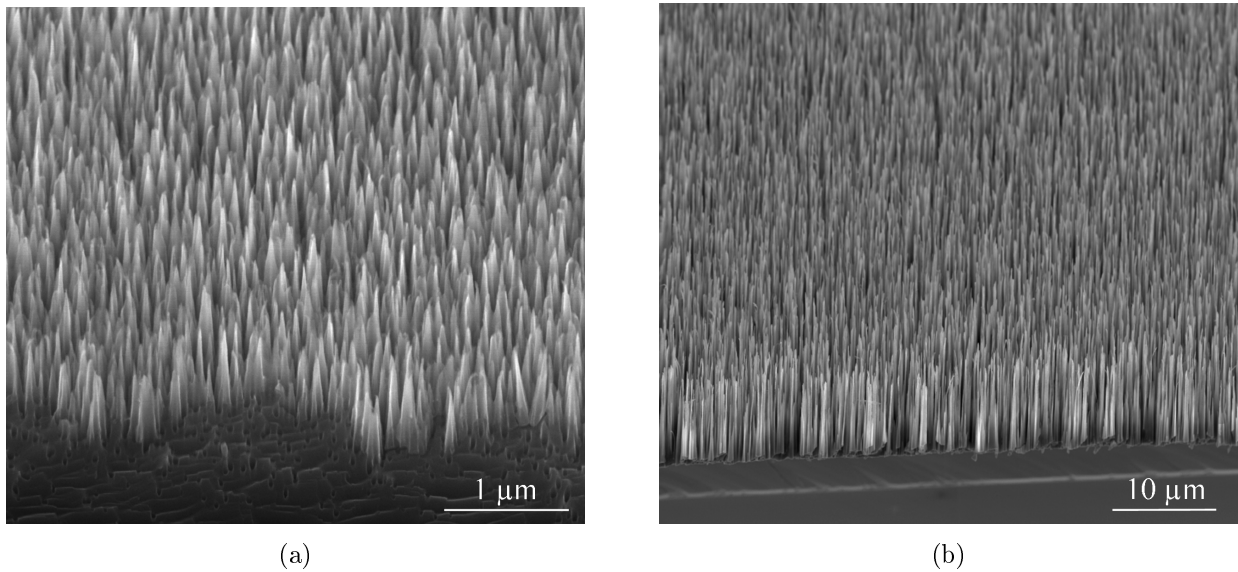


Figure 2.9: a) RIE and b) c-DRIE Silicon Grass.

concentration of the silicon is found. Organic contaminants or the incomplete removal of the natural oxide can also lead to a nanomask, if no pre-cleaning and treatment with hydrofluoric acid is performed.

Silicon Grass is especially observed in strongly anisotropic etching processes where a passivating chemistry is used. For these processes, the incomplete removal of the passivating layer is the primary reason for the nanomask. It is this mechanism which can be utilized to generate Silicon Grass in a controlled manner.

The numerous studies show that the effect of nanomasking cannot be attributed to a single phenomenon or mechanism. In fact, it is the configuration of the process and the system, which brings forward one of the explanatory models. Nearly all theories share the origination of a nanomask, consisting of a distribution of clusters with a material of high selectivity relative to Si . By this, a nucleation site for the following structure formation is being generated.

Because Silicon Grass formation disturbs the homogeneous etching in fabricating defined structures, most publications focus on different strategies for its prevention [RL95] [BS03]. In [LW80] a reproducible generation of Silicon Grass in chlorine-based plasmas is described. Here, the precipitation by local polymer group formation is surmised to be responsible for the nanomasking. Because of the good reproducibility and regularity, the authors already speculate about a possible utilization of the structures ('Random Microfabrication').

In 1995 JANSEN *et al.* published the 'Black Silicon Method' [JDLE95], a technique to optimize plasma etching processes. Here, the occurrence of Black Silicon is used as an indicator to find the proper oper-

ating point of an RIE etching process. Hence, the structures are not actively used but their formation is avoided to guarantee smooth trench bottoms.

Applications which make active use of the structures have emerged since the late 1990's. In this regard, several publications deal with the controlled initiation and control of the surface modification. The methods range between various organized [LHE⁺07] [CNRW06] and self-organized techniques, described in the following. In [KM00] two additional process steps are used: doping of the silicon substrate with high energy nitrogen ions to cause crystal defects and a subsequent oxidation to generate oxygen clusters, because the oxygen is precipitating at the interstitial nitrogen atoms. Others use the liquid flame spray production of silica nanoparticle agglomerates [SKA⁺07] or deposited metals such as *Au* [THKK97] and *Ni* [FMM⁺09] to introduce nucleation sites on which formed reaction products condense preferentially and form etch masks. In [DMT⁺05], [GS06] and [aTM08] a variation of process parameters is used to influence the Silicon Grass formation and its properties. Another method uses femto- and nanosecond-pulsed laser-assisted plasma etching to generate Black Silicon [HFW⁺98] [SCC⁺03] [CCW⁺04]. Here, a different formation mechanism in contrast to the already described methods is assumed because the involved energy densities are orders of magnitude higher and a liquidation of *Si* is supposed.

2.2.2 Applications

Numerous applications use micro- or nanostructured functional surfaces consisting of an array of needle-, pillar- or pyramid-shaped structures. Because the focus of this work is on c-DRIE Silicon Grass, the following overview covers applications which utilize this surface modification generated in plasma processes. Table 2.2 shows the typical geometrical properties of Silicon Grass from RIE and c-DRIE processes.

Table 2.2: Typical geometrical properties of Silicon Grass from RIE and c-DRIE.

Property	RIE	c-DRIE
Height (μm)	0 – 2	0 – 25
Diameter on top (nm)	< 5	> 5
Diameter on bottom (nm)	100 – 400	700 – 2000
Density (μm^{-2})	10 – 20	1 – 2
Surface	<i>smooth</i>	<i>ribbed</i>

Optical and Opto-electronic Applications

The exceptional low reflectivity of the surface modification makes it a promising anti-reflective coating or absorber for Micro-Opto-Electronic-Systems (MOEMS) and other types of opto-electronic devices.

In particular, the application for silicon solar cells has been studied extensively: at first for mono-crystalline cells [BTH⁺98] [SLS00] and later for poly- and multi-crystalline cells [RZN⁺05] [YKT⁺08] as well as for *Si* thin-film technology [KBS06]. A significant enhancement of efficiency was achieved. The downside of the technology is the high cost of reactive plasma fabrication techniques compared to established, wet-chemical etching processes. Since high quantities and large surface areas have to be processed, different methods for parallel processing like barrel etching [aTM08] or special, customized systems for parallel planar plasma etching were developed and evaluated [RKB⁺05]. Furthermore, Silicon Grass is used to optimize *Si* photodiodes [MWM⁺06] or sunlight sensors [LBMM05], where the nanostructure can easily be implemented in the CMOS fabrication process.

Microfluidic and Biological Applications

The high surface area enlargement and good control of surface energies by additional modification (e.g. FC-coating) make the nanostructure a promising functional element for microfluidics, micro-reactors or bio-sensors. It is possible to selectively generate super-hydrophobic or super-hydrophilic areas within microfluidic channels. In [SFK⁺06], [SKA⁺07] and [RDM⁺08] Silicon Grass is utilized as a catalytic structure for microfluidic systems. In combination with *Si* nanowires, Silicon Grass can be used to enhance the interface between *Si* and biological cells [CSW⁺07]. Figure 2.10 a) shows the accretion of chinese hamster ovary cells (CHO-cells) on the treated surfaces. The possible media transport between the nanostructures and the 3-dimensional nature of the interface allow for new concepts of bio-sensors or bio-electronics [KNK⁺07].

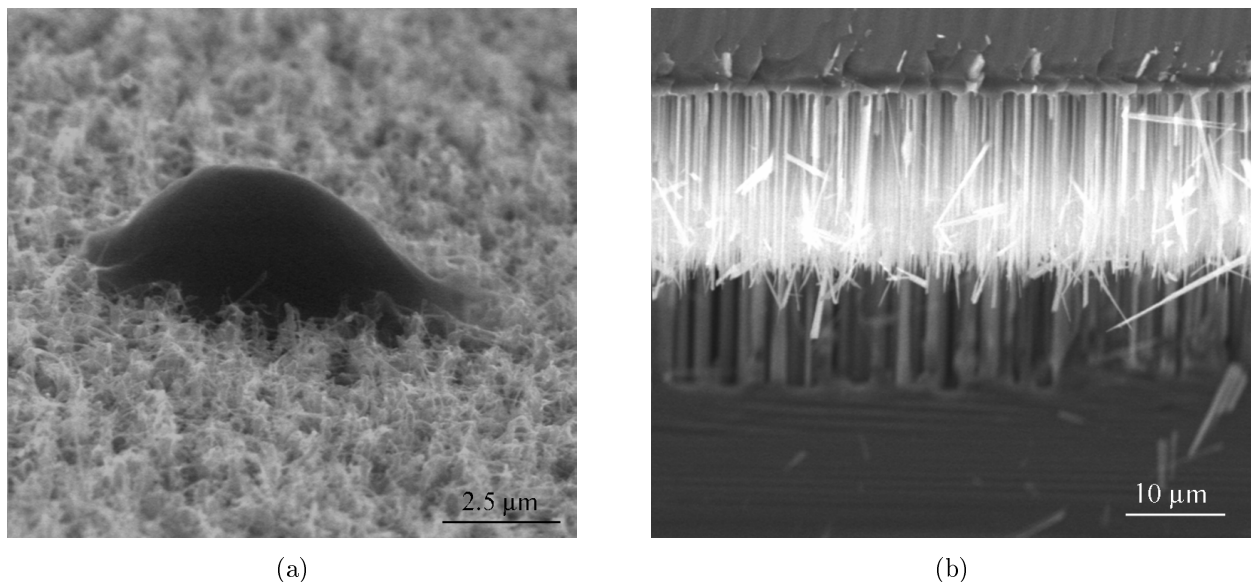


Figure 2.10: Applications of Silicon Grass. a) CHO-cells on Silicon Grass [CSW⁺07] and b) Silicon Grass as Nano-Velcro[®].

Another potential application is the development of new handling techniques for droplet-based biological analysis systems, which utilize electro-wetting or electro-capillary methods in combination with the nanostructured surfaces [FZ07]. Finally, the increasing importance of 3-D integration techniques (e.g. chip-stacking) pose a challenge to the cooling of such highly integrated devices. Here, the implementation of Silicon Grass inside of microfluidic channels can enhance the heat transfer between chip and cooling agent [DLM⁺07].

Application in Packaging Techniques

In recent years, the field of applications has expanded and incorporated packaging techniques. In [SFK⁺06] a new type of bonding technology is presented that is based on the mechanical adhesion of a form-fitted bond of Silicon Grass and can be applied on wafer level at room temperature, see Figure 2.10 b). At low contact pressures, the method is reversible, allowing for a repeated assembly of treated parts. With this method, several devices can be reversibly fixed on a treated substrate by means of a Nano-Velcro[®]. Retention forces up to 20 MPa are achieved, comparable to low level adhesives. A significant influence of the Silicon Grass geometry is expected, which is covered in Section 4.3. Hence, the improvement with geometrical optimization is possible.

The method also enables the bonding of *Si* with other materials such as polymers [SFK⁺07] and ceramics [FdP⁺08]. These material combinations allow new concepts for the design and development of MEMS and offer great potential in the field of micro- and nano-integration techniques. It is, for instance, possible to fabricate new hybrid substrates consisting of several layers of different materials. In this way, different material properties can be utilized effectively within one system, avoiding the problems of packaging and integration in subsequent process steps of standard hybrid fabrication techniques.

The bonding further allows the efficient coupling of polymer tubing to micro-reaction systems based on *Si* without the necessity of additional adapters. By this method, the occurrence of dead volumes, which often represent a disadvantage of standard fluidic coupling techniques, can be minimized [SFV⁺09]. Finally, an alternative to conventional flip-chip techniques is presented in [SZM⁺06]. Here, Silicon Grass is used to establish a solder-free electrical, mechanical and thermal contact between an opto-electronic device and a carrier substrate.

3 Nanomasking - Initiation of Silicon Grass Formation

Self-organized Silicon Grass formation in plasma processes is caused by nanomasking (see Section 2.2) and plays an important role in *Si* etching. Therefore, it is subjected to an in-depth analysis within this work.

This chapter starts with a theory for the origin and the formation process of nanomasking in c-DRIE processes (Section 3.1). Different surface analysis methods such as Scanning Electron Microscopy (SEM), Atomic Force Microscopy (AFM), X-Ray Photoelectron Spectroscopy (XPS) and Auger Electron Spectroscopy (AES) are performed to investigate the morphology and chemical properties of the nanomask (Section 3.2). The nanomasking process is also studied by Optical Emission Spectroscopy (OES) and pyrometry. In a series of experiments, the influence of various process parameters on the morphology of the nanomask is investigated to draw conclusions for the formation (Section 3.3). Furthermore, a method to generate the Silicon Grass in c-DRIE at various parametrical settings is proposed. Finally, a set of studies that are conducted to clarify other relevant influences on the nanomasking process are discussed (Section 3.4).

3.1 Formation Theory

Different nanomasking techniques have been investigated in literature ranging from lithographic methods like e-beam [LHE⁺07] or nanosphere lithography [CNRW06] to self-organized methods like oxygen precipitation [KM00], flame spraying [SKA⁺07], metal deposition [FMM⁺09] [THKK97], sputtering of the reactor walls [MC08] and more. Hence, depending on process chemistry, parameter settings and equipment, the nanomasking in c-DRIE can be produced by several different phenomena, as follows:

- Cluster of a deposited passivation film
- Adsorbates of sputtered materials from mask, electrode or chamber
- Crystallographic defects within the substrate material
- Adsorbates of oxidized etch products

- Contaminants or incompletely removed nature oxide

In order to derive a formation theory for the c-DRIE process, the morphological and chemical analysis in Section 3.2, the results of the described process analysis in Section 3.3 and the various findings of different single tests covered in Section 3.4 are combined. The key findings are listed in the following itemization:

- After one process cycle at the etching-passivation equilibrium, a distribution of clusters is found on the substrate. (Section 3.2.1)
- During the second cycle the clusters develop into filament-like structures. (Section 3.2.1)
- The filament-like structures act as nanomask; its amorphous morphology is transferred into the Si via etching. (Section 3.2.1)
- The surface morphology develops from a fine grainy to a larger clumpy structure within the cycles. (Section 3.2.1)
- The FC-ratio R_{FC} of the clusters is measured to be 0.38 dependent upon a high number of $C-C$ bonds, whereas the $C-F_x$ bonds are all close to the detection limit. (Section 3.2.2)
- No Al is found inside the nanomask, ruling out sputtered chamber material as the source for nanomasking. (Section 3.2.2)
- The adsorbed S from the etching step does not account for nanomasking. (Section 3.2.2)
- Nanomasking is introduced when etching and passivation yield are approximately in equilibrium. (Section 3.3.4)
- Nanomasking on unmasked substrates can be controlled by in situ OES, monitoring the emission line of $F(703.8\text{ nm})$ to set up the appropriate time constants. (Section 3.3.4)
- Shifting the working point within the nanomasking process window results in different morphologies of the nanomask. (Section 3.3.5)
- The nanomask morphology is more affected by a change of deposition step time τ_{dep} and passivation coil power P_c than by a change of bias power during etching P_b . Densities up to $32\ \mu\text{m}^{-2}$ are reached. (Section 3.3.5)
- Carbon dust formation and/or film flaking act as an additional nanomask, observed at high values ($>12\text{ W}$) for bias power during etching P_b . (Section 3.4.1)
- Natural oxide has a significant influence on the onset of nanomask formation, since it leads to a quick surface roughness development. It is not necessary for nanomasking. (Section 3.4.2)

- Adding oxygen as a precursor gas shifts the plasma chemistry towards stronger etching and thus affects nanomasking. (Section 3.4.2)
- Removing organic substrate contaminations by wet chemical treatment has no effect on nanomask formation. (Section 3.4.3)
- Masking affects nanomasking by its influence on geometrical and chemical properties of the substrate surface. (Section 3.4.4)

From these key findings it is concluded, that nanomasking in the Silicon Grass process is initiated by the incomplete removal of the deposited inhibiting film. The remaining material consists of carbon-rich clusters, whereas the absence of F in the nanomask is due to the low F content of the first several monolayers of the deposited FC-film and ion-induced defluorination during the following etching. A low FC-ratio indicates a high etch resistance beneficial to nanomasking. The initial morphology of the nanomask is defined by the morphology and laterally varying chemical composition of the deposited FC-film in the first two cycles. It can be influenced by process control to generate different types of nanomasks. Nanomasking depends on every process parameter affecting the etching-passivation equilibrium. Because the abrasion of the inhibitor depends strongly on the angle of the incident ions, the overall removal of inhibitor becomes less effective as areas with off-normal orientation are introduced. It follows that, once a certain surface roughness is reached, nanomasking perpetuates itself.

Figure 3.1 graphically depicts the Silicon Grass formation theory derived from the findings of this work. In the first cycle a distribution of carbon clusters remains on the surface. They are expected to originate from carbon-rich macro molecules being generated in highly polymerizing plasmas such as C_4F_8 [SST98], [TT01a], [TT01b], [TT02]. Due to an increased polymerization rate at the remaining carbon clusters, filament-like structures develop at these sites during the second cycle. This has also been observed to take place on top of Silicon Grass needle tips in [AS08].

No Si is etched but SiO_xF_y , SOF_x , CF_x and COF_x are formed as etch products from the natural oxide and FC-film. It is assumed that SiO_xF_y readsorbs on the clusters increasing their etch resistance. In the c-DRIE process utilized, Si etching sets in at the end of the third cycle, drastically affecting the surface roughness. Etch products now consist mainly of SiF_x and CF_x . After that, the created roughness affects deposition and subsequent inhibitor removal. Crests and vertices receive a greater flux of C_xF_y precursor molecules, creating a slightly thicker top while the abrasion at the flanks of the features is reduced during etching. Depending on the etching passivation equilibrium, the individual features get larger (stronger passivation), eventually overgrowing one another, or they get thinner (stronger etching), where smaller features are etched away at some point. In any case, the structure density decreases in the process.

A reduced structure density with an increasing number of process cycles is observed for every parametrical setting. In Chapter 4 this effect is discussed, where Silicon Grass density progression is analyzed

throughout the 75 cycles of the Silicon Grass process. It is found that in addition to density, other geometrical properties (e.g. sidewall morphology) of the resulting Silicon Grass can also be influenced by process parameters, which makes the c-DRIE a proper process for the generation of adapted *Si* surface nanostructures.

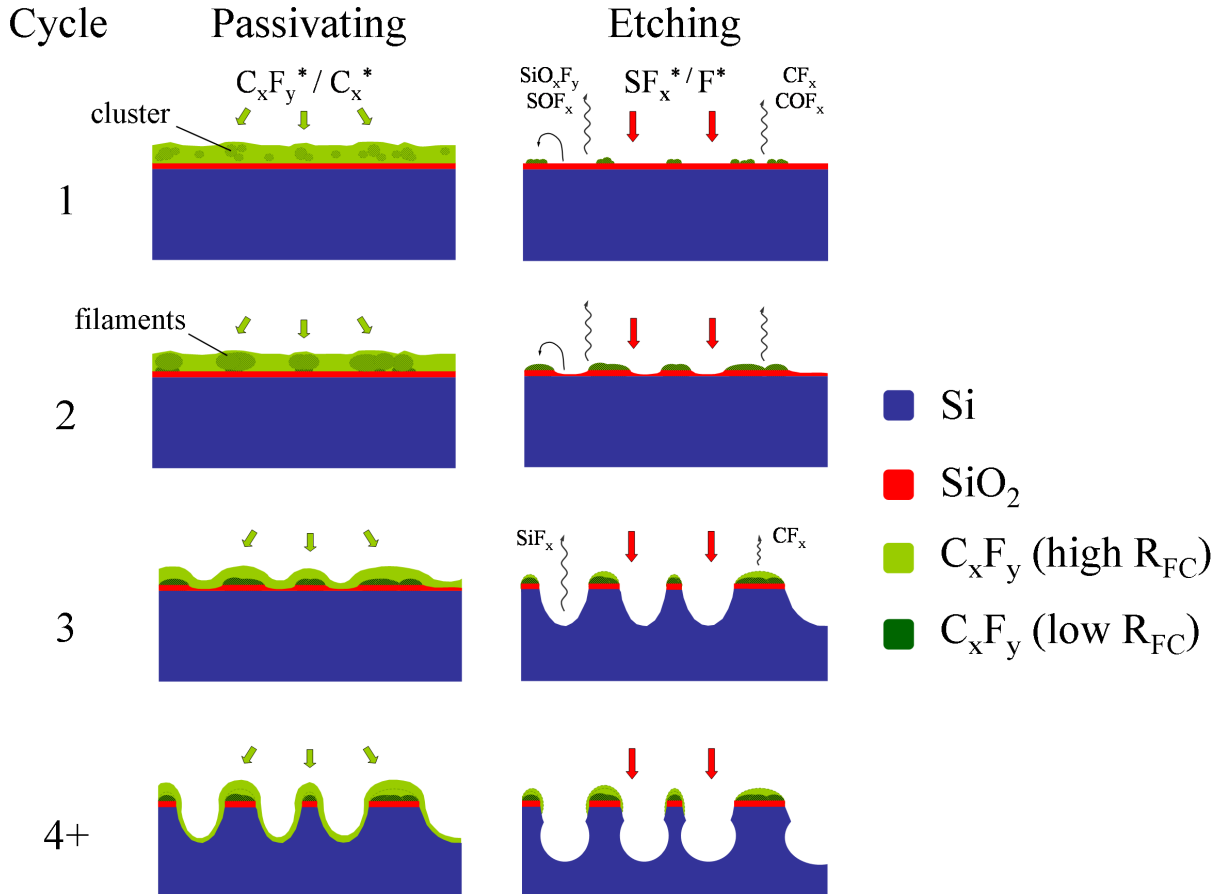


Figure 3.1: Sketch of Silicon Grass formation in c-DRIE processes.

3.2 Surface Analysis

In the following section the morphological and chemical analysis of the nanomask by SEM, AFM, XPS and AES is covered. The tools utilized are listed below:

- Scanning Electron Microscope (SEM), Type *S 4700*, Hitachi High-Technologies Corp.
- Atomic Force Microscope (AFM), Type *Atos*, NT-MDT Corp.
- X-Ray Photoelectron Spectrometer (XPS), special design (description in Section 3.2.2)
- Auger Electron Spectrometer (AES), Type *VG 350*, Thermo Fisher Scientific Inc.

Probes are prepared by processing silicon substrates ((100), diameter 100 mm, thickness 525 μm , resistivity 7 – 10 $\Omega\text{ cm}$, doping n-type phosphorus) in the ICP-multiplex from Surface Technology Systems shown in Figure 2.6. The parameters of a Silicon Grass generating process are given in Table 3.1.

Table 3.1: Silicon Grass generation process parameters.

Parameter	Passivation	Etching
$Q_{C_4F_8}$ (sccm)	85	-
Q_{SF_6} (sccm)	-	130
Q_{O_2} (sccm)	-	13
Step time (τ) (s)	11	9
P_c (W)	450	450
P_b (W)	-	12
p (Pa)	2.5	4.3
T_C ($^{\circ}\text{C}$)		40
T_S ($^{\circ}\text{C}$)		20
Process time (min)		25

3.2.1 Morphology Analysis

SEM Measurement

To investigate the morphology of the nanomask, the standard Silicon Grass process is stopped after one, two and five cycles. The obtained substrate surfaces are analyzed by SEM, see Figures 3.2, 3.3 and 3.4.

After the first cycle a distribution of clusters is found on the surface, see Figure 3.2. The morphology then changes into filament-like structures at the end of the second cycle, see Figure 3.3. They appear as

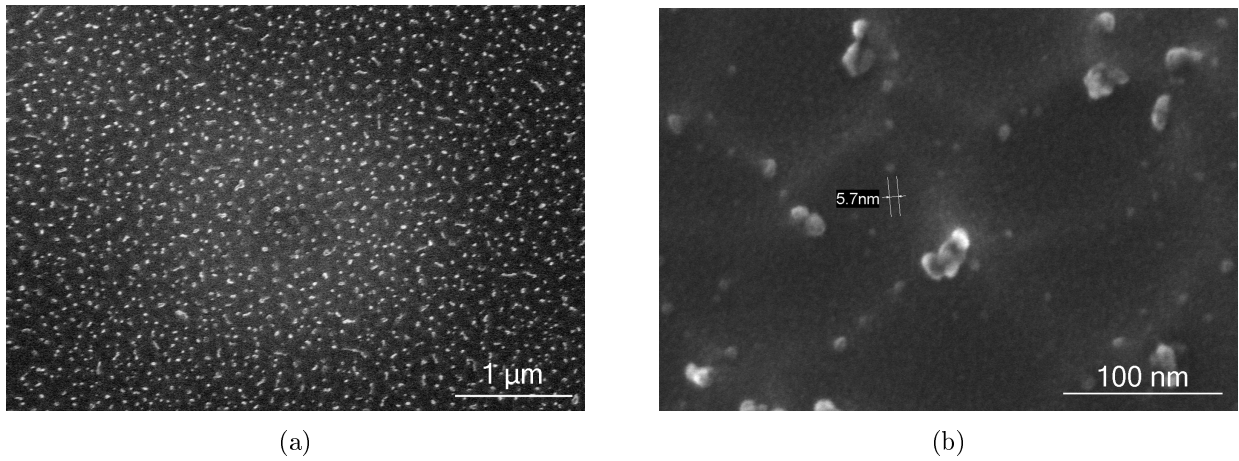


Figure 3.2: SEM of the nanomask after one cycle; magnification a) x25k and b) x150k.

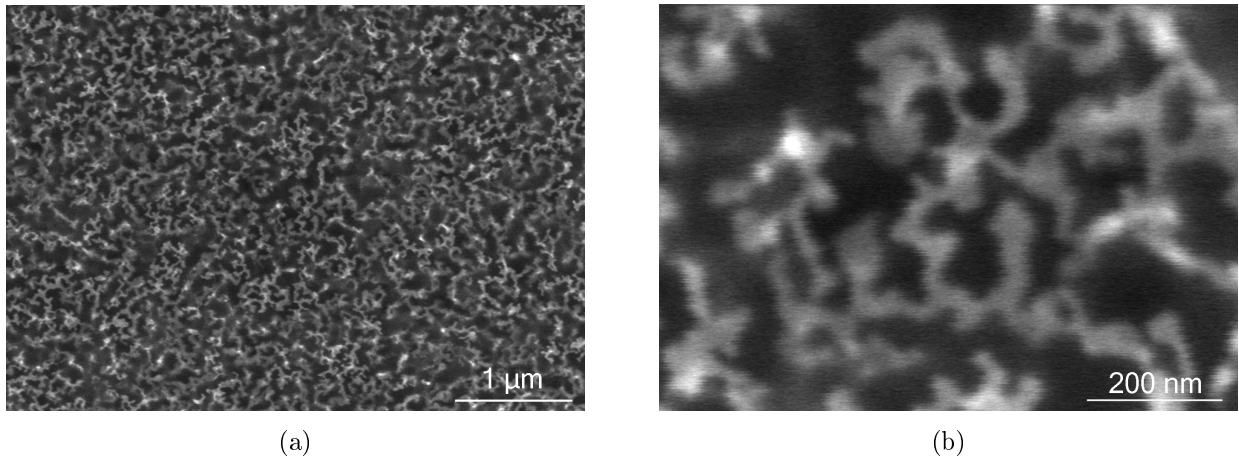


Figure 3.3: SEM of the nanomask after two cycles; magnification a) x25k and b) x150k.

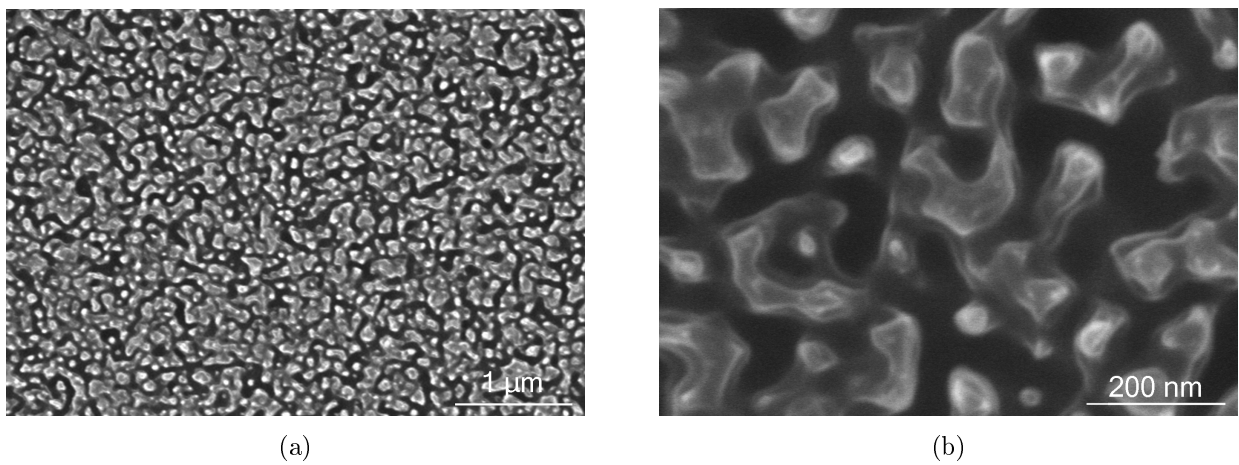


Figure 3.4: SEM of the nanomask after five cycles; magnification a) x25k and b) x150k.

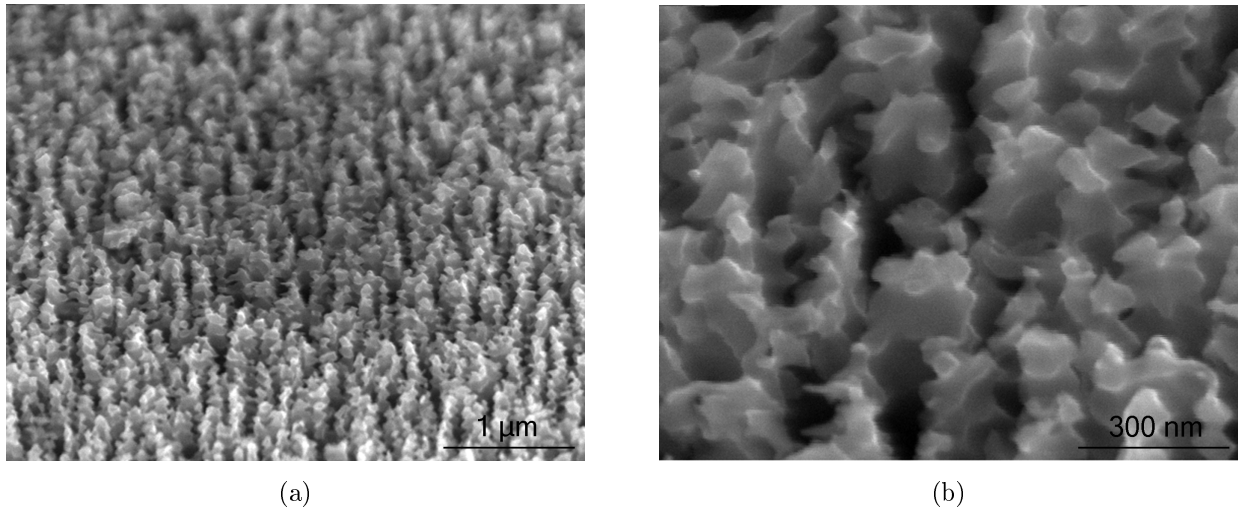


Figure 3.5: SEM of the nanomask after five cycles with coarser structures (45° view); magnification a) x25k and b) x100k.

branching and curled formations, resembling amorphous polymer chains left over after etching. After five cycles the morphology and arrangement of the amorphous structures is reproduced into the silicon surface, although the structures get coarser and cascaded from the cyclic etching, see Figure 3.5.

Depending on the process parameters, the density can vary, which is discussed in greater detail in Section 3.3.5. It is found that with stronger etching the nanomask is coarser, whereas the individual structures are higher. This is explained by the disappearance of smaller structures and the appearance of deeper trenches with stronger etching.

AFM Measurement

To further characterize the morphology, AFM measurements are taken after two, five and 15 cycles, see Figure 3.6. The measurement is done in semi-contact mode at a scan speed of $2\mu\text{m}/\text{s}$ for a scanned area of $2 \times 2\mu\text{m}^2$.

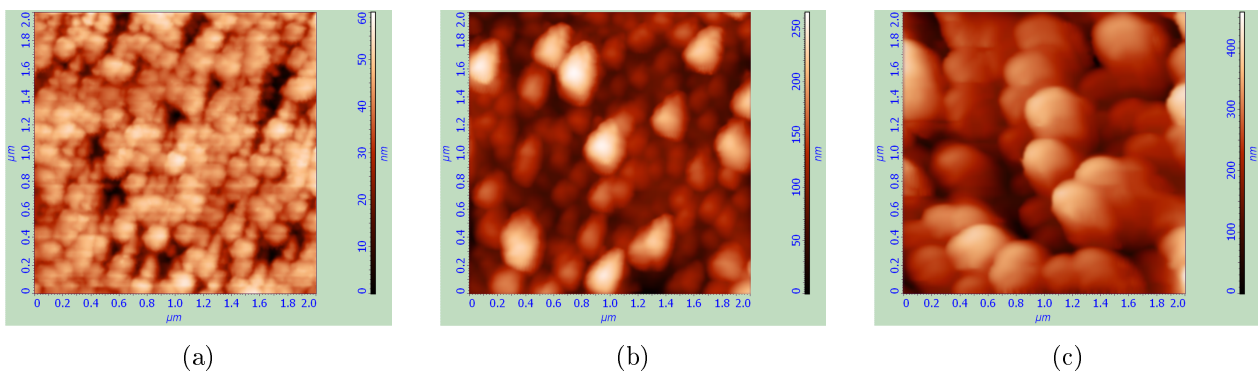


Figure 3.6: AFM of the nanomask after a) two, b) five and c) 15 cycles. Scanned area: $2 \times 2\mu\text{m}^2$.

The following Table 3.2 gives an overview of the parameters maximum height of profile $R_{t,NM}$ and average roughness $R_{a,NM}$ of the scanned area. It is clearly seen that the surface morphology develops from a fine grainy to a larger clumpy structure within the cycles. $R_{a,NM}$ scales from about 6.5 nm after two cycles to about 53.9 nm after 15 cycles. After five cycles some clusters seem to dominate in the process, finally overgrowing neighboring ones.

The findings are compared to the AFM study of a thin ($\approx 50\text{ nm}$) deposited FC-film before etching, see Figure 3.18.

Table 3.2: AFM results characterizing the nanomask.

Parameter	2 cycles	5 cycles	15 cycles
$R_{t,NM}$ (nm)	60.0	251.0	436.1
$R_{a,NM}$ (nm)	6.5	32.4	53.9

Radial Inhomogeneity

An investigation of the surface after the five cycle nanomasking process reveals a radial inhomogeneity of morphology across the wafer. As one progresses from the rim towards the center, it changes from rougher, coarser features towards smoother ones, which cover a greater part of the surface. Figure 3.7 shows the surface after a five cycle nanomasking process at three different radial wafer positions.

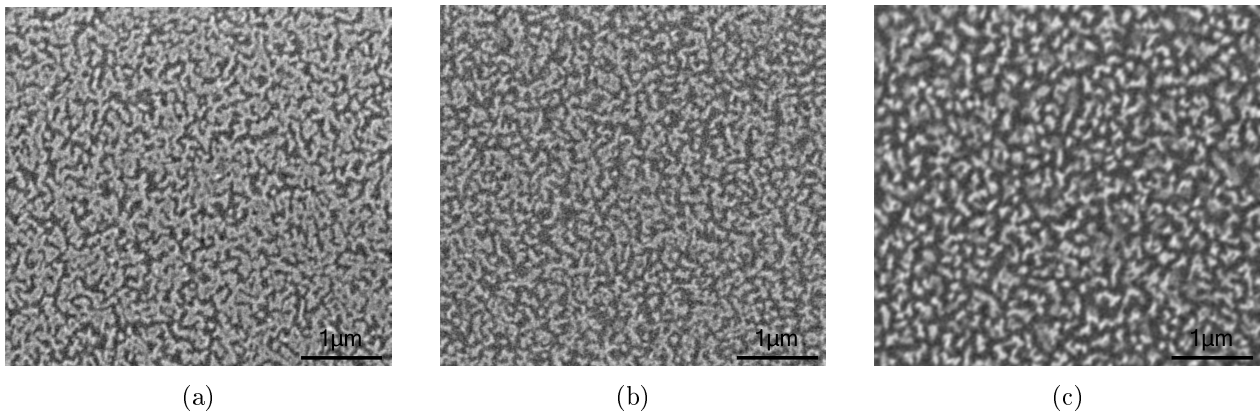


Figure 3.7: Radial inhomogeneity of the nanomask: a) *Center*, b) $R=20\text{mm}$ and c) $R=40\text{mm}$.

Since nanomasking is a delicate process which is easily affected by slight changes in the etching-passivation equilibrium, this inhomogeneity is attributed to a non-uniform etching of the c-DRIE process. The inhomogeneity perseveres from the nanomask to the resulting Silicon Grass, whereas the effect is significantly reduced for a small silicon load of masked substrates. This further supports the influence of radially inhomogeneous etching.

Radial inhomogeneity can become a considerable disadvantage of plasma-etched, self-organized nanostructures since it limits the reproducibility of the structure geometry, narrows the possible process window for a successful generation and hinders the prospect of influencing the generated structure geometry in a controlled manner. Therefore, plasma etching systems with good uniformity are preferred for controlled Silicon Grass generation. Because the uniformity of the ICP-system utilized is relatively poor (see Figure 2.7) compared to ICP systems of most recent development, the problem of uniformity should pose no significant problem.

3.2.2 Chemical Analysis

XPS Measurement

In order to clarify the elemental composition and the predominant chemical bonds of the nanomask, different XPS measurements are performed and compared to measurements of solid, deposited FC-films. The process parameters are given in Table 3.3. Parameters which are not listed are the same as given in Table 3.1.

Table 3.3: Comparison of process parameters of the nanomask and a solid FC-film.

Parameter	nanomask		FC-film
	passivation	etching	passivation
$Q_{C_4F_8}$ (sccm)	85	—	85
Q_{SF_6} (sccm)	—	143	—
Q_{O_2} (sccm)	—	—	—
τ (s)	9	5.3	9
P_c (W)		450	
P_b (W)	—	18	—
p (Pa)	2.5	4.3	2.5

The XPS module used is a customized UHV tool operating at a base pressure below 2×10^{-8} Pa using a monochromatic $Al(K\alpha)$ radiation source (Type PHI 10-60E, Omicron) operating at 300 W and an acceleration voltage of 14 kV (Monochromator XM1000). The emitted electrons are analyzed at a take-off angle of 53° (with respect to the surface normal) by a hemispherical electron energy analyzer (Type EA 125, Omicron) at a constant pass energy of 50 eV (survey spectra) and 15 eV (core level spectra). For a pass energy of 15 eV the chosen operation conditions lead to a total energy resolution of 0.6 eV, which is determined by measurements on $Ag3d_{5/2}$ at a polycrystalline silver sample. For data analysis the measured curves are fitted by a Gaussian-Lorentzian function while a Shirley-type background is subtracted.

Figure 3.8 shows the XPS survey spectra of the nanomask. A detailed analysis is done by high resolution scans of the $F1s$, $C1s$ and $O1s$ peaks (core level spectra). For the nanomask the $S2s$ and $Si2p$ peak are also inspected. Due to a slight surface charging of the insulating FC-layer, the spectra are shifted. The nanomask spectrum is shifted (shift $< 0.3\text{eV}$) and aligned at the $Si2p$ peak ($Si2p_{3/2}$ component) at 99.4eV (literature value for $(100)Si$ taken from [MSSB95]), while the solid FC-film is shifted about 2eV and aligned at the $F1s$ peak at 689.0eV according to previous works on fluorocarbon films [HYO⁺08] [MSSB95]. The shifts are subsequently applied to the high resolution scans. Within experimental time, no considerable peak shape change due to degradation by x-ray irradiation is observed.

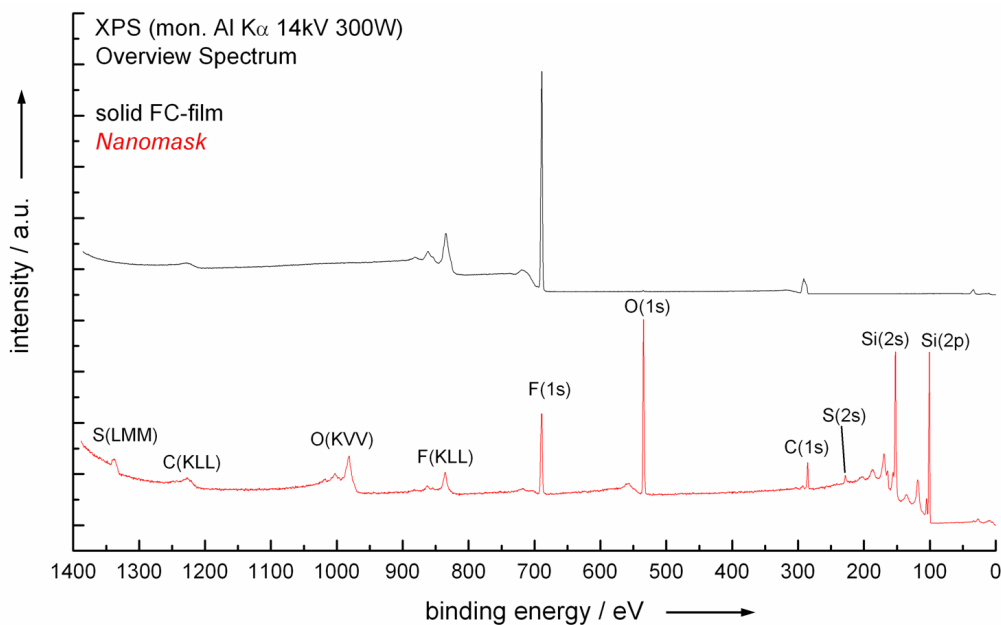


Figure 3.8: XPS measurement overview of the nanomask and a solid FC-film.

The chemical structure is defined by the elemental composition and the existing chemical bonds inside the layers. Figure 3.9 compares the $F1s$ spectra of the nanomask and the solid FC-film. Whereas for the solid FC-film a single peak for $F-C$ is found (which is used for the spectrum alignment at 688.9eV described above), the spectra of the nanomask reveals a double peak structure. The peaks are ascribed to $F-C$ (688.9eV) and $F-S$ (687.8eV) bonds, since adsorbed SF_x is expected after etching with SF_6 [TCCG99].

A strong distinction between the two samples can also be found in the $C1s$ spectra shown in Figure 3.10. Whereas the solid FC-film is composed of $C-F_3$ (293.5eV), $C-F_2$ (291.4eV), $C-F$ (289.1eV) and $C-(CF_x)_y$ (286.7eV) bonds (all bond energies taken from [PKL⁺94]). It also contains some $C-F_x$ bonds as the small peaks near the detection limit at the corresponding positions indicate. No recognizable peaks can be found for $C-Si$ (283.4eV) or

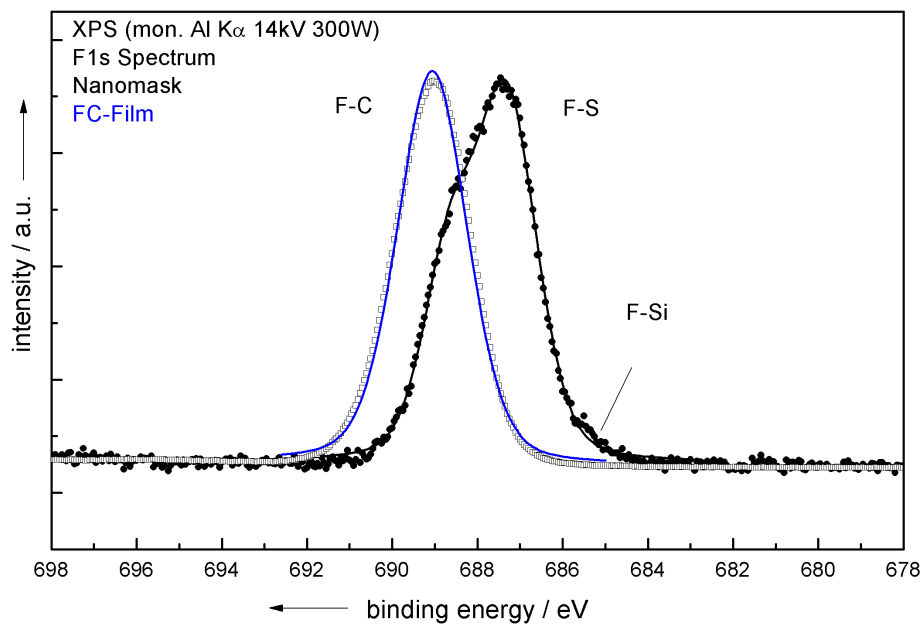


Figure 3.9: F1s peak comparison of the nanomask and a solid FC-film.

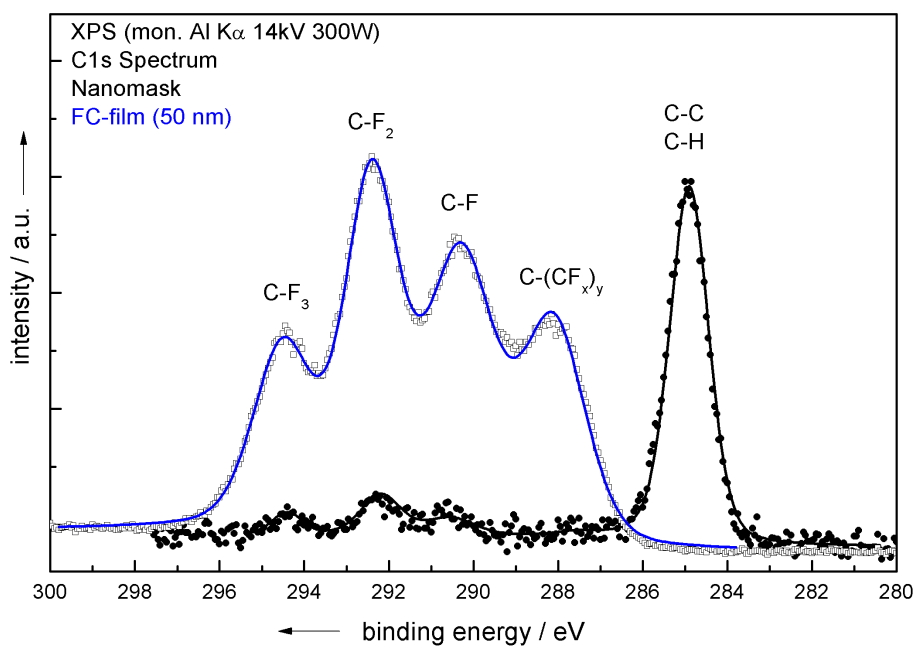


Figure 3.10: C1s peak comparison of the nanomask and a solid FC-film.

$C-(CF_x)_y$. It is also noted that no peak for Al is observed, thus ruling out AlF_3 as responsible for nanomasking as reported in [OSJ86].

The spectra of the solid FC-film is typical for C_4F_8 plasma passivated films and similar results are known from literature [TT01a] [YKO⁺04] [LDB⁺04]. All types of bonds range in the same order of magnitude in the frequency of their occurrence. Assuming a homogeneous chemical structure, this indicates a highly branched network of the FC-film.

The relative peak areas can be used to estimate the surface composition. For the calculation of the samples a homogeneous film model is used. A detailed description of the procedure is given in [KBE⁺07]. For characterizing perfluorocarbon polymers the fluorine to carbon ratio (FC-ratio, R_{FC}) is a common measure. In the case of the nanomask, R_{FC} is calculated by the fitted peak areas of the $C1s$ spectrum after equation 3.1 from [SHJ⁺04]. Table 3.4 shows the percentage elemental composition of both samples and the FC-ratio of total elemental composition $R_{FC,total}$ and the FC-ratio calculated from the $C1s$ peak R_{FC} .

$$R_{FC} = \frac{\sum_{i=1}^3 iA(C-F_i)}{A(C1s)} \quad (3.1)$$

Table 3.4: Elemental composition of the nanomask and a solid FC-film.

	C	F	O	S	Si	$R_{FC,total}$	R_{FC}
nanomask	9.5	6.5	16.6	2.6	64.8	0.70	0.38
FC-film	46.9	52.5	0.6	—	—	1.12	1.43

Since the nanomask is a composition of clusters on the substrate, a high Si concentration due to exposed Si is found. The high O concentration is explained by a) natural oxide which has not been removed before FC-film deposition and b) adsorbed water or O from ambient air during transportation to the XPS module. S is detected because it is used in the etching and adsorbs on the surface.

The solid film consists solely of F , C and O . The small O peak cannot be explained by a natural oxide layer, since the XPS measurement only has an information depth of about 10 nm maximum. It results instead from adsorbed water and O during transportation.

These findings show a strong distinction between the chemical structures of both samples. It is concluded that the nanomask consists of less fluorinated carbon clusters or chains, whereas the solid film consist of a stronger fluorinated carbon network structure.

Three mechanisms can explain the different chemical structures:

- The chemical structure changes with film thickness due to an inhomogeneous deposition process where initially mostly carbon is adsorbed on the surface which is subsequently fluorinated or covered by CF_x .
- The chemical structure is altered by reactions with SF_6 and/or bond breaking and reorientation by physical sputtering of the bombarding ions in the etching step (e.g. ion-induced defluorination).
- A combination of both mechanisms.

AES Measurement

To investigate the possibilities discussed in the previous section, an AES analysis is performed. Here, the passivation parameters are those given in Table 3.3 previously, except that for the FC-film one short cycle with four seconds of deposition time is applied, in order to deposit an FC-film of comparable thickness to the nanomask. After the generation in the ICP-multiplex system, the probes are quickly transferred ($< 5 \text{ min}$) to the analysis chamber to limit oxidation, water adsorption and contamination. The resulting AES spectra are compared in Figure 3.11. A strong C signal is found whereas F can barely be detected for the FC-film. O and Si are present in both samples, caused by a natural oxide layer on the Si . This shows that the results represent the whole deposited film and not only the surface layer. Compared to the thin FC-film, the nanomask has a strong S signal due to adsorbed sulphuric composites from SF_6 etching as well as a small N peak due to chamber flushing with N after etching.

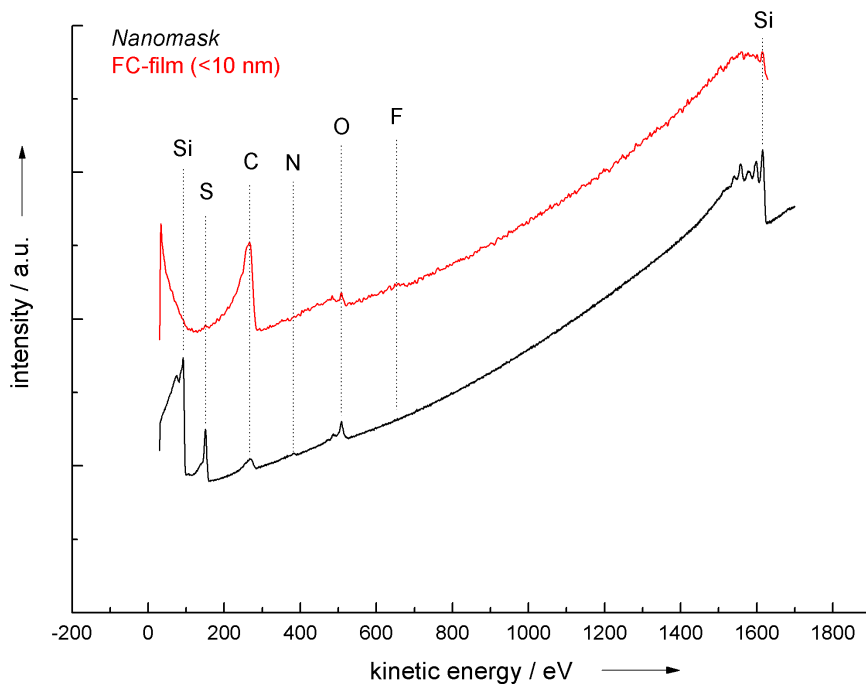


Figure 3.11: AES analysis of the nanomask and a thin solid FC-film.

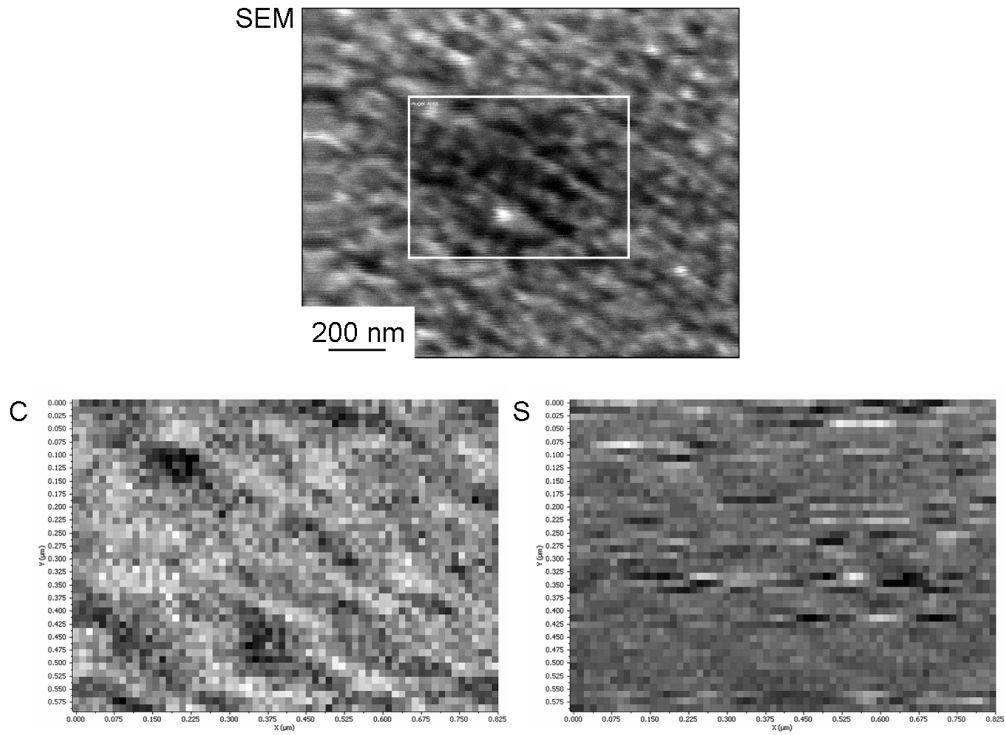


Figure 3.12: Elemental area-scan for C and S of the nanomask.

The bright and dark lines parallel to the x-axis in the S area-scan are measurement errors.

To find out whether S also participates in masking, an additional elemental area-scan for C and S of the nanomask is performed. The result is given in Figure 3.12. It clearly demonstrates that the morphology in the SEM image is reflected in the elemental scan for C but not in the scan for S . Hence, it is concluded that the adsorbed S is homogeneously distributed on the surface and cannot be responsible for nanomasking.

The findings support the explanation of an inhomogeneous deposition where initially mostly C adsorbs. However, the changes of S and C emissions indicate a chemical alteration and previous XPS studies showed that the etching of FC-films by SF_6 plasma changes the chemical structure [Kep08]. It is concluded that a combination of both mechanisms is probable.

3.3 Process Analysis

Nanomasking is an effect occurring at the end of the etching step, when the thin passivation layer is clustered before it is removed completely. In order to understand nanomasking in the c-DRIE, the passivation and the etching step are investigated. The process is analyzed by OES, XPS, SEM, profilometry and pyrometry to study influencing parametrical factors and time-dependent changes. It is found that *in situ* OES provides a useful way to control the nanomasking within the c-DRIE process and guarantees reproducible Silicon Grass generation. Experimental process studies are conducted to find parametrical influences on the nanomasking process and gain insight into the formation principle. In a parametrical study, the effect of passivation time τ_{dep} , coil power (in passivation) P_c and bias power (in etching) P_b on the morphology of the nanomask is investigated. In order to limit the experimental complexity, Design of Experiments (DoE) methods are applied.

3.3.1 Pyrometry

Temperature progression is analyzed by infrared pyrometry at wavelengths of 8 – 14 μm (IN 5plus, IMPAC Electronic GmbH), see Figure 3.13. The device is mounted at a window centrally above the wafer inside the chamber lid. A correction of 0.14 K/min (assumed linear) is applied to compensate for the change in emissivity due to altered surface roughness and different surface material. This is derived by measuring the difference at 20°C reference temperature from before and after the process.

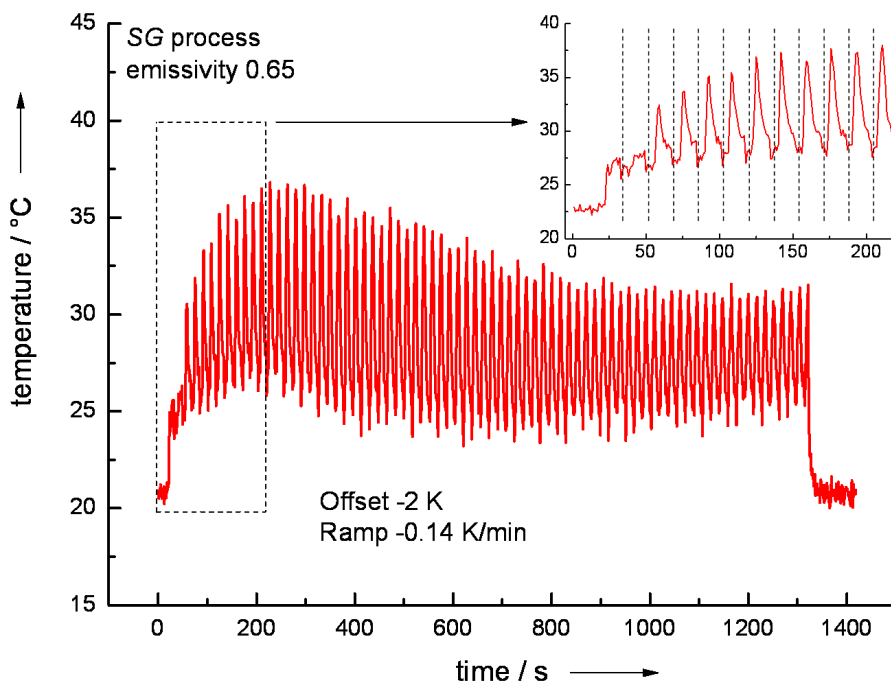


Figure 3.13: Temperature shifts occurring during Silicon Grass generation in c-DRIE etching.

As can be seen in the figure, the temperature rises initially by about $5K$. Then short-term temperature shifts due to the cycling between etching and passivation follow. Due to the fact that etching of Si by fluorine radicals is exothermic and also accompanied by ion bombardment, the rising edge of the curve is assigned to the etching step, whereas the falling edge is assigned to passivation. The temperature amplitude increases quickly from approximately $2K$ to more than $10K$ after 10 cycles. After remaining at a maximum for approximately $400s$, it decreases back to lower values toward the end of the process. The increase can be explained by the development of surface roughness and the associated increase in etched surface material. It indicates that etching slows after $400s$, corresponding to measurements of Silicon Grass structure height development, which is discussed later in Section 4.1.2. The smaller graph in Figure 3.13 depicts a magnified view of the first 12 cycles. The first two peaks are low, indicating that Si is not yet etched and the surface is still covered by a thin FC-film and natural oxide. In the third cycle, Si etching starts and raises the surface temperature significantly. A slight ramp of about $3K$ can also be noticed. The surface temperature at the initiation of the passivation step is several K higher than at the end of the step, which has an effect on the deposition rate [d'A90], further implying an inhomogeneous chemical structure of the FC-film layers.

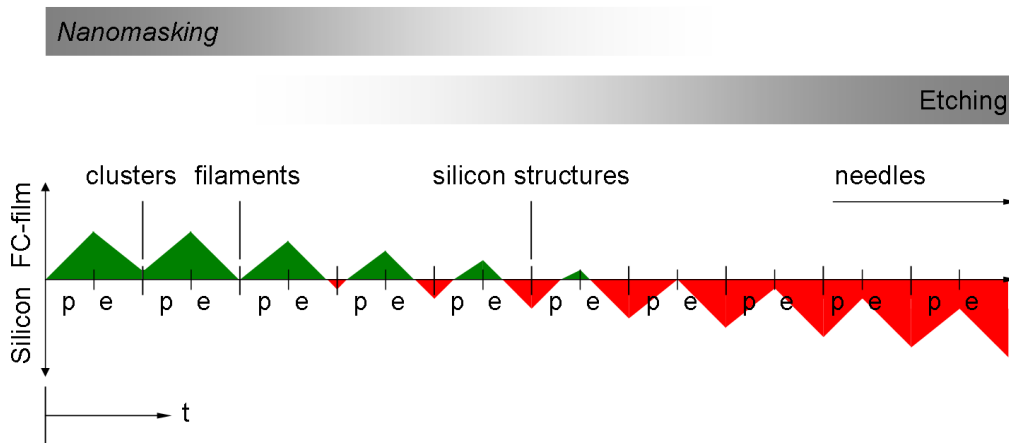


Figure 3.14: Illustration of the early phase of the Silicon Grass generation process.

From the pyrometry measurement, an illustration of the early phase of the Silicon Grass generation process is derived, see Figure 3.14. Nanomasking takes place in the first cycles and blends with the subsequent structure etching. The sketch shows a shift from passivation toward etching as the surface temperature heats up several K in the process.

In carbon-containing plasmas the working point of the process shifts between passivation and etching. It depends on the plasma chemistry, which in turn is strongly affected by changes in gas composition, power settings or pressure. This fact poses the challenge of controlling the working point in constant mode plasmas, where etching and sidewall passivation occur simultaneously and small parametric changes have huge effects. By spatially separating the two process chemistries, the working point can

easily be controlled by setting up appropriate time constants for the process. Because nanomasking is a phenomenon appearing when etching and passivation are close to equilibrium, this timed process control is used to set up the correct working point for a reproducible and effective Silicon Grass generation.

3.3.2 Passivation

Nanomasking is influenced by chemical and physical properties of the deposited FC-film. A lateral inhomogeneity causes differential etching which finally leads to the nanomask. As will be discussed in Section 3.3.5, one of the most important parameters affecting the nanomask is deposition step time, which relates to FC-film thickness. For this reason the chemical and morphological properties of the FC-film as well as relevant parameters affecting the deposition rate are discussed.

Plasma chemistry is divided into reactions occurring in the plasma volume and surface reactions taking place on the substrate. Both types of reactions are affected by different plasma parameters and setup. A list of the most important parameters for passivation is given below:

- Coil power
- Bias power
- Pressure
- C_4F_8 flow rate
- Substrate temperature
- Chamber temperature
- Chamber setup and geometry
- Substrate properties (material, thickness, etc.)

Because coil power and pressure are the main parameters influencing the dissociation and radical density, they greatly affect gas-phase volume reactions inside the plasma. This can clearly be seen in the OES spectra taken by a VIS-IR spectrometer (getSpec-2048, getAMO *c/o* Sentronic GmbH) for different parametrical values, see Figure 3.15. The device is mounted at a slightly eccentric quartz window located inside the chamber lid.

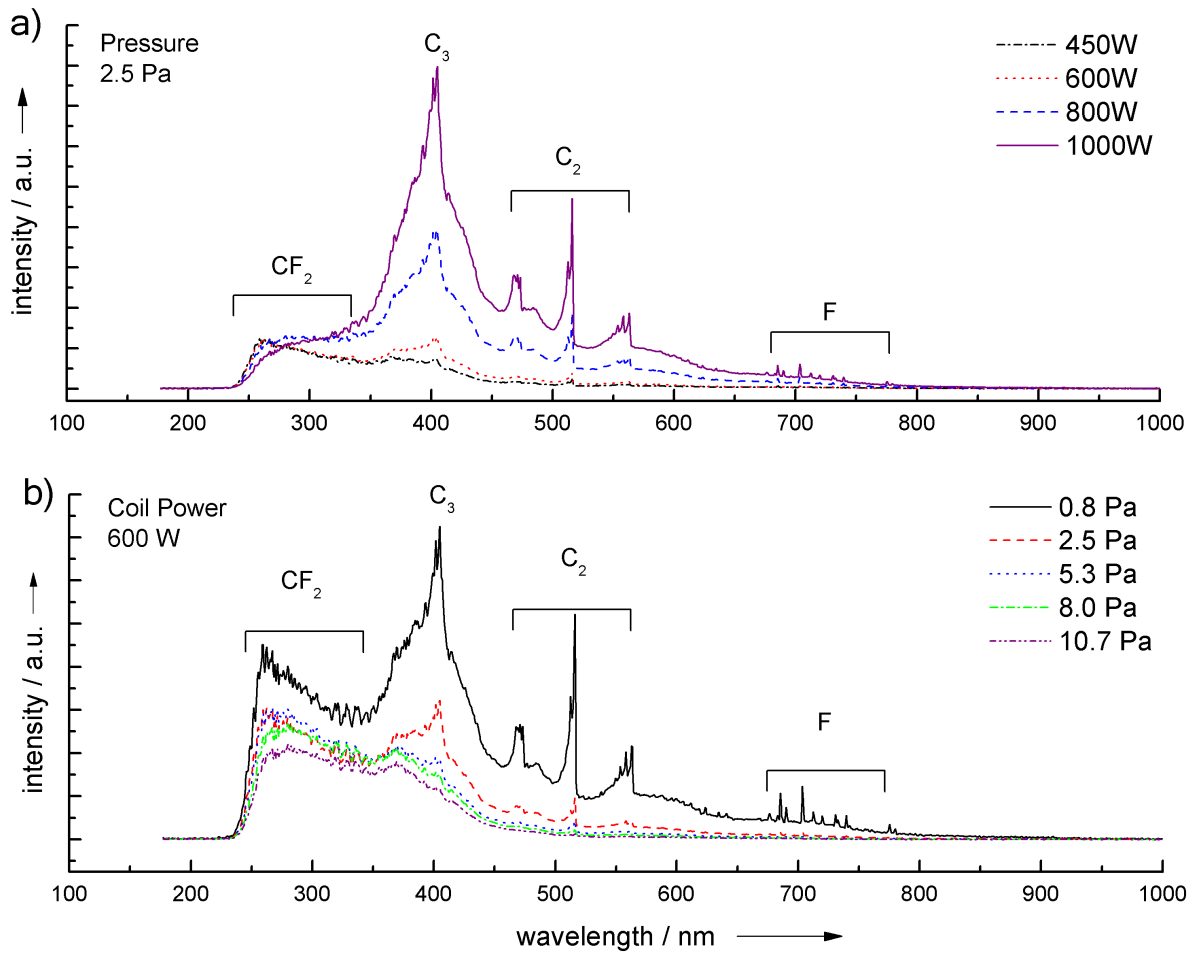


Figure 3.15: OES spectra of C_4F_8 at different a) pressure p and b) coil power P_c settings.

Parameters: $Q_{C_4F_8} = 85 \text{ sccm}$, $P_b = 0 \text{ W}$, $T_S = 20^\circ\text{C}$, $T_C = 45^\circ\text{C}$.

Substrates: $(100)\text{-Si}$, $t_w = 525 \mu\text{m}$, $D_w = 100 \text{ mm}$, n-doped P , $R_w = 1 - 5 \Omega \text{ cm}$.

The graphs show a similar behavior of increased coil power and reduced pressure. In both cases the peaks for C_2 , C_3 and F increase in comparison to the CF_2 peaks, indicating raised dissociation of the feedstock gas, induced either by a higher collision rate through a higher electron temperature T_e (Power) or a smaller amount of C_4F_8 molecules present, which are dissociated (pressure). Additionally, the rate of recombination reactions increases for higher pressures, constraining the level of dissociation of the feedstock gas. The spectra are categorized in two regimes; a C_2/C_3 dominated, high dissociation regime at high power and low pressure and a CF_2 dominated, less dissociated regime at low power and high pressure.

Chemical Composition

From the OES spectra observed surface reactions taking place on the substrate cannot be deduced. Therefore, to analyze the effect of the different plasma conditions on the chemical structure of the deposited FC-film, an XPS measurement of two samples is performed. The OES- and corresponding XPS-C1s spectra are shown in Figure 3.16 and 3.17. The parameters are as in Figure 3.15.

The result shows that the different plasmas lead to a change in the chemical structure of the passivation layer. Both spectra are aligned and equalized to match each others maximum peak intensity for $C-F_2$ for a better comparison. While the peaks for $C-F_3$ are approximately identical, the 600 W sample shows a lower amount of $C-F$ and $C-(CF_x)_y$. The calculated FC-ratios are 1.13 and 1.22 for the 450 W and 600 W sample, respectively. It is concluded that a higher dissociation of precursors leads to a higher FC-ratio in the deposited film. This finding is also reported by Labelle *et al.* in [LDB⁺04], where they explained the effect by assuming a two-step deposition mechanism: initial deposition of a C-rich film and subsequent fluorination by free F. The higher amount of free F in the high power low pressure mode allows for enhanced fluorination as compared to the other regime, where F is scarce and mostly CF_2 and larger fluorine deficient species such as C_4F_6 , C_3F_4 and C_xF_y ($x \approx y > 4$) are the dominant deposition precursor molecules.

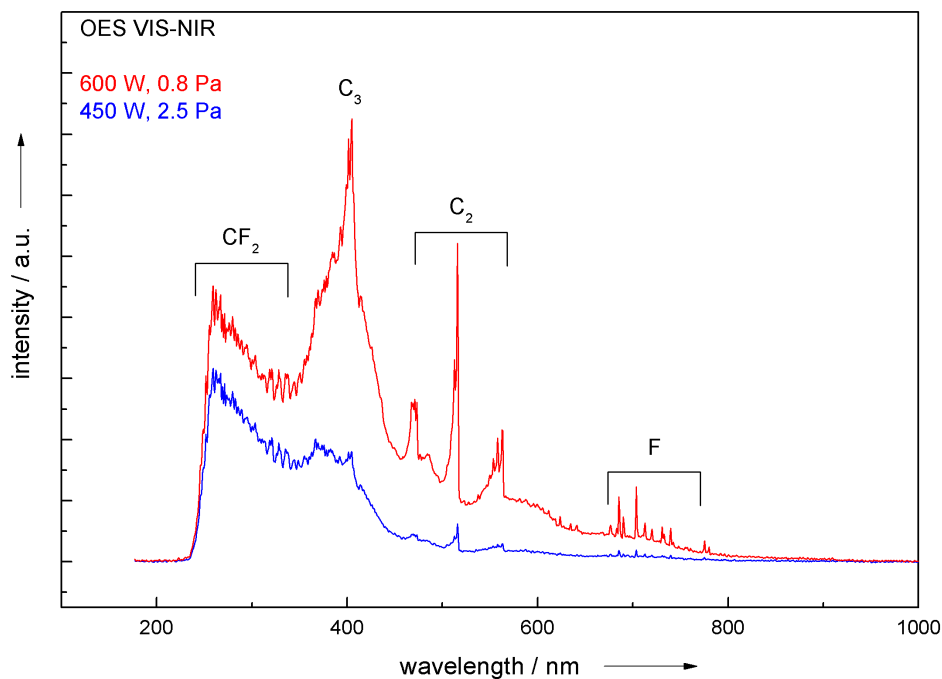


Figure 3.16: OES spectra of C_4F_8 at different passivation settings.

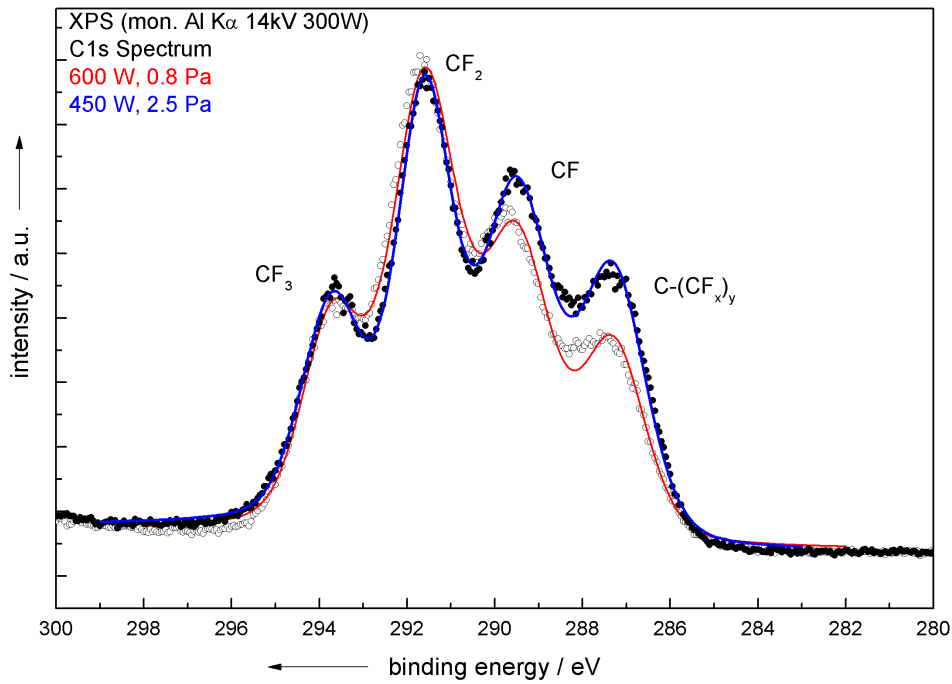


Figure 3.17: XPS C1s spectra of FC-films deposited at different passivation settings.

Morphology

In order to analyze the morphology of a thin (≈ 50 nm) FC-film before etching, a sample is prepared and investigated by AFM. Figure 3.18 shows the height and phase information of a $1 \times 1 \mu\text{m}^2$ surface scan. It reveals an amorphous structure resembling the one discovered by SEM of the nanomask. The calculated roughness gives a $R_{a,FC}$ of 0.139nm and a maximum peak height $R_{t,FC}$ of 1.69nm . Assuming a selectivity $S_{Si,FC}$ of Si to FC-film etching of 50–100 and a homogeneous, perfect anisotropic etching of the surface, the observed lateral thickness variations can account for the roughness development of the nanomask given in Table 3.2. In this ideal case the maximum achievable nanomask roughness $R_{a,NM}$ after one cycle can be calculated as follows:

$$R_{a,NM} = S_{Si,FC} * R_{a,FC} \quad (3.2)$$

One can assume that lateral differences in the chemical structure, as indicated by the phase information of the AFM scan, are attributable to a difference in local etch rates of the film, thus enhancing the roughness development. In contrast to this, it is stated that SF_6 etching in c-DRIE has a strong isotropic component and lateral etching quickly removes spikes and tips, smoothing the surface after all of the inhibiting FC-film is stripped. That is why exact timing is crucial to prevent excessive lateral etching and provide sidewall passivation of the features in the subsequent steps.

Bigger particles are also found scattered across the wafer, see Figure 3.18 (lower left corner). These particles are either dust contaminants or larger particles originating from the C_4F_8 plasma. The aspect of plasma dust affecting the nanomask is discussed in detail in Section 3.4.1.

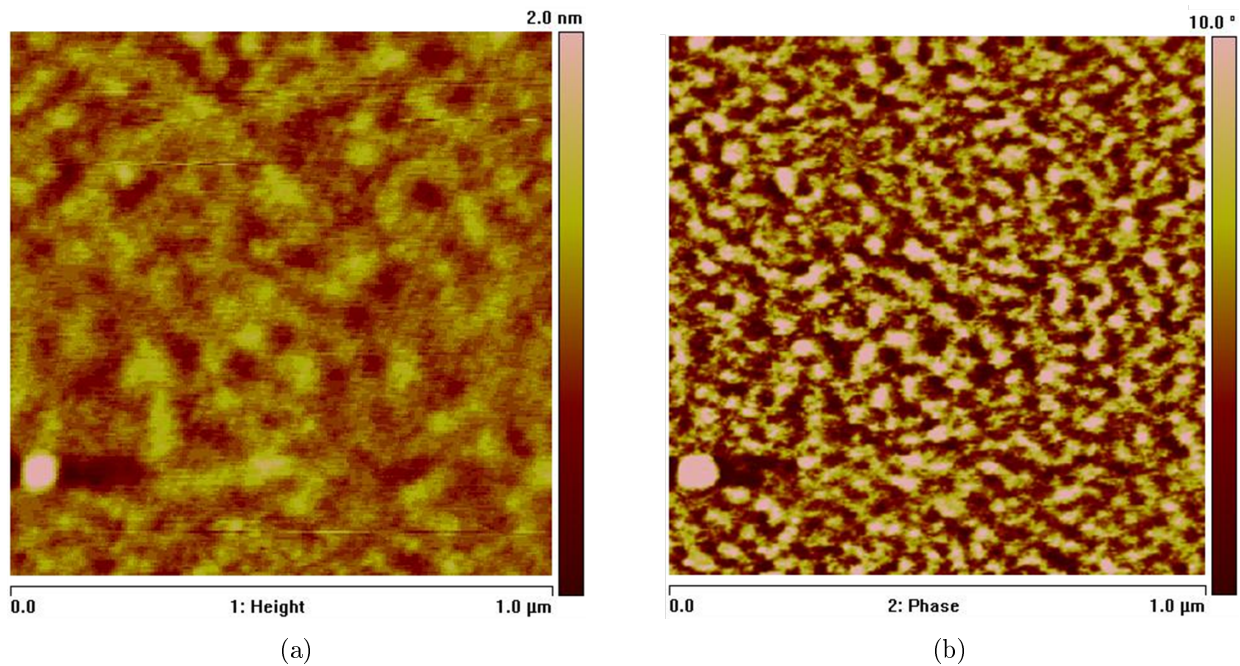


Figure 3.18: AFM scan of deposited FC-film for a) height and b) phase.

It is known that FC-film deposition by C_4F_8 is characterized by an anomalous roughness scaling [BK08]. BALONIAK *et al.* reports a change of surface morphology from a fine grainy to a larger clumpy structure with deposition time, respectively film thickness. As it is shown in Section 3.3.5, this effect can be used to generate different nanomasks with varying density.

Deposition Rate

Different plasma regimes and their associated deposition precursor molecules cause changes in deposition rate. Figure 3.19 plots the deposition rate as a function of coil power P_c , pressure p and substrate temperature T_S . A linear relationship is found for the increase of coil power, indicating a higher deposition with the increase of free radicals. For the pressure variation, the deposition rate is about 1.4 nm s^{-1} for 0.8 Pa and 2.5 Pa . As the pressure is increased to 5.3 Pa the deposition rate drops significantly to about 0.8 nm s^{-1} . This shows that an increased concentration of sufficiently dissociated precursor molecules is important to achieve high deposition rates.

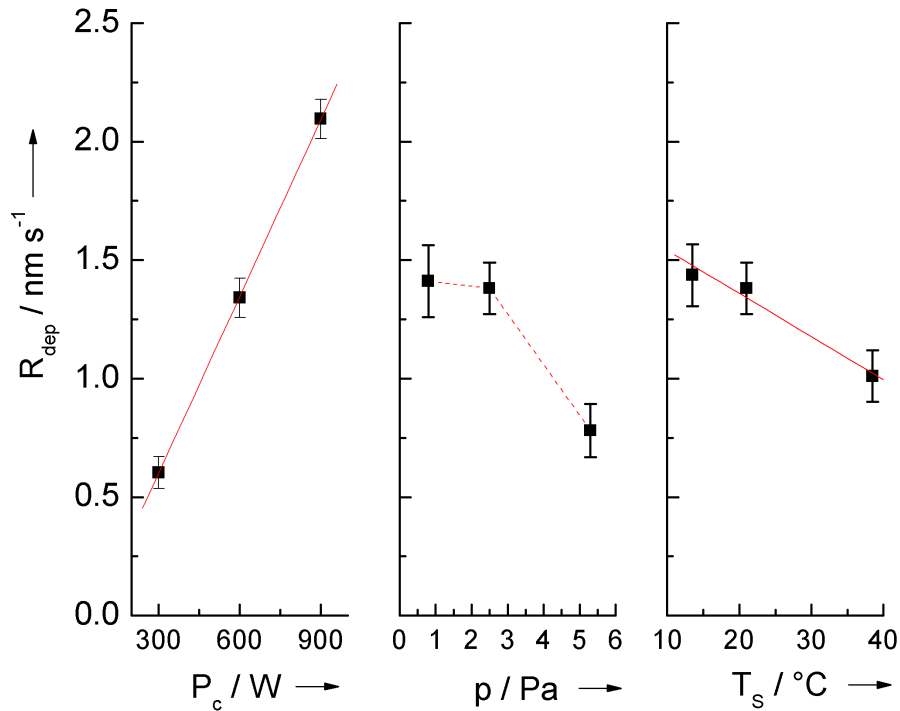


Figure 3.19: Deposition rate R_{dep} as a function of coil power P_c , pressure p and substrate temperature T_s .

A negative effect of an elevated substrate temperature on the deposition rate has been found. D'AGOSTINO *et al.* concludes from similar results in [d'A90] that a higher surface temperature reduces the deposition rate as the ratio of adsorption-desorption and the chemical surface reactions are changed.

The deposition rate is a complex function of various plasma parameters. It depends on the feed of polymerizing precursor molecules affected by radical density and the dissociation-recombination equilibrium (influenced by power, pressure, flow rate), the properties of the radicals (e.g. sticking coefficients), the occurrence of excited surface sites (influenced by bias power and temperature) and the ratio of adsorption-desorption [d'A90].

It is noted that the deposition rate is measured at FC-films, which are deposited for 100 s at the specific process settings, resulting in thicknesses greater 50 nm. Because the chemical structure of thin ($< 10 \text{ nm}$) FC-films is significantly different from bulk FC-films ($> 50 \text{ nm}$), the deposition mechanism and the deposition rate can change. A more detailed discussion of the deposition rate in combination with the corresponding FC-film etch rate is necessary for the nanomasking and is found in Section 3.3.4.

3.3.3 Etching

During etching the passivation is removed and the nanomask appears at the end of the step. As has been shown by XPS analysis (see Section 3.2.2), the remaining clusters are carbon-rich thus providing high selectivity for the subsequent *Si* etching and acting as nuclei for Silicon Grass generation. In standard c-DRIE these clusters are etched away by a stronger or prolonged etching to prevent them from masking. The process also uses a percentage of *O* (usually 10 – 20%) so that oxidizing reactions participate in removing the *C*. Consequently, to effectively generate the Silicon Grass without consuming much of the *Si*, the etching step must be stopped after the nanomask has developed but before the clusters are removed completely.

At the end of etching the surface morphology changes within a small time frame of one to two seconds. The process can be divided into different phases. At first, the film is considered as one single cluster. Before it is completely removed it becomes porous. Then the etched holes develop into trenches which subsequently join each other and separate parts of the remaining film. An amorphous surface structure emerges which closely resembles the morphology of the FC-film. As etching continues, the structures are broken up into smaller fractions. Finally, the structures get smaller until they are etched away completely. An illustration of the process is given in Figure 3.20, demonstrating the Area coverage V and density D as functions of time at the end of the etching step. It is seen that maximum density is reached for $V \approx 0.2 - 0.3$.

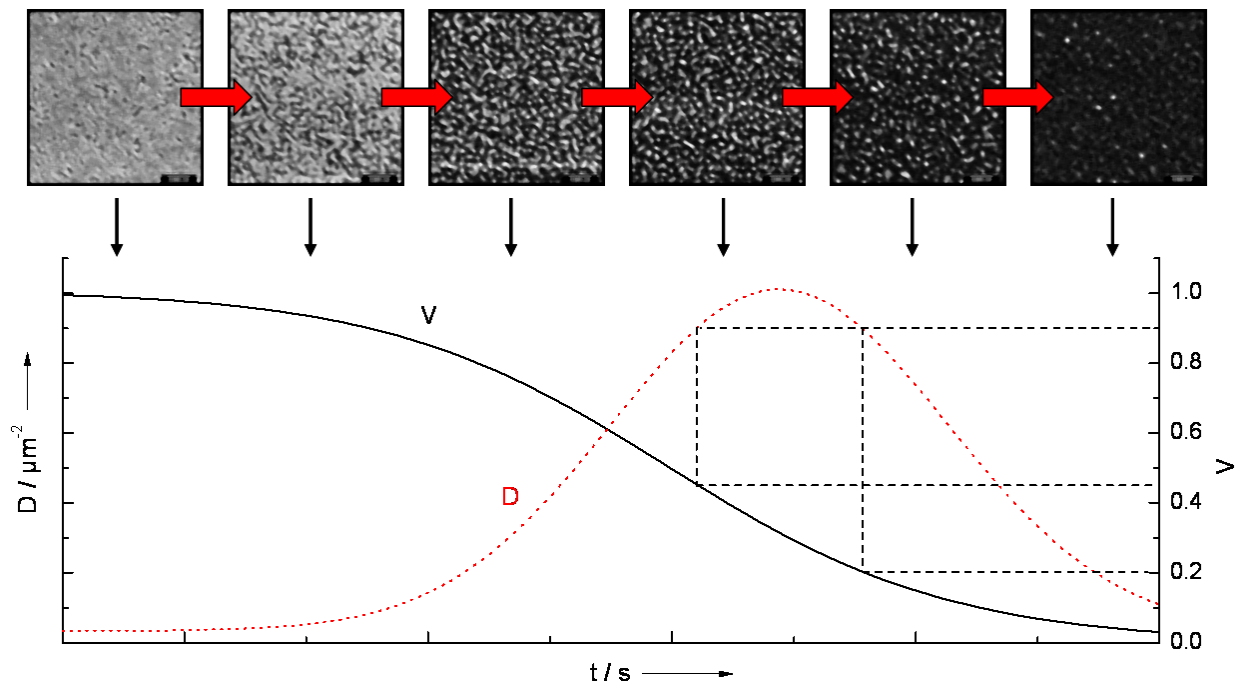


Figure 3.20: Sketch of morphological change of the FC-film at the end of the etching step.

In order to find the right time for switching, *in situ* monitoring of the process is necessary. The initial approach uses online observation of the processed wafer and is performed with a digital camera, the second method uses OES spectroscopy as an end-point detection system.

Visible Changes

Since nanomasking generates a strong surface roughness, a change in reflection is visible to the naked eye. For optimal conditions the change in reflection, which progresses from the edges to the center of the wafer, is noticed after two cycles at the end of etching, see Figure 3.21. The images show a top view of the wafer during the etching step. On the left-hand side the pins from the mechanical clamping system and the clamping ring are visible. Furthermore, the camera viewport, the circular gas-inlet port and some screws on the inside of the chamber lid are seen reflecting off the polished wafer surface in the first frame. It is observed that the change in reflection is inhomogeneous and affected by the clamping pin positions. At the end of the etching the surface appears dull and the formerly clear reflections are not visible anymore.

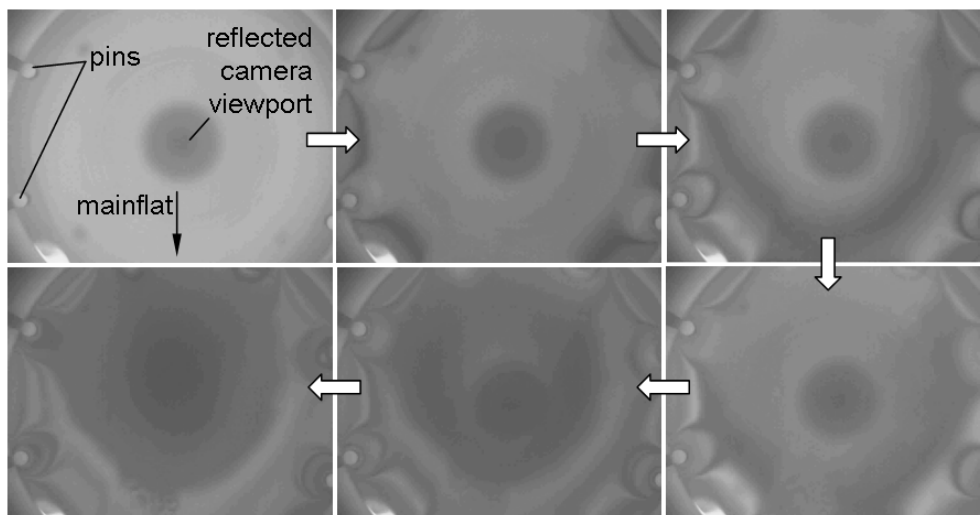


Figure 3.21: Change in reflection at the end of the etching step.

The method is a useful procedure to find the appropriate nanomasking process window for different parametrical settings and has been applied in the experimental studies to determine parametrical influences in Section 3.3.5. However, in regard to the integration in manufacturing processes, OES spectral analysis for end-point detection is more precise to find the right working point.

OES Analysis

Figure 3.22 shows different OES spectra at the beginning and end of the etching step in the Silicon Grass process (FC-film). For comparison a spectrum of etching SiO_2 with SF_6 (oxide) shows the spectral differences and enables identification of the characteristic F , SF_x and S lines.

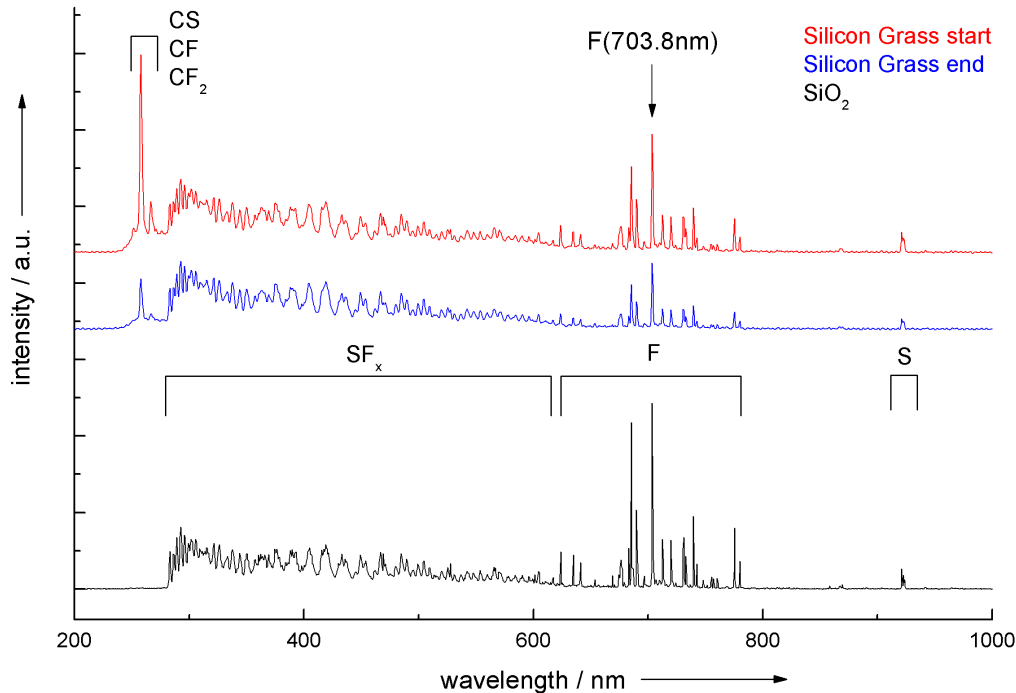


Figure 3.22: OES spectra of FC-film and oxide etching with SF_6 .

The parameters used are given in Table 3.5 (Silicon Grass process).

A significant change for the emissions from 238.7 nm to 281.4 nm occurs. They are assigned to CF , CF_2 and CS radical emissions [PG76]. The identification for F , S and SF_x is taken from [AML86]. Furthermore, a drop in F emissions is noticed.

For a more detailed examination of the changes during cycling, the characteristic lines for $F(703.8\text{ nm})$ and $CS(257.6\text{ nm})$ of a Silicon Grass process are plotted as a function of time and compared to those of a normal c-DRIE process for deep Si etching, see Figure 3.23. The process parameters are given in Table 3.5. No O_2 is added in the Silicon Grass process. Therefore, the etch step time is reduced to $\tau_{etch} = 9\text{ s}$. After an initial peak, which is attributed to gas switching and the associated mechanisms of pressure control and impedance matching, a continuous decrease of the emission intensity of $CS(257.6\text{ nm})$ in the etching step is observed for both settings. In contrast to the Silicon Grass process, the line in c-DRIE decreases more rapidly and, as it approaches zero, levels in a type of $1/x$ function, indicating the removal of C and CF_x from the substrate and the reactor walls in the prolonged etching step. The greater gradient is explained by the higher coil power setting in the c-DRIE.

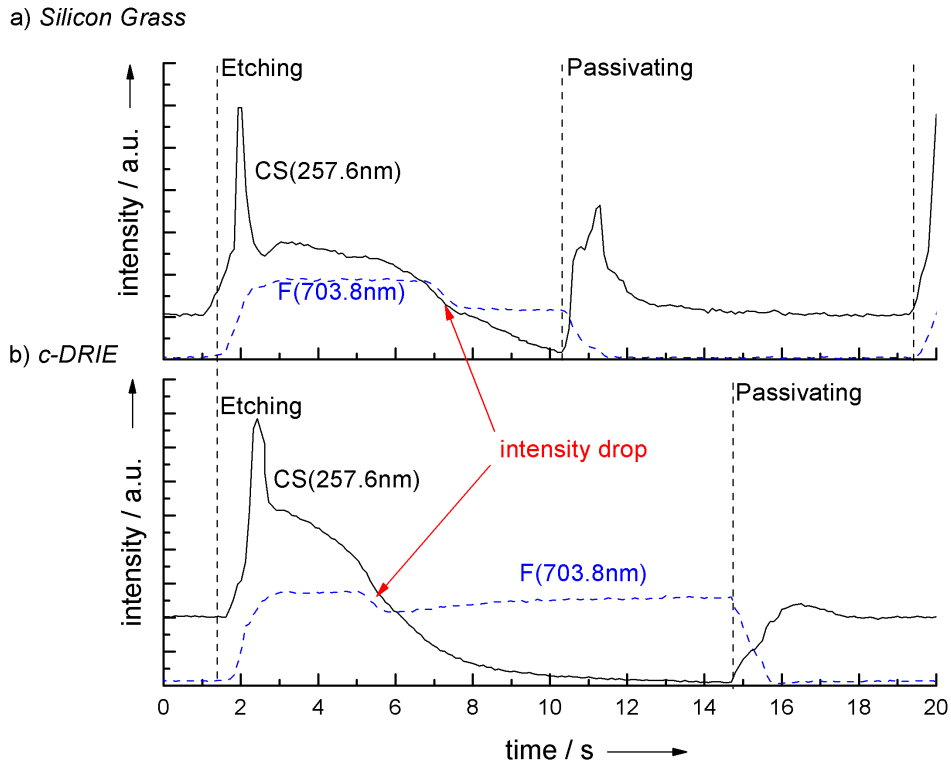


Figure 3.23: $F(703.8\text{ nm})$ and $CS(257.6\text{ nm})$ emissions during etching for a) the Silicon Grass and b) the c-DRIE process.

Table 3.5: Silicon Grass and normal c-DRIE process parameters.

Parameter	Silicon Grass process		c-DRIE	
	passivation	etching	passivation	etching
$Q_{C_4F_8}$ (sccm)	85	—	85	—
Q_{SF_6} (sccm)	—	143	—	130
Q_{O_2} (sccm)	—	—	—	13
τ (s)	9	9	7	13
P_c (W)	450	450	600	600
P_b (W)	—	12	—	18
p (Pa)	2.5	4.3	2.5	4.3
T_C ($^{\circ}C$)	40			
T_S ($^{\circ}C$)	20			
Process time (min)	25			

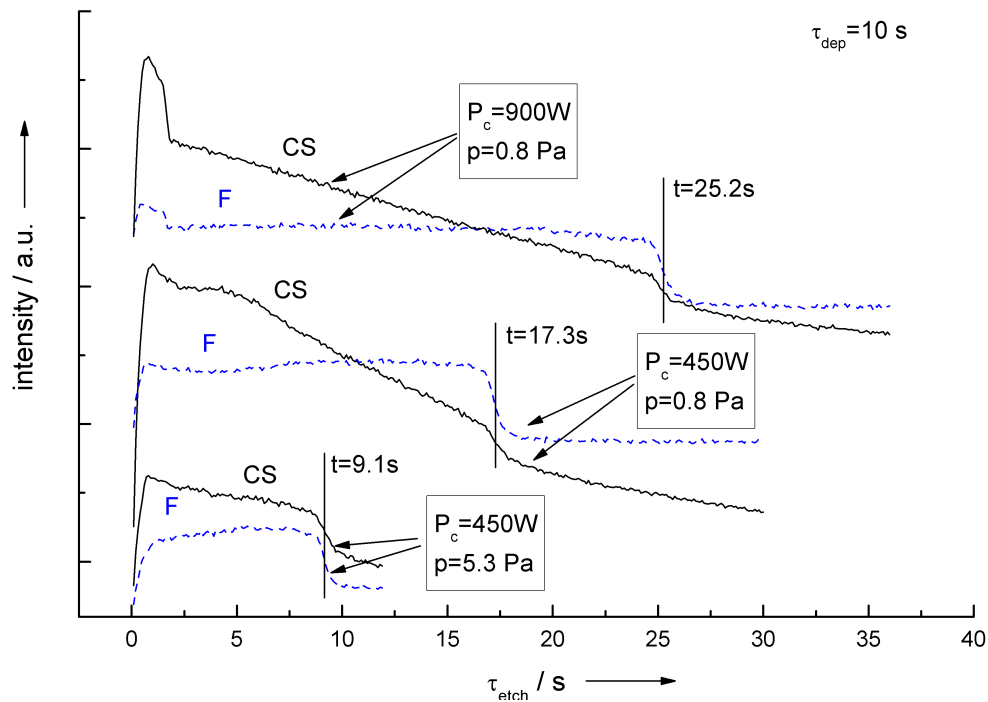


Figure 3.24: $F(703.8\text{ nm})$ and $CS(257.6\text{ nm})$ emissions during etching FC-films deposited at different passivation settings. Etching is performed according to Table 3.5 (Silicon Grass process).

In both settings a sharp decrease in $F(703.8\text{ nm})$ emissions at a distinctive time is seen. This indicates that at this particular point the FC-film becomes porous and Si etching starts, scavenging free F and thus causing the intensity drop. At this moment the change in morphology of the FC-film sets in and develops into the nanomask. After this, continued etching leads to a smoothing and leveling of the roughened surface.

Depending on the parametrical settings of the passivation step, the decrease occurs at different times corresponding to the particular deposition thickness, see Figure 3.24. The findings are also in agreement with the observation of reflection change for the different parameter settings, which are measured at the corresponding times of 9 s (450 W , 5.3 Pa), 17 s (450 W , 0.8 Pa) and 25 s (900 W , 0.8 Pa).

Etch Rate

Because the parametrical study in Section 3.3.5 uses bias power as a variation parameter, the influence of bias power on the FC-film etch rate is studied. A linear relationship is found, see Figure 3.25. For the measurements a thick FC-film (several 100 nm) is deposited and subsequently etched with the varying parameters.

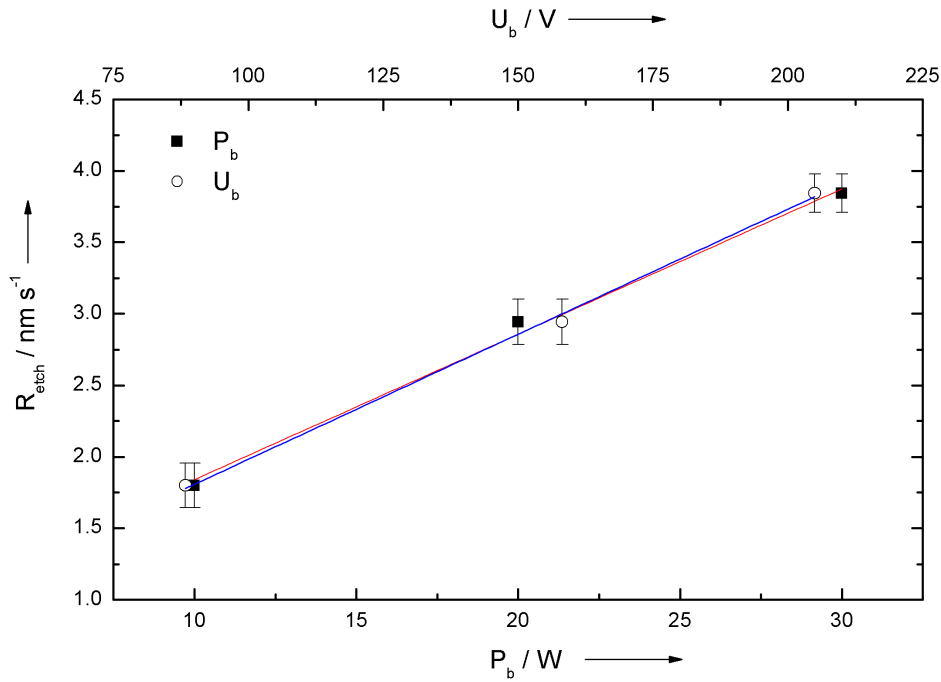


Figure 3.25: FC-film etch rate as a function of bias power P_b and corresponding bias voltage U_b . The parameters used are given in Table 3.5 (Silicon Grass process).

As shown by the chemical analysis in Section 3.2.2, the chemical structure of the solid FC-film and the thin deposited film during cycling is different, so that etch rates can also vary. Therefore, the measured etch rate is valid for thick, homogeneous films and must be corrected for the purpose of nanomask generation which is discussed in Section 3.3.4.

Parametrical influences on the etch rate of Si in c-DRIE processes are studied extensively [JBU⁺09] and therefore do not form a part of this work. However, because Si is etched between the remaining clusters, the Si etch rate and the etch anisotropy have an influence on the roughness development and thus nanomask formation. In this context, it should be considered that a higher etch rate is often accompanied by a greater inhomogeneity, promoting a non-uniform nanomask development and making it more difficult to find the exact timing for switching.

3.3.4 Controlled Nanomasking

Nanomasking in c-DRIE processes is achieved when etching and passivation are balanced and the inhibiting film is not fully removed at the end of etching. For a given set of process parameters the minimum step duration for etching, which in the following is labeled as critical etch step time τ_{crit} , must be found.

Passivation and etching yield must be equal,

$$z_{dep} = z_{etch,inh} \quad (3.3)$$

with z_{dep} being the deposited film thickness and $z_{etch,inh}$ being the etching yield of the inhibiting layer. Substituting the time dependent deposition and etch rate results in:

$$\int_{\tau_{dep}}^0 R_{dep}(t)dt = \int_{\tau_{crit}}^0 R_{etch,inh}(t)dt \quad (3.4)$$

To calculate the corresponding critical etch step times for every parametrical setting, the functions for $R_{dep}(t, p_1, p_2, \dots, p_n)$ and $R_{etch,inh}(t, e_1, e_2, \dots, e_n)$ must be known, integrated and solved for τ_{crit} . As parametrical influences are complex due to non-linearities and interdependencies, this method turns out to be highly impractical.

Therefore, to determine the critical etch times for the parametrical experiments (Section 3.3.5), an empirical approach is conducted.

The critical etch step times τ_{crit} for the different process parameters deposition time τ_{dep} , coil power P_c and bias voltage U_b , are measured by varying the etch step until the $F(703.8 \text{ nm})$ intensity decreases. The resulting times are given in Figure 3.26 and Figure 3.27. Both line progressions in Figure 3.26 can be fitted with a linear approximation, which shows that τ_{crit} can be assumed proportional to τ_{dep} and inversely proportional to U_b .

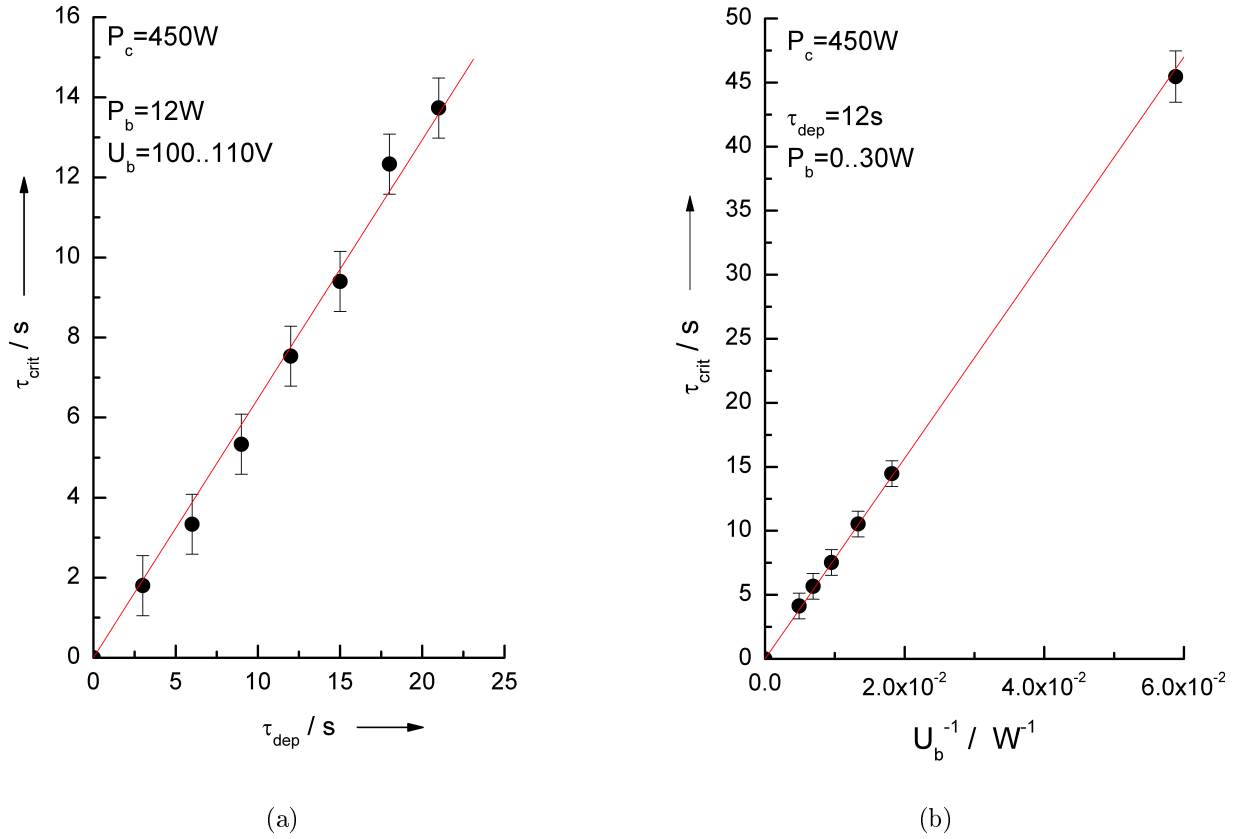


Figure 3.26: Critical etch time τ_{crit} as function of a) deposition time τ_{dep} and b) bias voltage U_b .

The dependency of τ_{crit} on the applied P_c during deposition is not linear for the range between 150 and 900 W but can be separated into two regimes of linear behavior, see Figure 3.27. The shift between the two regimes occurs at about 600 W which correlates to the observed regimes of high and low dissociation discussed in Section 3.3.2. Taking into account the linear increase of R_{dep} with P_c from Figure 3.19 and the linear increase of τ_{crit} with τ_{dep} from Figure 3.26, it is concluded that the lower gradient at higher powers is due to a higher etch rate of the FC-films deposited in the high dissociation regime. This conclusion is also supported by the fact that the FC-films of the high dissociation regime have a higher FC-ratio (see Section 3.3.2), indicating their lower etch resistance. At a lower power setting of 150 W the measured etch times become too short to be accurately measured. The linear fit cuts the x-axis at about 100 W, which is labeled as the minimum coil power $P_{c,min}$.

From the linear relationships an empirical equation is derived to calculate the critical etch time τ_{crit} :

$$\tau_{crit} = c_1 \tau_{dep} \frac{P_c - P_{c,min}}{U_b} \quad c_1 = 0.2 \quad (3.5)$$

However, utilizing the calculated τ_{crit} as the etch step time τ_{etch} does not result in effective Silicon

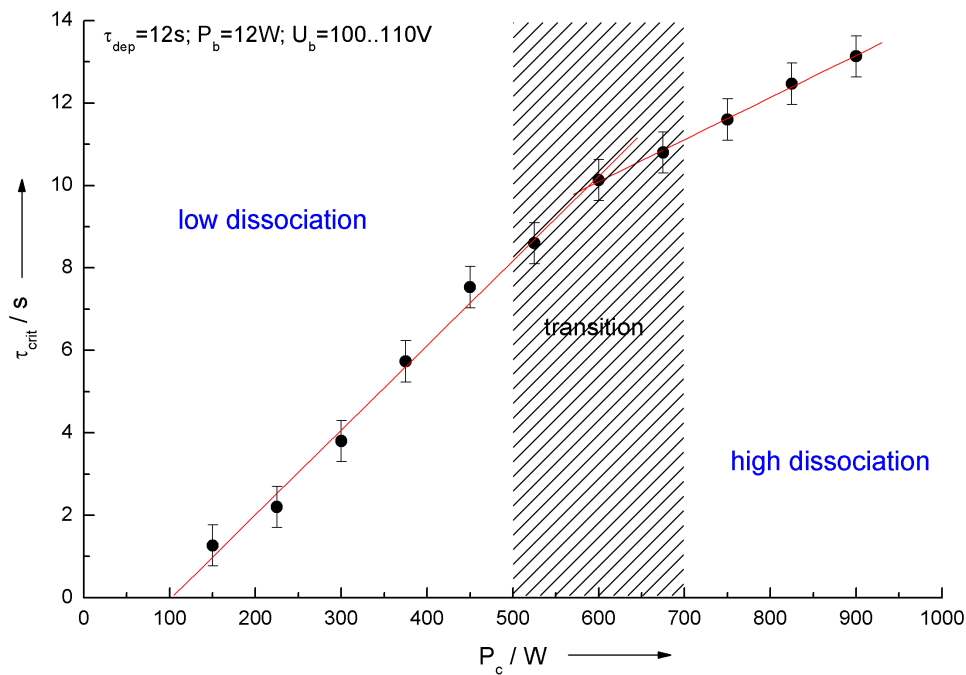


Figure 3.27: Critical etch time τ_{crit} as function of coil power P_c .

Grass generation, because it only equals the required etch step time minimum. Examining the surface after five cycles with $\tau_{etch} = \tau_{crit}$ reveals heavily passivated structures, indicating that the level of passivation is still too strong. Several performed experiments evidenced that the typical needle-shaped Silicon Grass is most efficiently generated when the etch step time is prolonged by 2 s. Hence, the optimum etch step time τ_{opt} for $150 < P_c < 650$ W is found to be:

$$\tau_{opt} = \tau_{crit} + 2 \text{ s} \quad (3.6)$$

In order to find the etching-passivation balance for any parametrical combination, the use of *in situ* OES with online end-point detection for each step is advised. It is noted that this method works well for a high silicon load, since the $F(703.8 \text{ nm})$ intensity drop is more pronounced if more *Si* is exposed to etching as the inhibiting film is removed. The method is also discussed for the generation of Silicon Grass on masked substrates, covered in Section 3.4.4.

3.3.5 Parametrical Study

An experimental study is conducted to clarify, if the morphology can be influenced by parametrical variations to set up specific geometrical properties of the nanomask [Leo08]. Thereby it is identified whether this modification is governed by a) passivation or b) etching.

If a large number of influencing factors and interdependencies is assumed (e.g. chemical process analysis, genetic experiments or plasma processes), the complexity of the experimental design is very high. In such cases the Design of Experiments (DoE) method is an adequate tool to find an appropriate experimental design and to maximize information with a minimum number of tests.

A subset of three parameters is selected, which affect the deposited FC-film thickness z_{dep} (deposition step duration τ_{dep}), the chemical composition of the FC-film (coil power during passivation P_c) and the kinetic energy of the bombarding ions during etching (bias power during etching P_b). In the case of a), τ_{dep} and P_c have a great effect on the nanomask. If bias power P_b during etching is most influential, b) is considered. Additionally, the deposited film thickness z_{dep} in each passivation step is assumed to be one of the most potent parameters to influence the nanomask morphology because of its anomalous roughness scaling [BK08].

The minimum and maximum values of the input parameters that bound the process window of interest are defined considering the process parameters of standard recipes for c-DRIE etching, the limits of the system used and the experience of process engineers, who have been using the Silicon Grass process for several years.

The morphology of the nanomask is inspected via SEM after a process of five cycles with the different settings. At that point the nanomask is transferred into the *Si* (see Section 3.2.1). From the pictures several output parameters are derived characterizing the morphology of the nanomask. Density D is a characteristic and important surface property and is therefore chosen as output parameter x for the study.

As discussed in Section 3.3.4, each parametrical setting requires a specific, adapted etch step time τ_{etch} , which allows for the nanomask to occur. At the time of the study the relation given in Equation 3.5 yet unknown. Therefore, τ_{etch} was determined by measuring the etch step duration until the visible change in reflection occurs, described in Section 3.3.3. Applying the method, it is found experimentally that τ_{etch} can be expressed by:

$$\tau_{etch} = \tau_{dep} \left(\frac{p_1 + p_2 P_c}{e_1 + e_2 P_b} \right) \quad (3.7)$$

with $p_1 = 3.05 \cdot 10^{-1} \text{ nm s}^{-1}$, $p_2 = 2.75 \cdot 10^{-3} \text{ nm W}^{-1} \text{ s}^{-1}$, $e_1 = 9.49 \cdot 10^{-1} \text{ nm s}^{-1}$ and $e_2 = 8.07 \cdot 10^{-2} \text{ nm W}^{-1} \text{ s}^{-1}$.

Mathematical Model and Experimental Design

Because of the complexity of the process a model with linear and quadratic terms is chosen:

$$\hat{x} = a_0 + \sum_{i=1}^4 (a_i u_n + a_{ii} u_i^2) \quad (3.8)$$

It includes the four input parameters ($u_1 = \tau_{dep}$, $u_2 = P_c$, $u_3 = P_b$ and $u_4 = \tau_{etch}$), the output parameter x and the linear (a_i) and quadratic (a_{ii}) model parameters with an offset (a_0). Because u_4 is not independent it is substituted in 3.8 with 3.7:

$$\hat{x} = a_0 + \sum_{i=1}^3 (a_i u_i + a_{ii} u_i^2) + a_4 u_1 \left(\frac{p_1 + p_2 u_2}{e_1 + e_2 u_3} \right) + a_{44} u_1^2 \left(\frac{p_1 + p_2 u_2}{e_1 + e_2 u_3} \right)^2 \quad (3.9)$$

A composite experimental design for input parameters with linear, quadratic and mixed terms has been proposed by Hartley *et al.* [Wer89] [Har59]. It uses four core points for the factorial experiments and seven star points including the zero point for three independent input parameters, see Figure 3.28. The individual values of the different tests are shown in the experimental table, see Table 3.6.

Table 3.6: Experimental table [Leo08].

	u_1 in s	u_2 in W	u_3 in W	u_4 in s	x in μm^{-2}	\hat{x} in μm^{-2}	Δ
DoE 0	10	450	18	6.5	26.3	24.5	-6.70%
DoE 1	11	600	24	7.5	16.9	15.1	-10.20%
DoE 2	11	300	12	6.5	17.9	18.3	2.10%
DoE 3	9	600	12	9.2	25.2	23.3	-7.40%
DoE 4	9	300	24	3.5	26.3	26.0	-1.20%
DoE 5	11.4	450	18	7.4	13.6	14.1	4.40%
DoE 6	8.6	450	18	5.6	21.3	22.5	5.50%
DoE 7	10	662	18	8.9	14.5	16.7	15.00%
DoE 8	10	238	18	4	18.4	17.9	-2.30%
DoE 9	10	450	26.5	5	25.4	26.5	4.20%
DoE 10	10	450	9.5	9	31.2	31.9	2.20%

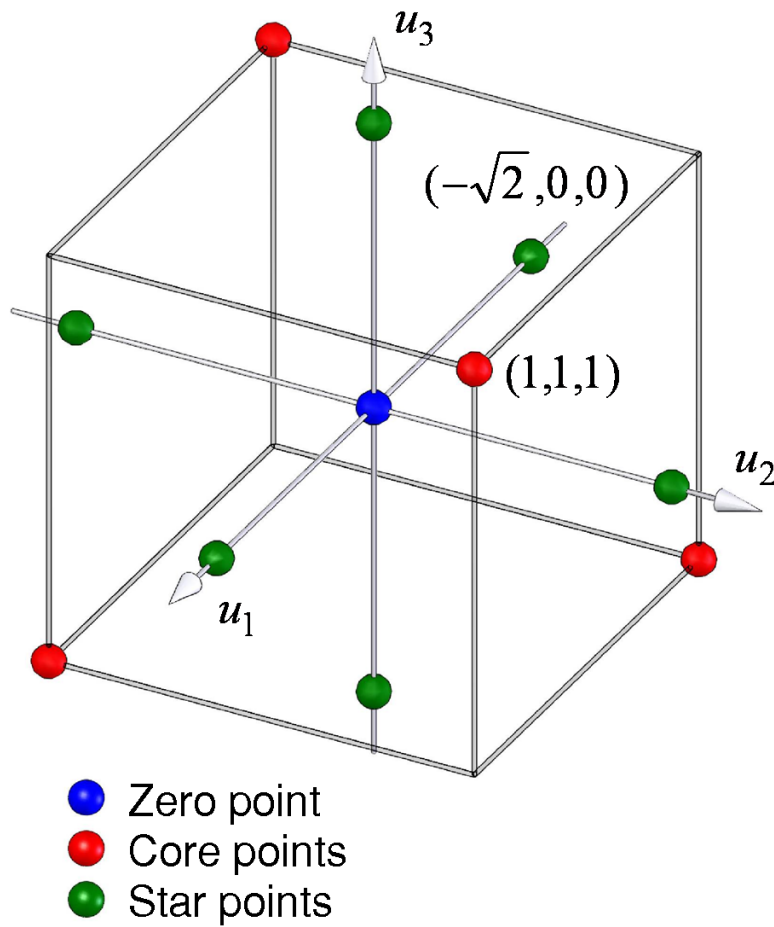


Figure 3.28: Three-dimensional experimental space [Leo08].

Preconditioning and Setup

To guarantee reproducible results, the ICP system is preconditioned with an oxygen cleaning and a subsequent Silicon Grass process. The cleanliness of the chamber is controlled by OES spectrometry, which showed no significant change of the spectrum after ten minutes of cleaning at $P_c = 800\text{ W}$, $Q_{O_2} = 45\text{ sccm}$, $p = 2.7\text{ Pa}$. Then a Silicon Grass conditioning process is performed for ten minutes and guarantees the process chamber coating being of similar type in all experiments.

As temperature changes have an impact on the etching passivation equilibrium, the changing process chamber temperature during processing must be considered. Equal starting temperatures for each process are ensured by controlling the chamber temperatures with the installed pyrometer before running each test. However, it must be noted that different parameter settings lead to different temperature progressions in each test, so that the influence of temperature can not be ruled out completely. To account for the radial inhomogeneity, which is discussed in Section 3.2.1, the measurements are always performed at a specific radial wafer position of $R = 40\text{ mm}$.

Test substrates are single-side polished (100) *Si* wafers with a diameter of 100 *mm*, a thickness of 525 μm and a resistivity of 7 – 13 $\Omega\text{ cm}$. The wafers are not subjected to an RCA cleaning prior to processing. It is found that organic contaminates have no significant influence on the nanomasking process, see Section 3.4.3. The natural oxide film plays a role but is not necessary for the nanomask to occur. It merely enhances the process because of the higher selectivity of SiO_2 relative to *Si* in contrast to carbon residues relative to *Si*. The influence of nature oxide is discussed in Section 3.4.2.

After processing, the wafers are fragmented and inspected by SEM. The properties of the structures are analyzed by the digital image processing methods of SEM pictures (Image Pro Plus®, Media Cybernetics). Since SEM image contrast and brightness settings can differ slightly from image to image, a best-fit contrast equalization is performed prior to the measurements. An illustration of the measurement procedure is given in Figure 3.29.

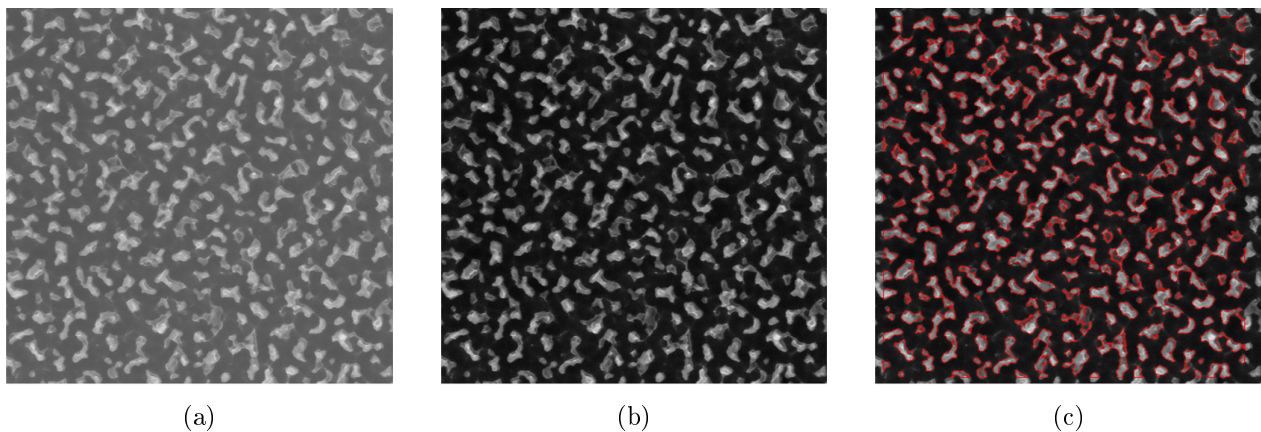


Figure 3.29: Measurement procedure: a) original SEM image, b) contrast equalization and c) automatic particle measurement.

Results and Discussion

SEM analysis reveals distinct differences of the surface morphology after the five cycle nanomasking process. Figure 3.30 shows two characteristic examples for different morphologies of a high density with small structures and of low density with bigger ones.

To evaluate the reproducibility, the process is executed three times with the same input parameters (DoE 3) as a repeatability test. The densities measured at $R = 40\text{ mm}$ are 21.8, 23.5 and 21.9 μm^{-2} respectively, from which follows a standard deviation of approximately 1 μm^{-2} .

After acquiring the densities for all experiments the model parameters are solved by regression (method of least squares). Table 3.6 lists the parameter sets with measured and calculated density and their

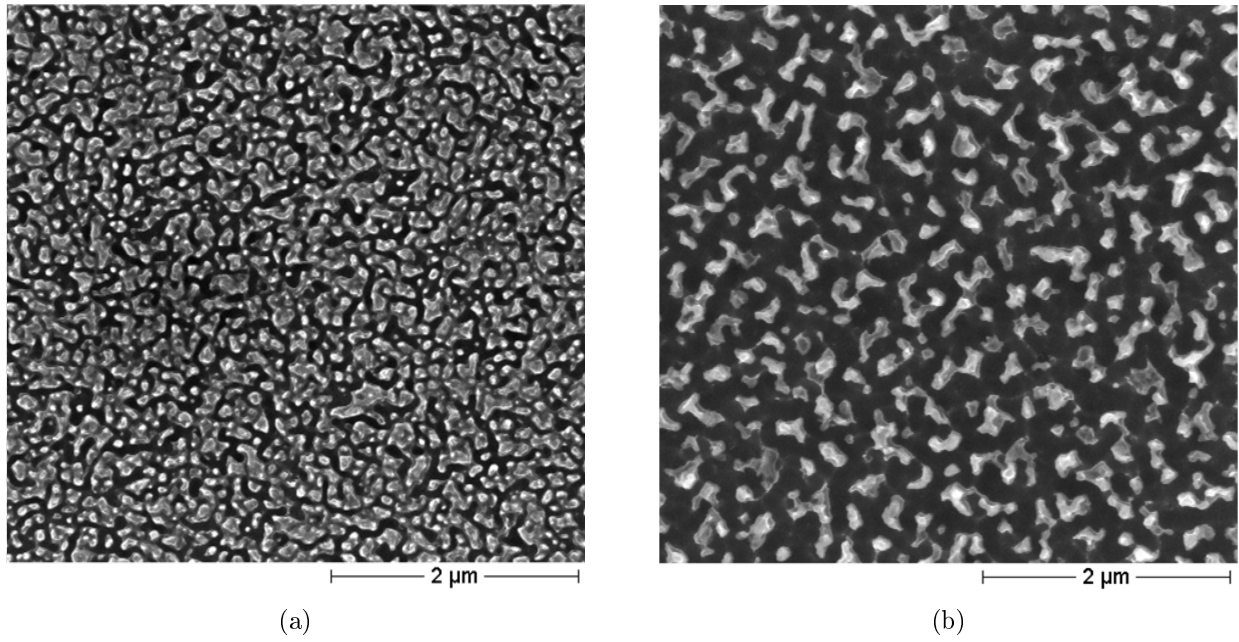


Figure 3.30: Different morphologies after the five cycle nanomasking process. [Leo08]

deviation for each experiment. The deviation for the tests with high values of P_c are highest. This is assumed to be an effect of the non-linear behavior of deposition if $P_c > 650 W$ (see Figure 3.27). The resulting model parameters are given in Table 3.7.

Table 3.7: Calculated model parameters. [Leo08]

Model parameter	value	unit	corresponding process parameter
a_0	-3564	-	-
a_1	610	s^{-1}	τ_{dep}
a_2	-3.55	W^{-1}	P_c
a_3	50.2	W^{-1}	P_b
a_4	425	s^{-1}	τ_{etch}
a_{11}	-41.8	s^{-2}	τ_{dep}
a_{22}	$2.55 \cdot 10^{-4}$	W^{-2}	P_c
a_{33}	0.19	W^{-2}	P_b
a_{44}	-18.7	s^{-2}	τ_{etch}

To visualize the influences on nanomask density, the relation given in Equation 3.9 is plotted for the combination of the three independent parameters, see Figure 3.31.

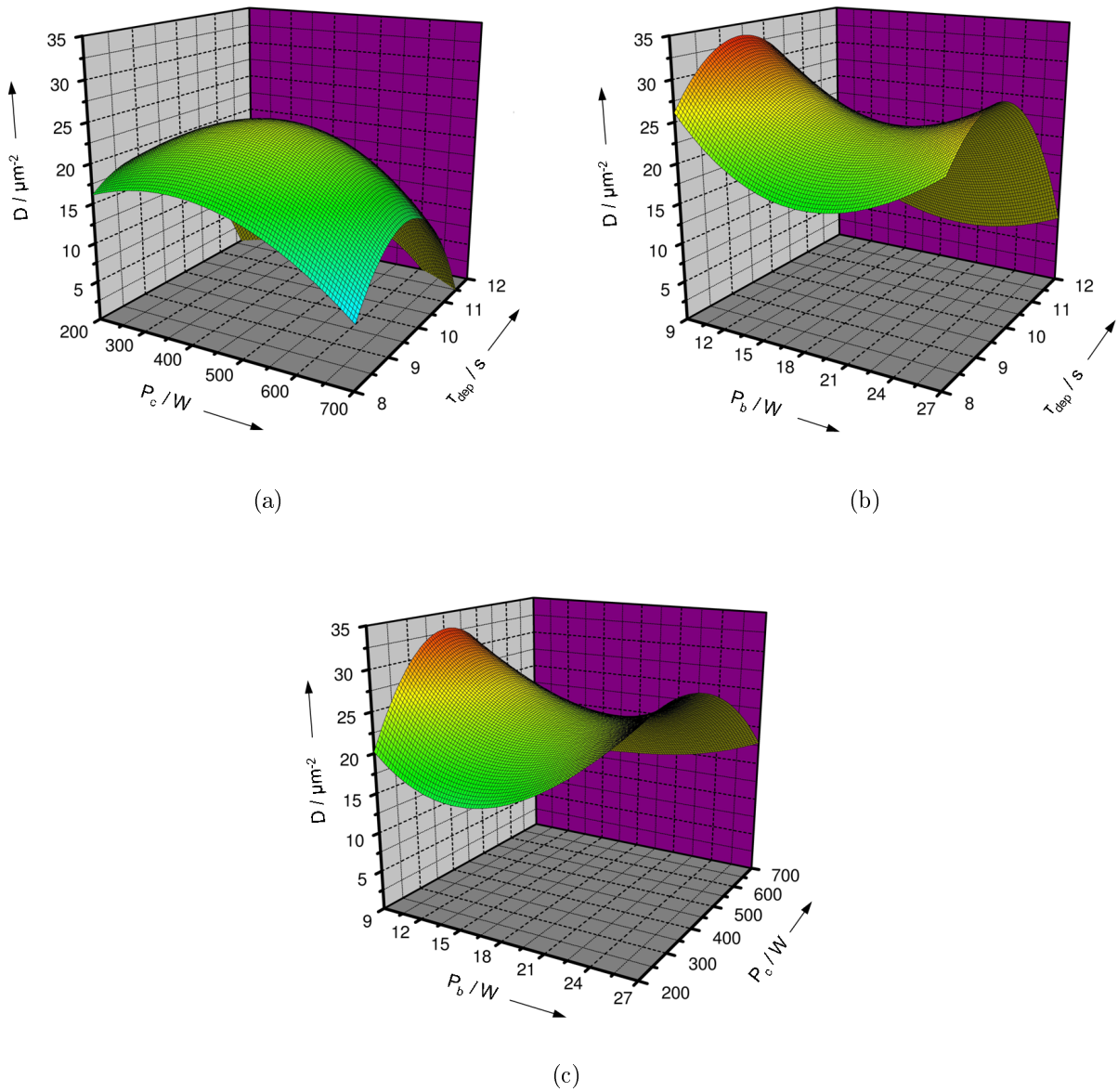


Figure 3.31: Dependencies of τ_{dep} , P_c and P_b on nanomask density [Leo08].

From the experimental study several conclusions for the nanomasking process can be drawn. First, it is found that the morphology, respectively density, of the nanomask can be changed by a variation of process parameters. For all tests the density D varies between $14.1 \mu\text{m}^{-2}$ and $31.9 \mu\text{m}^{-2}$ at an equal value for area coverage A , whereas the geometry of the analyzed structures closely resembles the amorphous structure of the carbon filaments, described in Section 3.2.1. The deposition step time τ_{dep} (u_1) is the most prominent parameter affecting the surface morphology of the nanomask, which

implies influence of the passivated FC-film thickness z_{dep} . Coil power P_c (u_2) also has an influence on the morphology, although its impact is considerably smaller. The results further indicate that bias power P_b has only a small effect on the morphology of the nanomask.

The findings show that a morphological definition via the deposited FC-film during the passivation step is most effective. On the one hand, the morphological and chemical configuration of the deposited carbon-rich film of the initial passivation steps (the first two cycles) defines the primary cluster distribution. On the other hand, the inhibitor has an important part in protecting the generated surface structures from lateral etching and prevents the re-smoothing of the surface.

3.4 Influences on Nanomasking

Because nanomasking is caused by several different phenomena, the process is also influenced by a multitude of process conditions. In order to further specify the nanomasking in c-DRIE, a series of experiments is performed to clarify the impact of different process conditions. In the following sections the influence of carbon dust formation and film flaking (Section 3.4.1), oxidation (Section 3.4.2), contaminations (Section 3.4.3) and masking (Section 3.4.4) is discussed.

3.4.1 Carbon Dust Formation and Film Flaking

In addition to the carbon nano-filaments in Section 3.2.1 other phenomena known as ‘carbon dust formation’ or ‘film flaking’ can play an important role in nanomasking. Both effects are known to occur in plasma polymerization processes [LS72] [KBS74] [MIU04].

STOFFELS *et al.* studied polymerization reactions in RF fluorocarbon plasmas of CF_4 , C_2F_6 and C_4F_8 by electron attachment mass spectrometry [SST98]. They report the generation of large polymer molecules up to the detection limit of the spectrometer (500 *amu*), whereas the density of larger polymers decreases with the size of the parent gas and the degree of saturation by F . Another work covers the solid particle production in C_4F_8 plasmas [TT01a]. Here, a marked increase of particle production is reported for the pressure range higher than 6.7 *Pa* (50 *mTorr*), indicating that particle production also takes place at lower pressures. Measurement of these particles reveals a high number of $C-CF_x$ bonds, and the particles are expected to exhibit a higher thermal stability than the film. Being built into the deposited FC-film, the particles would thus act as nuclei for nanomask formation. A corresponding model for the gas phase reaction kinetics is given in [TT02].

Evidence for this mechanism is found by inspection of SEM images of an etched FC-film, see Figure 3.32. Because of non-uniform etching due to ion-shadowing from the clamping ring, a transitional region is identified in its vicinity. The lighter spots inside the FC-film are identified as incorporated clusters which are subsequently exposed. During the course of this work, also larger particles are found scattered across the wafer affecting the formed Silicon Grass. Figure 3.33 shows SEM images of the substrate after five cycles and 75 cycles of the Silicon Grass process. The distribution of the particles in Figure 3.33 a) resembles the distribution of the larger Silicon Grass of Figure 3.33 b).

An effect is observed for higher bias power $P_b > 12W$ settings during etching. This finding is supported in [MIU04], where it is reported that the formed particles are positively charged and attracted to the substrate when negative bias voltage is applied. Because the exchange of gases is long, compared to the instantaneous switching of the powered electrode during cycling, the applied bias voltage can have an effect on the deposition process by attracting formed agglomerates onto the substrate surface.

The images show that the influence of dust particles causes an inhomogeneity of the resulting Silicon Grass. It can be prevented if either bias power is kept below a certain threshold value ($\approx 12W$) or if a time delay is implemented as the process switches from passivation to etching to guarantee a complete exchange of the process gases.

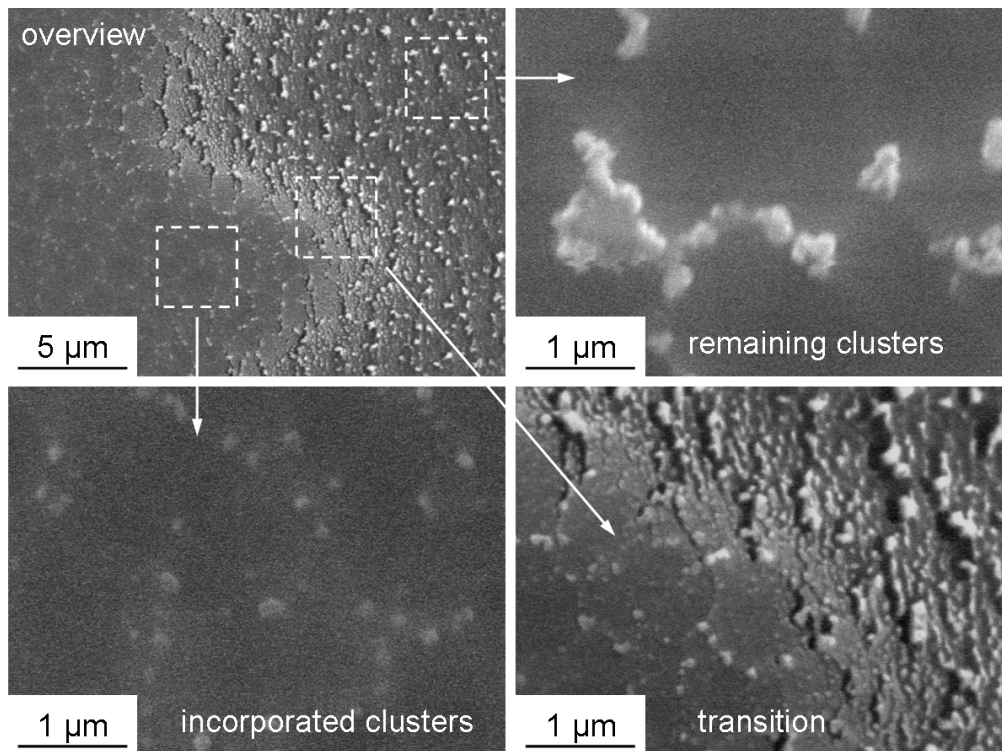


Figure 3.32: SEM images of a non-uniformly etched FC-film in the vicinity of the clamping ring. The images show that the clusters are already present inside the FC-film.

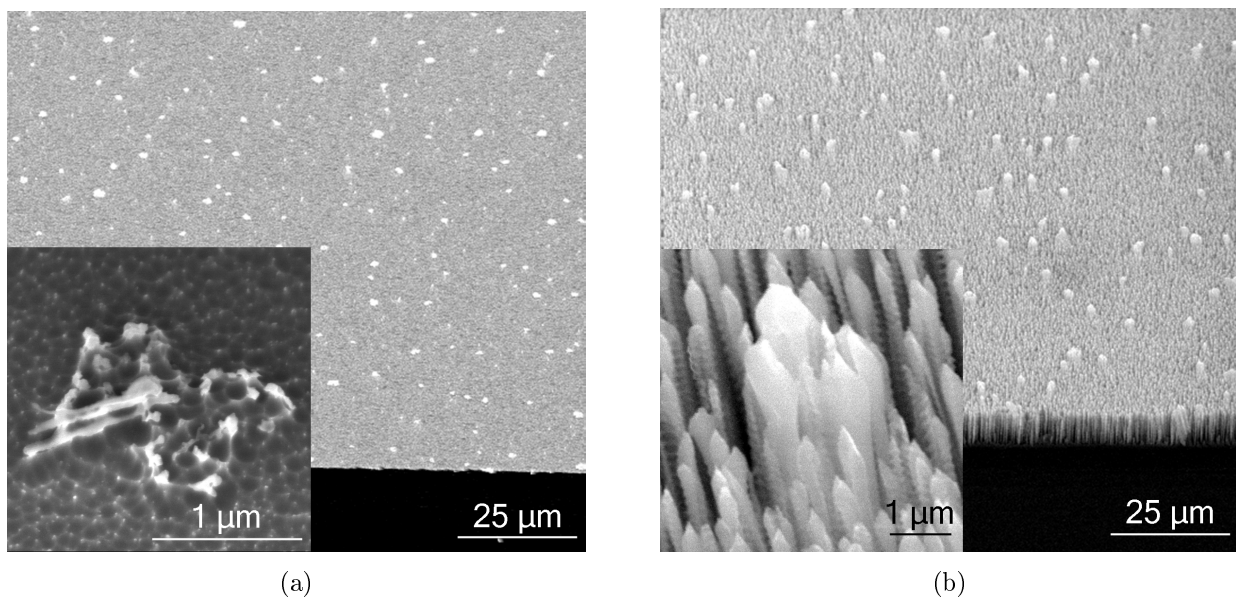


Figure 3.33: SEM images of a) carbon dust particles after five cycles and b) the resulting Silicon Grass structures after 75 cycles.

3.4.2 Oxygen

Natural Oxide

Because the selectivity of SiO_2 to Si is greater than the selectivity of C_xF_y to Si the natural oxide plays a role in starting the nanomasking process. The XPS and AES studies in Section 3.2.2 proved that the natural oxide is still present in the five-cycle nanomask. In order to analyze its influence three wafers of the same batch are prepared. The natural oxide of two of the wafers is stripped by a dip in hydrofluoric acid (HF) prior to processing, while the third one remains untreated as a reference sample. The reference wafer and one of the HF -treated wafers are processed for two cycles in the nanomasking process and subsequently analyzed by SEM. In contrast to the reference wafer, no nanomask is found on the surface of the treated wafer. The second treated wafer is processed in the 75-cycle Silicon Grass process and also inspected via SEM. Both treated wafers are shown in Figure 3.34. Monitoring of the wafer surface during the process reveals that nanomasking sets in late in the process (> 50 cycles), as indicated by the change in reflection discussed in Section 3.3.3. A follow-up experiment with a treated wafer and a reduced critical etch time τ_{crit} from 9 to 7 s displayed nanomasking behavior after two cycles.

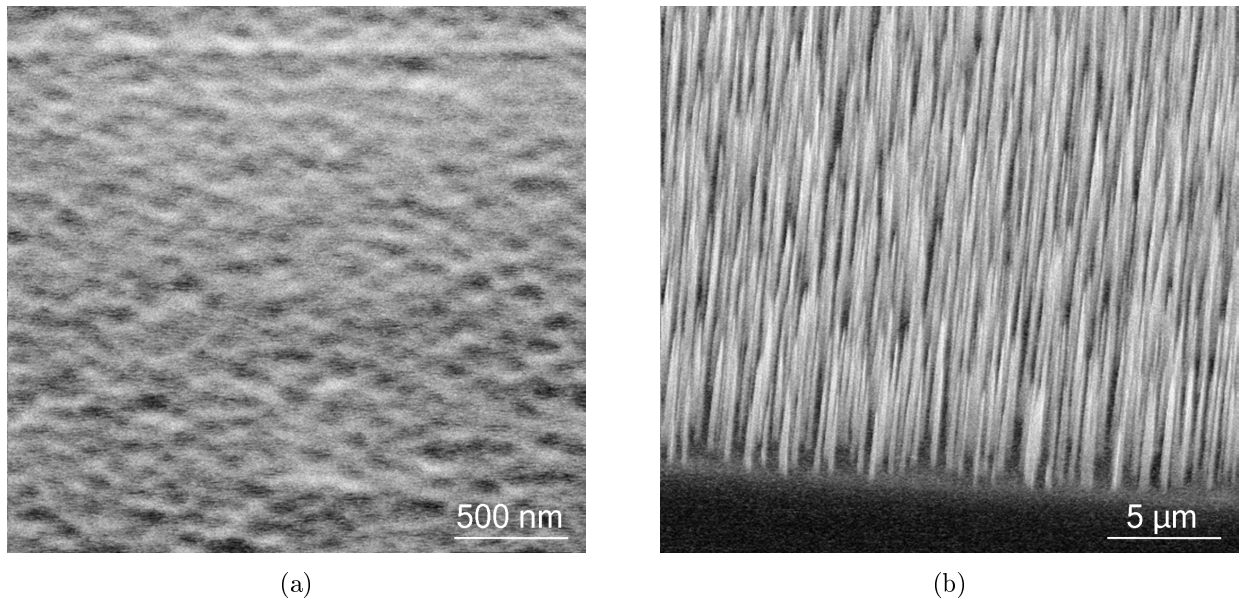


Figure 3.34: SEM images of HF treated wafers after a) two cycles and b) 75 cycles.

These findings show that the natural oxide is not necessary for the nanomask, but has a significant influence on the onset of its formation. It is assumed that the oxide aids the nanomasking process as etch products (e.g. SiO_2 or SiO_xF_y) are redeposited. SiO_2 provides a high selectivity ($> 100 : 1$) relative to Si in contrast to the selectivity of C_xF_y relative to Si . Another possibility is that the specific surface properties of the SiO_2 affect the FC-film when it is deposited in the first passivation step (e.g. provoking the formation of carbon nano filaments).

Oxygen Reactions

Adding about 10–20 % O_2 to SF_6 is common for the c-DRIE process, as it increases the F radical concentration and aids in removing the FC-film. Reaction products can also adsorb on the sidewalls, forming passivation films for lateral etch protection (see Section 2.1.3). The experiments show that no O_2 is necessary to create the nanomask, proving that passivation via SiO_2 and SiO_xF_y has no major part in nanomasking. Increasing the oxygen concentration shifts the plasma chemistry towards stronger etching, so that the etch step duration must be shortened by one to three seconds for an effective nanomask to occur.

3.4.3 Contaminations

Wafer Contamination

To rule out organic contaminants on the wafer surface as the source of the nanomask, a 10min cleaning in Peroxymonosulfuric H_2SO_5 acid is applied prior to processing. The wafers used are the same as in the experiments with natural oxide described in the previous section. After the treatment the wafers are rinsed in water (H_2O) and dried in a Quick Dump Rinser. During the 75-cycle Silicon Grass process the wafers exhibited no observable difference compared to the reference wafer. The change in reflection indicating nanomask generation can be observed for both samples after two cycles. SEM analysis of the resulting structures after the process also showed no significant difference. It is concluded that wafer contamination occurring during the handling of the wafers does not affect the nanomask.

Chamber Contamination

Another source for contamination is the plasma reactor itself when chamber materials are sputtered by the ion bombardment during processing. This is especially the case for CCP reactors where much higher bias voltages are present. The system utilized consists of a ceramic tube (Al_2O_3), a chamber lid and substrate electrode made of Al . Since Al compounds such as AlF_3 are reported to account for nanomasking [OSJ86], the possibility of sputtered Al which is subsequently fluorinated and deposited on the substrate has to be considered. However, the XPS overview spectrum in Figure 3.8 and the AES overview spectrum in Figure 3.11 of the nanomask show no signs of Al , thus this option is eliminated. It is observed that previous processes affect nanomasking and preconditioning is crucial to obtain reproducible results. Best nanomask generation is achieved when the chamber is conditioned with an 10 min Silicon Grass process. Therefore, it is concluded that the deposited FC-film at the chamber walls influences the process. Sputtered C_x and/ or C_xF_y are assumed to participate in the deposition process, albeit the exact mechanism remains unknown.

3.4.4 Masking

It is found that the geometry and the material of the applied mask have an influence on the nanomask formation and Silicon Grass generation. A low silicon load increases the etch rate, since F radicals are abundant during etching. Consequently, if dark-field masks with high-area coverage (small etching area) are applied, the etching-passivation equilibrium shifts towards etching and nanomasking is affected. For low-area etching, the OES timing method of using the $F(703.8nm)$ emission line is affected, because the shift is less pronounced compared to etching with a high Si load.

If the same process parameters are applied as if processing an unmasked wafer, the nanomasking sets in several cycles late in the process, indicating the shift toward etching. Optimizing the Silicon Grass process for every mask configuration is therefore recommended.

Another effect, which is observed when processing Silicon Grass on SiO_2 masked substrates, is the dead range of Silicon Grass in the vicinity of the mask edge or in small trenches ($< 5 \mu m$), which is also observed for Silicon Grass from RIE processes [ORP90]. The phenomenon is attributed to ion scattering at the flank of mask and trench, whereas the maximum distance s from the bottom of the trench for which scattered ions bombard the Si surface at off-normal incidence is roughly given by

$$s \sim z \tan(\beta) \quad (3.10)$$

with z representing the depth of the trench and β the maximum scattering angle for which the ion number density is still significant. It is this effect which is also assumed to be responsible for the decrease of structure density during the Silicon Grass process described in Section 4.1.2. Figure 3.35 a) shows the dead range of Silicon Grass at the edge of a mask (Fotoreisist AZ 9260, MicroChemicals GmbH).

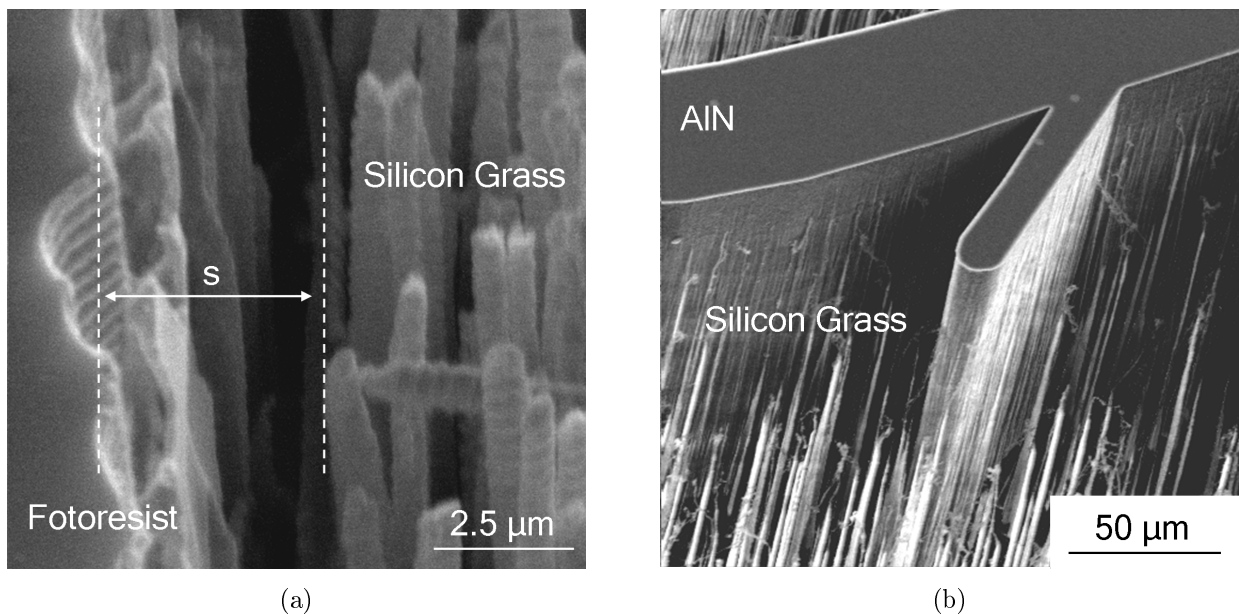


Figure 3.35: SEM images of Silicon Grass substrates masked by a) Fotoreisist and b) AlN

Furthermore, as the aspect ratio of the structures increases during processing, the radical transport towards the bottom of the trenches is affected (KNUDSEN transport model [CW89]). Usually the effect is stronger at higher process pressures, where the mean free path of the radicals is reduced. It is observed for the c-DRIE processes utilized, that etching is more influenced than passivation and consequently the etching-passivation equilibrium shifts towards passivation as the trenches get deeper. That is why Silicon Grass formation is often observed to be induced after the trench has reached a certain depth.

Another important factor is the mask material. Especially for metal-containing masks, such as *Al*, aluminium nitride (*AlN*) or *Au*, Silicon Grass formation is found to be greatly enhanced. In these cases re-adsorbed, sputtered mask material is an additional source for nanomasking. Consequently, the geometry of the structures is different and the mask geometry also plays a role. Silicon Grass density is observed to greatly vary across wider etching areas ($> 1\text{ mm}$), and the homogeneity of the features is poor. Figure 3.35 b) shows an example for Silicon Grass generated by sputtered material from an *AlN* mask.

4 Silicon Grass Processing

Silicon Grass is produced by etching the *Si* surface carrying a self-generated nanomask, which is covered in the previous chapter. Depending on the process parameters applied, the resulting profiles and sidewall morphology of the Silicon Grass are affected. Therefore, in this chapter, the whole process of Silicon Grass formation is investigated and a selection of parametrical influences on characteristic features (e.g. on structure height, density and profile) are studied (Section 4.1). This investigation will also show the interrelation of nanomasking and subsequent structure development. The main goal is to enable a profile control by variation of process parameters to manufacture specific Silicon Grass geometries, which was shown for *Cl* based RIE processes [KSM02]. The structures can also be metallized by PVD or electroless plating. A number of experiments with these processes are performed; they are covered in Section 4.2. Finally, the chapter discusses two exemplary applications: mechanical bonding and IR applications, and it is shown that an adaption of Silicon Grass to specific applications is feasible (Section 4.3).

4.1 Silicon Grass Formation

In Section 3.3.1 it is described that the working point usually shifts toward etching as the substrate is heated, due to exothermic reactions of fluorine radicals and ion bombardment. Consequently, the process shifts from the nanomasking phase into the etching phase, in which the geometries are transferred into the bulk *Si*. This transition is sketched in Figure 3.14. Depending on the working point progression during the whole process, different geometries are produced. This is illustrated in Figure 4.1.

If the process parameters are kept constant, the process starts within the region of nanomasking and shortly shifts toward etching as the surface temperature rises. Depending on the actual setting, the resulting nanomask exhibits different densities and area coverage, which in turn influence the etching in the later process. When structure density becomes high and the features appear more like a porous *Si* surface instead of individual needle shape structures, ARDE effects limit the etch rate at the bottom of the trenches and the etching-passivating balance is shifted back to passivating. Figure 4.1 shows three examples of working point progressions resulting in different Silicon Grass.

The etching behavior of c-DRIE is known from literature and various structure profiles can be realized

by process control. However, in general, c-DRIE with masked substrates is characterized by negatively tapered profiles - the result of stronger etching with deeper trenches that prevent nanomasking at the bottom and spawn Silicon Grass. Hence, to prevent the disintegration of the generated features by lateral etching or undercutting, the process must not exceed a certain lateral etch rate and the features must be protected by a sufficient sidewall passivation. Effective Silicon Grass etching therefore has different requirements compared to the standard c-DRIE trench etching. The influence of different process parameters on the resulting geometries is discussed in Section 4.3.

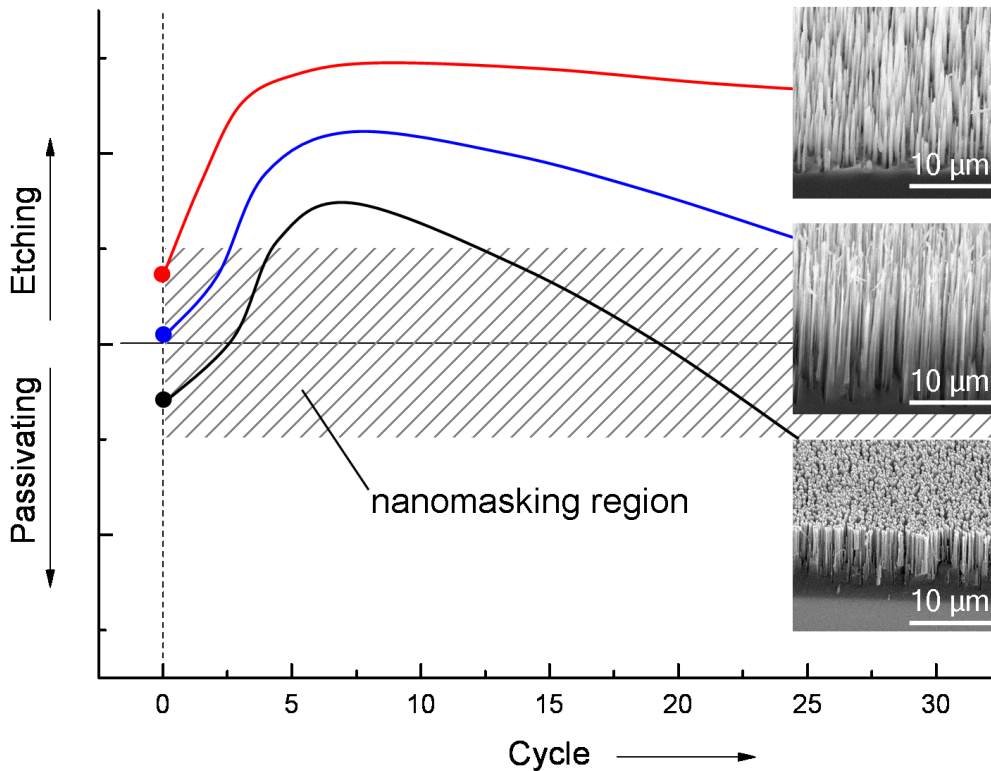


Figure 4.1: Sketch of working point progressions resulting in different Silicon Grass geometries.

4.1.1 Experimental Set-up and Structure Characterization

For the analysis, the Silicon Grass is generated with the ICP-multiplex system described on double-side polished (100) *Si* wafers with a thickness of $525 \pm 25 \mu\text{m}$, a diameter of 100 mm and a resistivity of $1\text{--}5 \Omega\text{ cm}$. The applied process parameters for the Standard Silicon Grass generation process are given in Table 3.1. After processing, the wafers are fragmented and inspected by SEM. Mean height \bar{h} and density D of the structures are analyzed by digital image processing methods of SEM pictures (Image Pro Plus®, Media Cybernetics). The density measurements are performed at three different wafer positions (*Center*, $R = 20 \text{ mm}$, $R = 40 \text{ mm}$) similar to the measurement already described for the nanomask in Section 3.3.5. By averaging several structure heights at a length of $25 \mu\text{m}$ at the wafer positions described, the mean height of the structures is acquired.

To further characterize the Silicon Grass it is helpful to introduce a Silicon Grass Aspect Ratio AR , which is calculated using the mean distance \bar{x} and the mean Silicon Grass height \bar{h} as given in the following Equation 4.1:

$$AR(t) = \frac{\bar{h}(t)}{\bar{x}(t)} \quad (4.1)$$

with:

$$\bar{h}(t) = \frac{1}{n} \sum_n h_n(t) \quad (4.2)$$

Mean Distance

Assuming a lateral hexagonal close-packed arrangement of the structures, the mean distance \bar{x} can be approximated from the measured density D .

In a hexagonal close-packed structure, the vertices, which represent the structures, are connected in the form of equilateral triangles. Each triangle has an area of:

$$A_t = \frac{\sqrt{3}}{4} a^2 \quad (4.3)$$

with a as the side length of the triangle, which approximates the mean distance \bar{x} of the structures. The area which is assigned to each structure is:

$$A_{cp} = 6 \cdot \frac{1}{3} \cdot A_t \quad (4.4)$$

Since A_{cp} can be expressed as D^{-1} it is substituted and solved for \bar{x} :

$$\bar{x} \approx \sqrt{\frac{2}{\sqrt{3}D}} \approx \frac{1.075}{\sqrt{D}} \approx \frac{1}{\sqrt{D}} \quad (4.5)$$

So finally:

$$\bar{x}(t) = \frac{1}{n} \sum_n x_n(t) \approx \frac{1}{\sqrt{D}} \quad (4.6)$$

Surface Enlargement

Another important aspect of the Silicon Grass is its inherent characteristic of an increase in surface area. It can be mathematically expressed by a surface enlargement factor e , which is approximated by making some simplifying assumptions: Assuming an array of identical, cone-shaped structures, where the mean cone height h is much larger than the base radius r_B , it follows:

$$e = \frac{A}{A_0} \quad (4.7)$$

with A_0 being the original surface area, neglecting the initial roughness. The generated surface area A is therefore:

$$A = A_0 - D A_0 r_B^2 \pi + D A_0 r_B \pi s_c \quad (4.8)$$

with s_c being the directrix of the cone. Since $h \gg r_B$ it is substituted h for s_c in 4.8 and insert this in 4.7 to find:

$$e = 1 - D r_B \pi (r_B - h) \quad (4.9)$$

Finally, the expression $(r_B - h)$ is simplified to $-h$ which results in:

$$e = 1 + D r_B \pi h \quad (4.10)$$

However, in Equation 4.10 the sidewall scalloping, which can significantly increase the surface area, is not considered. To approximate the influence of scalloping, the lateral area of a standard cylinder A_{cyl} is compared with that of a cylinder with a sinusoidal profile function $A_{cyl,sin}$. The lateral area of the body is found by revolving the sine function

$$f(x) = z_{scal} \sin\left(\frac{2\pi}{p_{scal}}x\right) + \bar{r} \quad (4.11)$$

about the x-axis. Here, the amplitude is the mean scalloping depth z_{scal} , \bar{r} the mean radius of the structure and p_{scal} the mean period of the scallops. The lateral area of a rotational body with a surface profile function $f(x)$ is given by:

$$A_{lat} = 2\pi \int_{x_0}^x f(x) \sqrt{1 + f'(x)^2} dx \quad (4.12)$$

Inserting Equation 4.11 gives:

$$A_{cyl,sin} = 2\pi \int_0^{p_{scal}} \left(z_{scal} \sin\left(\frac{2\pi}{p_{scal}}x\right) + \bar{r} \right) \sqrt{1 + \left(\frac{2\pi}{p_{scal}}z_{scal} \cos\left(\frac{2\pi}{p_{scal}}x\right)\right)^2} dx \quad (4.13)$$

Solving Equation 4.13 numerically with typical values for $z_{scal} = 200 \text{ nm}$, $b = 250 \text{ nm}$ and $c = 250 \text{ nm}$ gives $A_{cyl,sin} \approx 1.9 * 10^6 \text{ nm}^2$, which is about 4.8 times the area of the normal cylinder A_{cyl} . This shows that scalloping can play a significant role in further enlarging the surface area in Silicon Grass etching. So to arrive at the final formula for the surface area enlargement, Equation 4.10 is multiplied by the additional surface area enlargement due to scalloping

$$e_s = \frac{A_{cyl,sin}}{A_{cyl}} \quad (4.14)$$

to obtain

$$e = e_s(1 + D r_B \pi h) \quad (4.15)$$

Calculating the surface enlargement for the Standard Silicon Grass with $e_s = 4.8$, $D = 1 \mu\text{m}^{-2}$, $r_B = 250 \text{ nm}$ and $h = 15 \mu\text{m}$ results in a value of about $e \approx 60$.

Differential Etch Rate

Furthermore, when analyzing the etching of Silicon Grass, the differential etch rate $R_{etch,dif}$ between the tips and trenches must be considered:

$$R_{etch,dif}(t) = R_{etch,tr}(t) - R_{etch,ti}(t) = \frac{d}{dt}z_{tr}(t) - \frac{d}{dt}z_{ti}(t) = \frac{d}{dt}h(t) \quad (4.16)$$

Here, $R_{etch,tr}$ and $R_{etch,ti}$ label the etch rate of the trenches and the tips, respectively. In the ideal case, the etching of the tips should be completely prevented by passivation. An illustration is given in Figure 4.2. In fact, it is the differential etch rate $R_{etch,dif}$, that defines the Silicon Grass progression. It is observed that $R_{etch,tr}$ and $R_{etch,ti}$ can cancel each other out if the working point is too far away from the etching-passivation equilibrium.

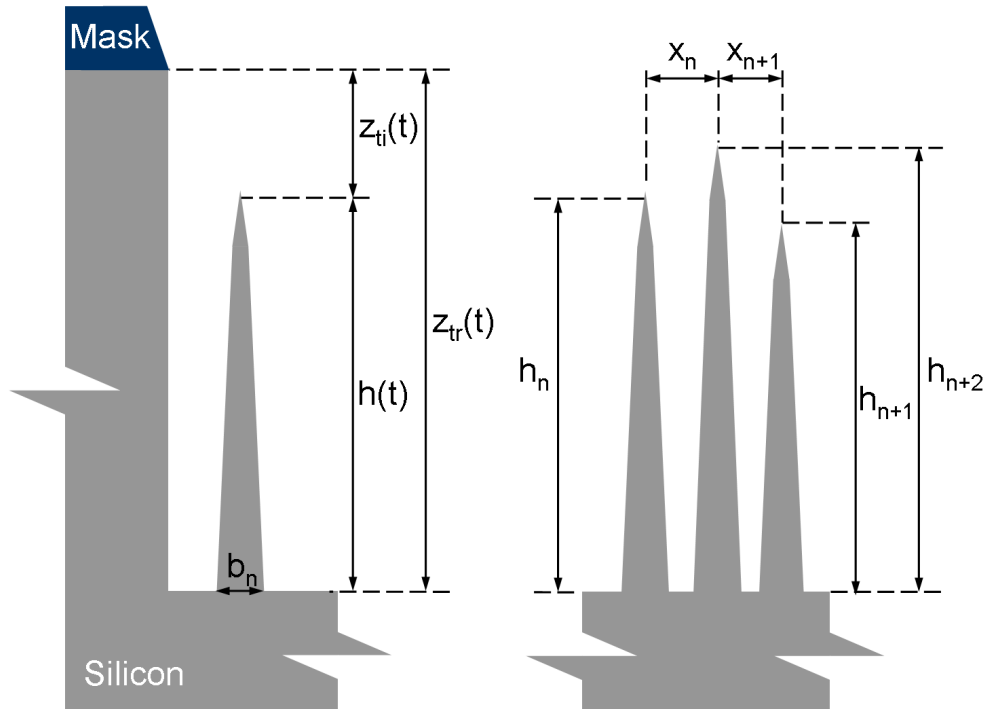


Figure 4.2: Sketch of Silicon Grass property measurements.

4.1.2 Structure Development

In the following the structural development during the standard Silicon Grass process is discussed. Geometric properties like structure height, density and profile undergo several changes that must be considered for a successful adaptation of the features.

Figure 4.3 shows the development of structure height h and density D during the Standard Silicon Grass process at different radial wafer positions (*Centre*, $R = 20\text{ mm}$, $R = 40\text{ mm}$). The standard deviation, given by the error bars, shows the observed variation at each wafer position. It is observed for all Silicon Grass types and caused by the distribution of cluster diameters of the nanomask.

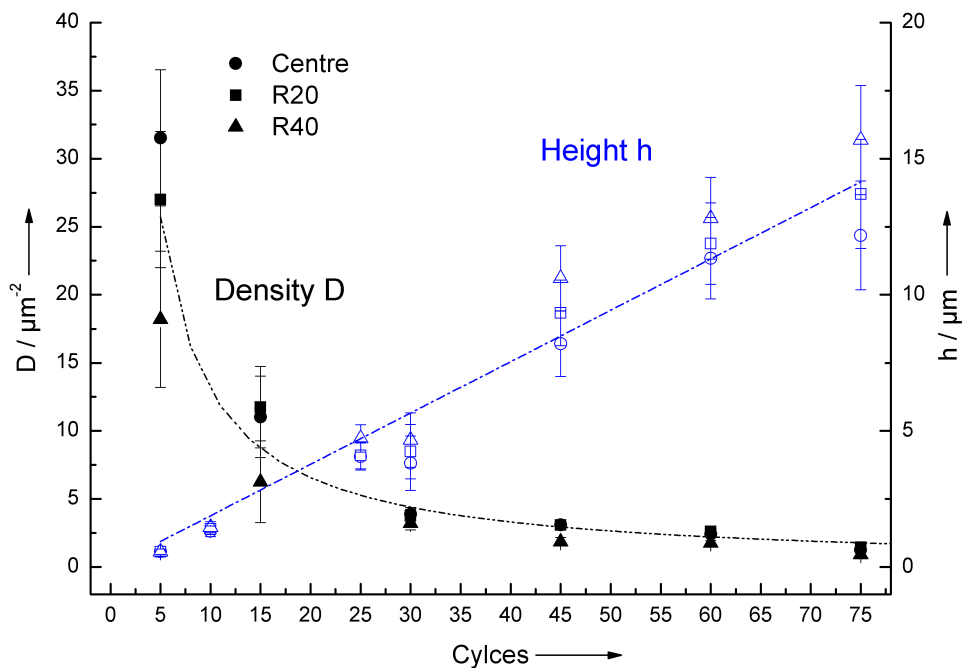


Figure 4.3: Progression of Silicon Grass height h and density D throughout the process.

After the initial nanomasking taking place in the first cycles, structures with measurable heights begin to form. The curve progression of structure height can be described as roughly linear, although it must be noted that the differential etch rate $R_{etch,dif}$ is not constant throughout the process. It takes approximately three to five cycles for the transition from nanomasking to structure etching, which causes $R_{etch,dif}$ to increase during these cycles.

Saturation of structure height at about $30\ \mu\text{m}$ is observed for processes with more than 300 cycles. ARDE effects limit the progression of the Silicon Grass as it becomes very dense at its base point where $R_{etch,dif}$ drops to zero. Silicon Grass from the standard process of 75 cycles reaches a height of about $12 - 15\ \mu\text{m}$, whereas the height of the structures varies with their radial position, with the structures at the $R40$ position being higher than those at the *Centre*. This inhomogeneity is explained by loading of the ICP-multiplex (see Figure 2.7).

Structure density D drops rapidly within the first 30 cycles and levels off at a value of about $1 - 2 \mu\text{m}^{-2}$ after 75 cycles. The curve can be fitted with an allometric function. D is also found to vary with radial wafer position, whereby the Silicon Grass is generally denser in the center of the wafer. This indicates a correlation between h and D and $R_{etch,dif}$. Thinner structures are likely to be removed by lateral etching during the process. Ion bowing and scattering play a significant role, as the passivated tips become negatively charged and deflect the ions toward the sidewalls, where they cause lateral etching. Those ions which are not consumed are scattered and hit the flanks of neighboring features, also causing lateral etching. It is this undercutting is made responsible for the decrease and leveling of the density curve progression for the given parameter setting. Ion scattering has already been described in Section 3.4.4 where it is also responsible for the dead range of Silicon Grass at the edge of a mask. Hence, Silicon Grass height h and density D are related and cannot be controlled independently from one another as long as lateral etching by bowing and scattering is prevalent.

It is noted that these findings strongly depend on the used equipment and the applied process parameters, which are held constant throughout the process. In order to generate a wide range of Silicon Grass geometries it would be useful to split the process into two separate ones: an initial process to setup the nanomask and an etching process to structure the Silicon Grass.

4.1.3 Parametrical Influences

Deposition Step Time

Since deposition step time τ_{dep} is determined to have a great impact on the density of the nanomask in Section 3.3.5, influence of this parameter on the resulting Silicon Grass geometries is expected. This is shown in [AA08], where the dependence of h and profile on τ_{dep} is investigated.

The deposition step time τ_{dep} also determines the thickness of the FC-film on the sidewalls and affects lateral etching which an important limiting factor in terms of Silicon Grass density. Furthermore, it leads to an increased build-up of polymer at the tips of the structures, which, if it becomes very voluminous, will again affect etching by deflecting and scattering incoming ions.

Figure 4.4 depicts the influence of deposition step time τ_{dep} on the Silicon Grass density D and height h . In contrast to [AS08] where the etch step time τ_{etch} is fixed, it is calculated according to Equation 3.6. A clear trend for both parameters is present. While density D drops from about $4.1 \mu\text{m}^{-2}$ to $0.8 \mu\text{m}^{-2}$, height h increases from $8 \mu\text{m}$ to about $14 \mu\text{m}$ as deposition step time increases. The resulting structures are shown in Figure 4.5. The greater density and thinner structures observed for $\tau_{dep} = 7 \text{ s}$ (see Figure 4.5 a)) are explained by the finer grained nanomasking and stronger lateral etching as compared to the other examples. It is also noted that no polymer agglomeration is observed on the needle tips, which would protect them from being etched; thus the structures are shorter. In contrast to this, the structures for $\tau_{dep} = 15 \text{ s}$ (see Figure 4.5 c)) are coarser than the rest. Polymer agglomerates are found for $\tau_{dep} = 11 \text{ s}$ and 15 s which explains the equal height for both structures.

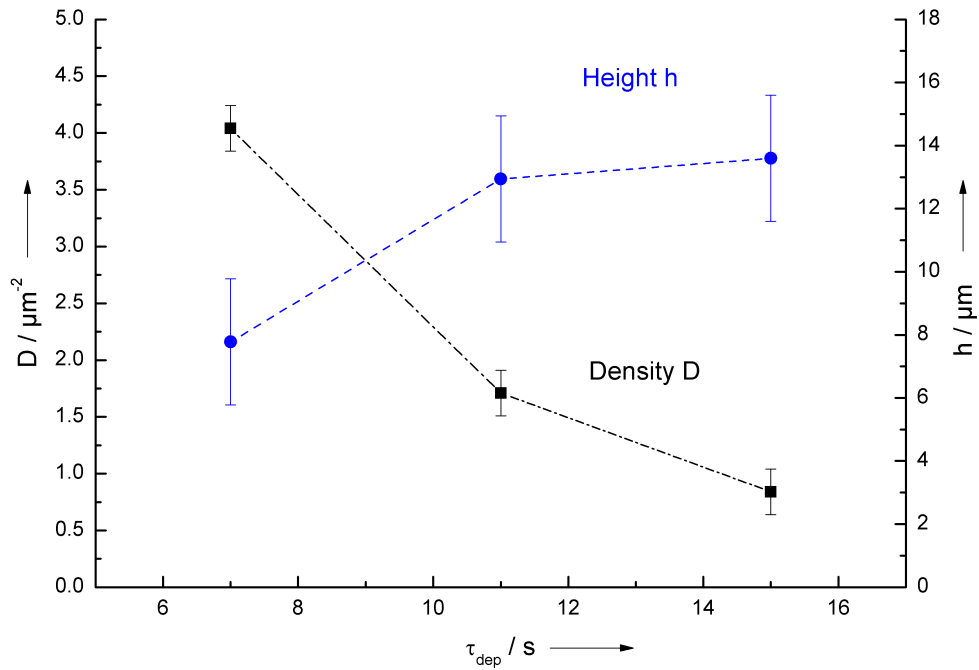


Figure 4.4: Influence of the deposition step time τ_{dep} on Silicon Grass height h and density D .

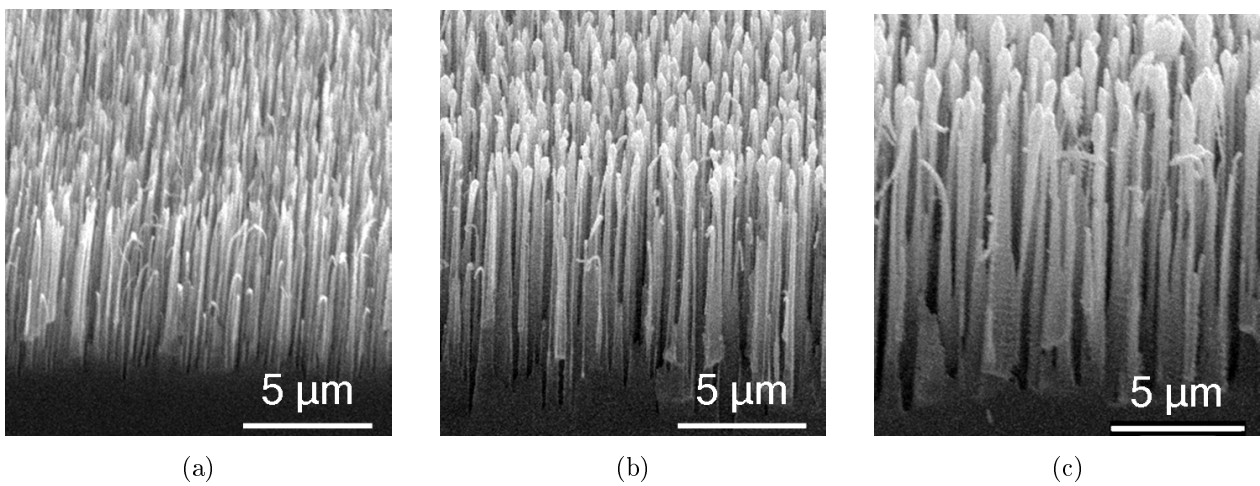


Figure 4.5: Different Silicon Grass with τ_{dep}/τ_{etch} a) 7 s/6 s, b) 11 s/9 s and c) 15 s/12 s.

Bias Power

To study the effect of bias power P_b on Silicon Grass properties, it is varied from 8 to 21 W. All other parameters are kept constant, according to the Silicon Grass Process. The etch step time is not altered, but left at 9 s for every run. Due to the increased etching rate at higher bias power values ($P_b = 15, 17, 19$ and 21 W), nanomasking is affected and sets in several cycles later in the processes. Figure 4.6 shows the influence of bias power P_b on density D and height h . It is observed that, while D is reduced by approximately half of its value from 1.8 to about $0.9 \mu\text{m}^{-2}$, h varies from about 11.8 to $14.8 \mu\text{m}$. In contrast to D , where the change occurs steadily with higher bias powers, the maximum height is reached for $P_b = 19$ W. In this regard, it is observed that at higher bias powers (19 and 21 W) two types of needles develop: some are regularly shaped and others are larger and thicker, see Figure 4.7. Their occurrence is explained by additional masking by carbon dust and film flaking (covered in Section 3.4.1). Because these larger and thicker needles are spawned by another mechanism, they are not accounted for in the height measurement. No Silicon Grass formation is observed at 8 W. Instead, a thin FC-film is found on the surface, which shows that no Silicon Grass could be formed due to insufficient etching of the FC-film.

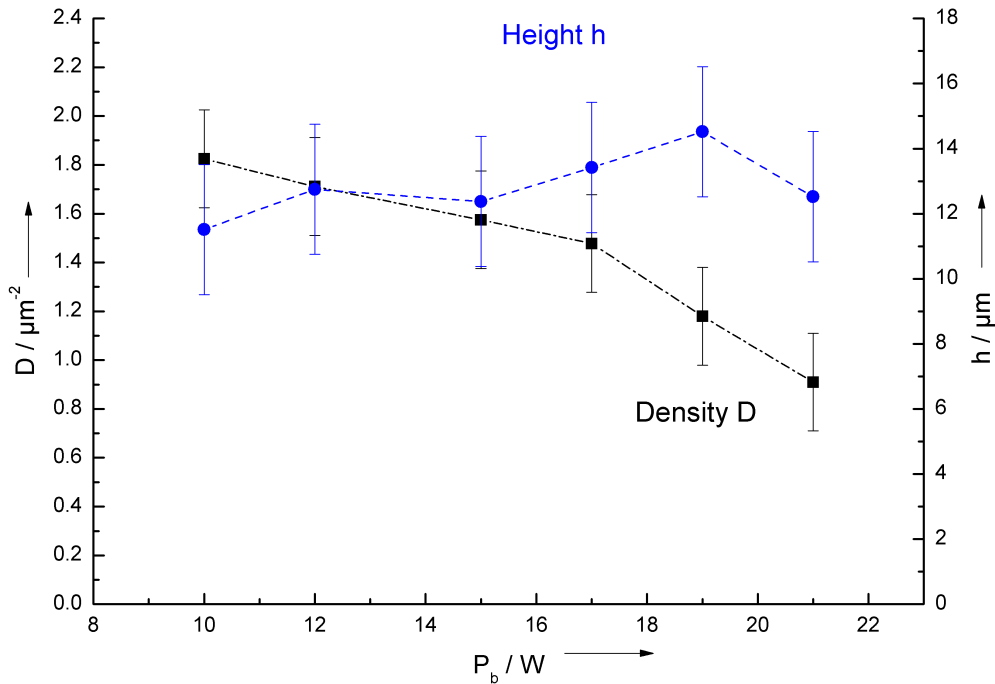


Figure 4.6: Influence of bias power P_b on Silicon Grass height h and density D .

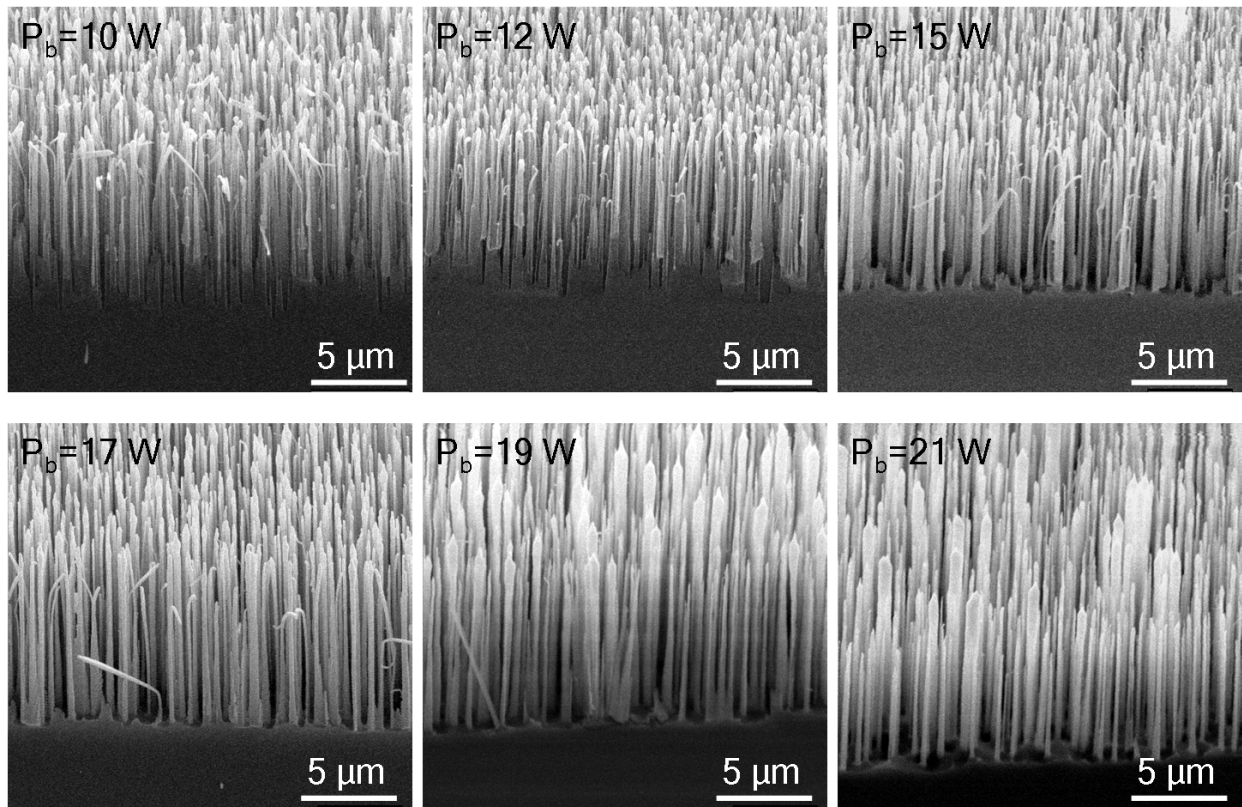


Figure 4.7: Different Silicon Grass types from processes with different values for P_b .

From Figure 4.7 additional conclusions are drawn. As discussed, ion bowing influences the etching when the FC-agglomerates and the sidewall passivation film are charged by incident angular electrons at the upper part of the structures. The charge deflects incoming ions toward the sidewalls and leads to physical lateral etching (bottling and scattering). By increasing ion velocities, ion deflection is altered and the point of impact shifts from the upper and middle part toward the base of the needles. When physical etching at the base becomes stronger, thinner structures are cut off or etched away, explaining the decrease in density D . At lower bias powers, physical etching occurs at the upper and middle part, causing needles with small diameters which will eventually bend under their load (see Figure 4.7 for $P_b = 10, 12,$ and $15 W$). The effect is also demonstrated by the bent structure at $P_b = 17 W$, where etching has caused a near cut-off close to the base. Also affected by this shift are the scallops, which are more pronounced for higher bias powers, where physical lateral etching is reduced, see Figure 4.8.

The geometrical shape of the needles is an important characteristic (e.g. for Silicon Grass with index matching properties, high mechanical stability or high surface enlargement) and can be affected by bias power. At high ion velocities, better etching anisotropy leads to cylindrically-shaped needles with pronounced scallops standing on a flat ground plane. Lower values lead to a gradual change between smooth structures and the bulk.

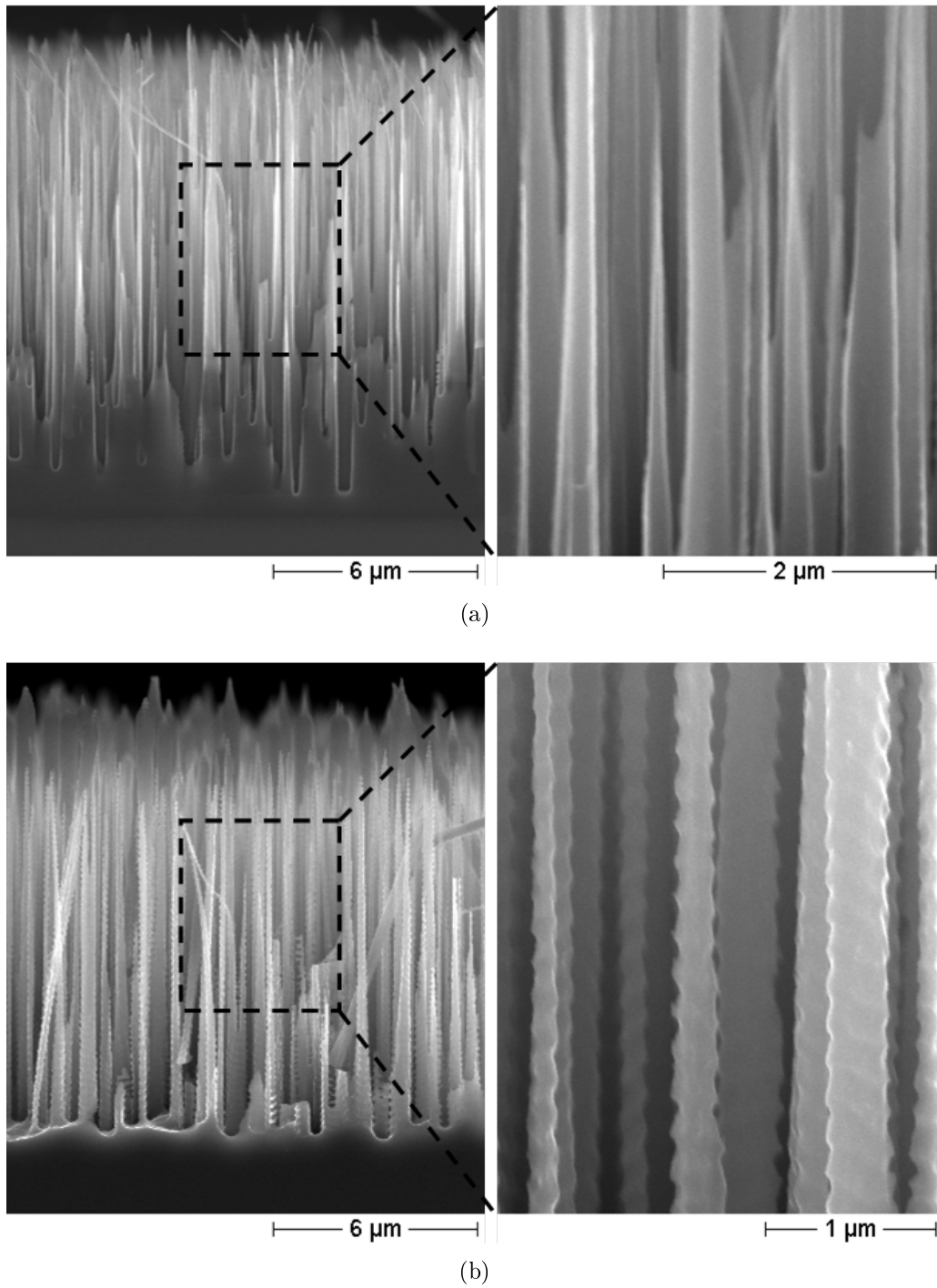


Figure 4.8: Effect on sidewall scallops by a variation of physical lateral etching at a) $P_b = 12 W$ and b) $19 W$.

4.2 Metallization of Silicon Grass

In various applications metallized surfaces play an important role, as they provide the conditions for chemical reactions (e.g. in microreactors), enable electrical functionality or constitute modifiable sensor surfaces (e.g. for bio-sensors). Here, Silicon Grass presents great potential for silicon-based devices, where a high surface enlargement leads to an enhanced performance of the device. For this reason, different metallization techniques for Silicon Grass investigated in [Kie09] are discussed in this section. The high aspect-ratio of the Silicon Grass poses challenges for PVD metallization methods so that enhanced methods (e.g. ionized PVD or oblique angle deposition) are suggested. Electroless plating provides a cost-effective way to cover the Silicon Grass at a high deposition rate, compared to the PVD methods. However, the electroless plating techniques generate a rather thick and coarse-grained layer and require special pre-treatment procedures and therefore must be checked for technological compatibility.

4.2.1 Physical Vapour Deposition

Evaporation and sputtering are metallization techniques commonly used in semiconductor fabrication. In the context of this work, where a homogeneous coverage of the three dimensional structures is desired, sputtering is preferred. It is advantageous compared to evaporation, since the deposition process has a less pronounced directional characteristic and the deposited film usually exhibits a better edge coverage, greater conformity and purity.

For the experiments the Silicon Grass is metallized with a commercially available PVD system (LS 250 EF, Ardenne). *Al*, *Au* and *Ti* are sputtered with different parameter settings (see Table 4.1). *Ti* is used to provide a good adhesion of the *Au* that is sputtered subsequently. The resulting equivalent film thicknesses t_{equ} are measured *in-situ* by the system.

Table 4.1: Sputter parameters for *Al* and *Au* of the LS 250 EF system.

Parameter	<i>Al</i>	<i>Au</i>	<i>Ti</i>
P (W)	160	100	160
p (Pa)	0.3	0.3	0.3
Q_{Ar} (sccm)	30	30	30
t_{equ} (nm)	200/500	200/500	20

Examining the surfaces by SEM (Figure 4.9 and Figure 4.10) shows that Silicon Grass is not covered uniformly. For both metallization systems, the incoming material reaches mainly the upper part of the structures. This agglomeration can be especially observed for the 500 nm equivalent film thickness. Because of shadowing, only a small fraction of sputtered material reaches the bottom of the Silicon Grass. This effect becomes even stronger as more and more material is concentrated at the tips. In

Figure 4.9 b) bending of the structures is noticed, indicating a stress induced by the *Al* coverage.

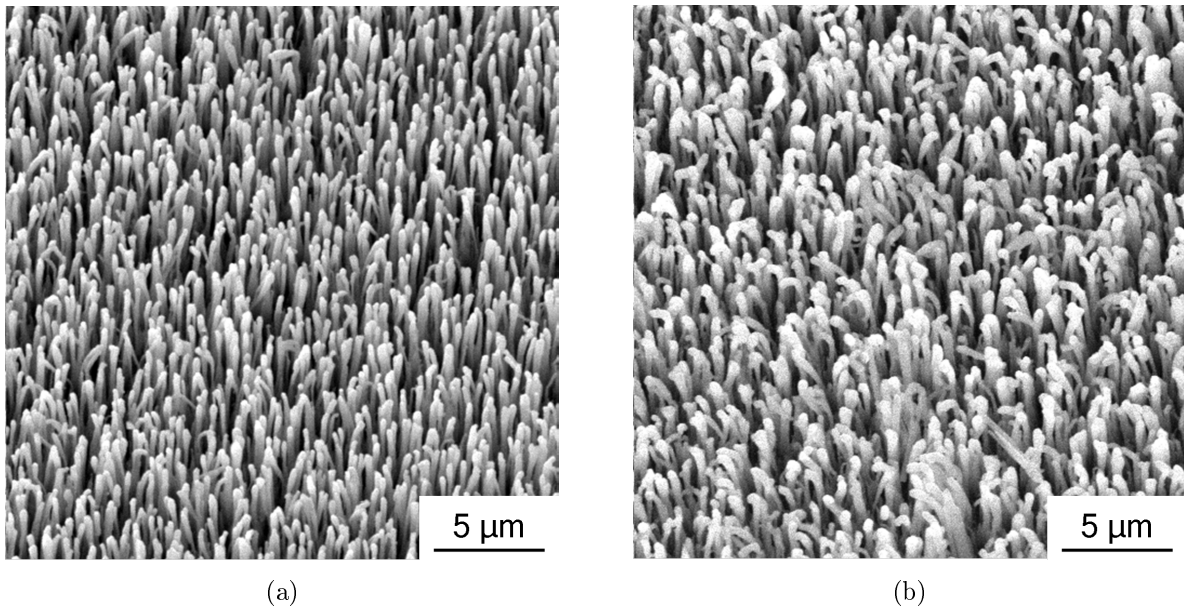


Figure 4.9: Sputtered *Al* on Silicon Grass. a) $t_{equ} = 200 \text{ nm}$ and b) 500 nm .

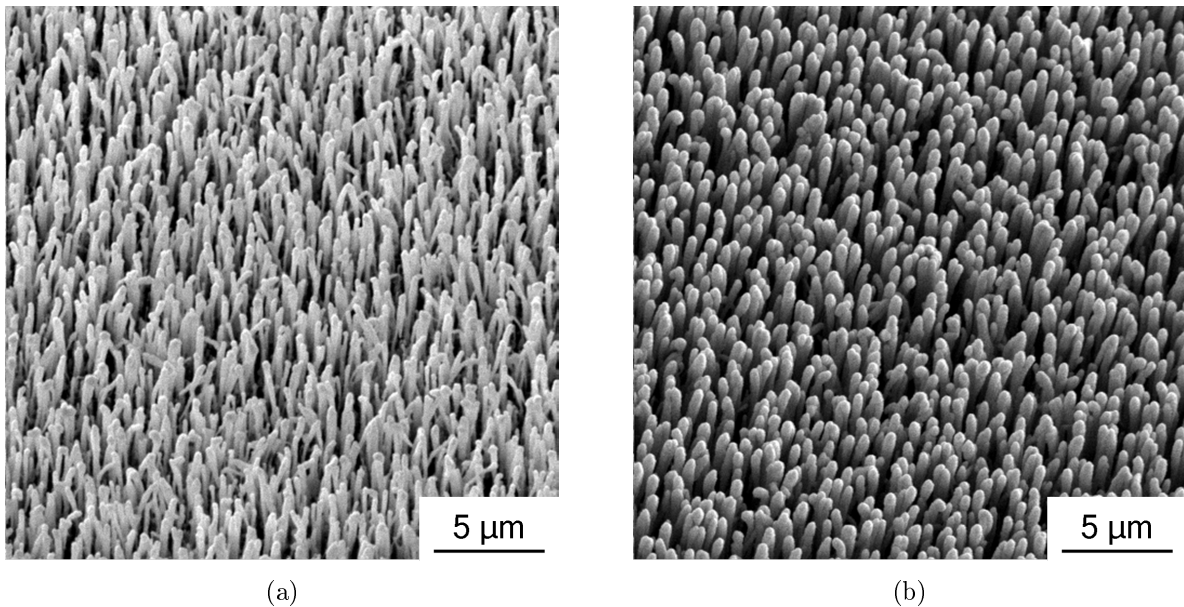


Figure 4.10: Sputtered *Ti/Au* on Silicon Grass. a) $t_{equ} = 20/200 \text{ nm}$ b) $20/500 \text{ nm}$.

To analyze whether small amounts of the metal are reaching lower parts of the needle, a Transmission Electron Microscopy (TEM) study is performed. Here, some metallized Silicon Grass was scratched off with a scalpel and prepared on a thin carbon lattice. The results for 200 nm *Al* and *Au* are given in

Figure 4.11 and Figure 4.12, respectively. For both structures the scan starts at the tip and progresses toward the base as indicated by the red line in the figures.

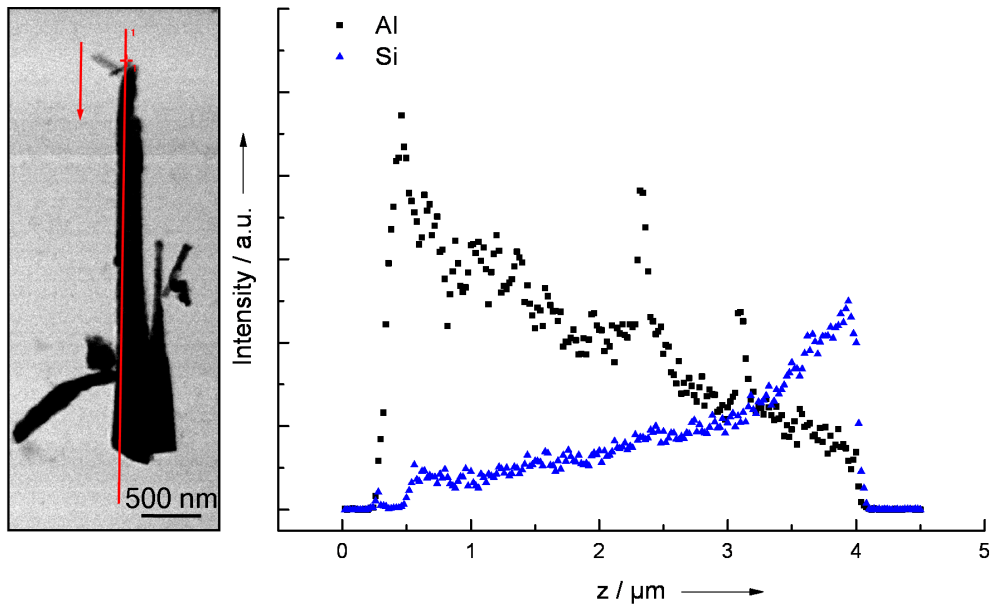


Figure 4.11: TEM analysis on Silicon Grass needle with 200 *nm* sputtered *Al*.

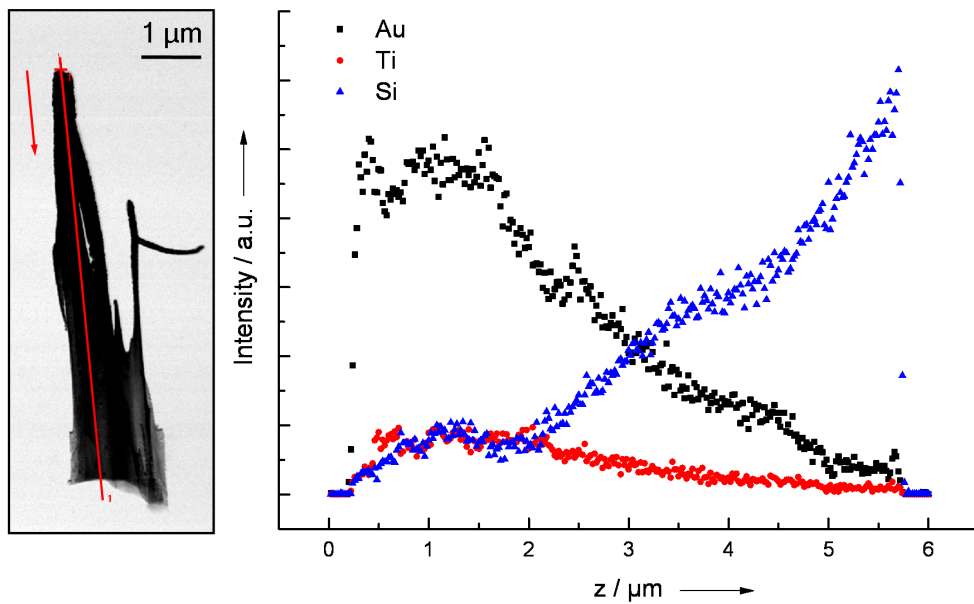


Figure 4.12: TEM analysis on Silicon Grass needle with 200 *nm* sputtered *Au*.

The images show that the Silicon Grass geometry is complex and can roughly be described as needle-like. Because of the gradual transition from the structures to the bulk, the features are not sheared off

at their bases, rather the upper half breaks off during the preparation with the scalpel. This is why the structures exhibit a height of only about $5\ \mu\text{m}$.

Scanning for the elemental composition from top to bottom reveals an approximately linear decrease of metal. At the lower end only a small amount of deposited metal is found. This shows that the coverage is not homogeneous. If fully metallized Silicon Grass structures by PVD are desired, enhanced techniques such as ionized PVD [Mon99] [SWK⁺97] or oblique angle deposition [KL05] [RSB98] should be considered. A good overview of possible methods for the metallization of nanostructures is given in [And07]. Alternatively, the geometry of the Silicon Grass is limited to a certain height, density and profile angle to ensure proper coverage.

Another aspect that influences the deposition process is the scalloped sidewall profile. As every scallop acts like a small protrusion, the metal material deposits primarily on these edges, shadowing the one below and as a result, the metal film becomes non-uniform, see Figure 4.13. A similar effect was observed in [JKJ⁺07], where columnar, porous structures are found at the sidewalls of trenches, which are also explained by shadowing effects.

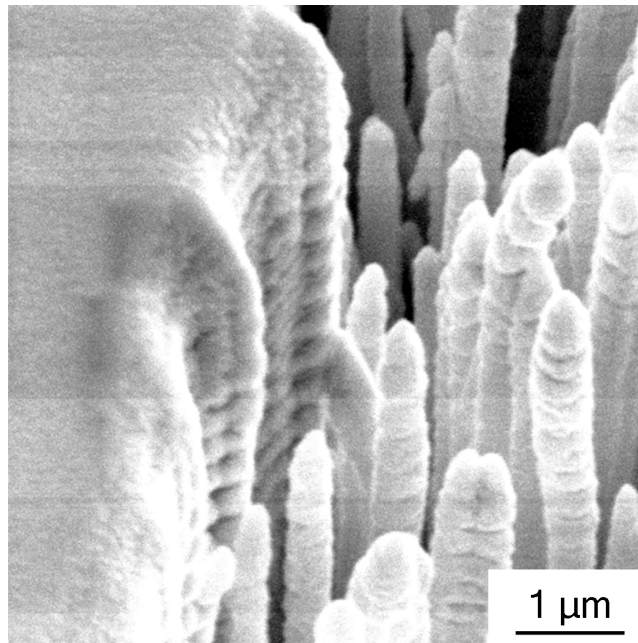


Figure 4.13: Effect of scalloping on the uniformity of a sputtered Au film. $t_{equ} = 200\ \text{nm}$.

4.2.2 Electroless plating

Electroless plating is investigated as another method to metallize the Silicon Grass. In comparison to PVD it is more cost-effective, especially when a greater metal thickness ($> 200\text{ nm}$) is desired. Due to the semi-conducting nature of the substrate, no electroplating is applied, as the large field gradient at the Silicon Grass tips would lead to a non-uniform coverage of the structures. The materials tested are *Ni*, *Cu* and *Ag*.

For *Ni* and *Cu* a special pre-treatment is performed to prepare the Silicon Grass, as given in the following procedure:

1. Acid degreasing (12 *min*)
2. Colloidal activation (5 *min*)
3. Rinse in distilled water
4. Activation by hydrogen chloride (*HCl*) (3 *min*)
5. Acceleration by *NaOH* (5 *min*)
6. Rinse in distilled water

The steps 2, 3 and 4 are repeated three times for best results. In contrast to *Ni* and *Cu*, the processing of *Ag* requires only steps 1 and 4.

After pre-treatment the surfaces are subjected to the different metallization baths. The *Ni* bath is prepared with a commercially available electrolyte (LECTRO-NIC® Series, Enthone GmbH) used at a temperature of 82°C . The *Ag* bath is prepared with silver nitrate (AgNO_3), potassium hydroxide (*KOH*), ammonia (NH_3), H_2O and glucose ($\text{C}_6\text{H}_{12}\text{O}_6$) (chemical composition given in [Kie09]). For the electroless plating with *Cu* a commercial method (Enplate Cu 872, Enthone GmbH) is used.

In contrast to *Cu*, good metallization results are achieved for *Ni* and *Ag*, see Figures 4.16, 4.14 and 4.15. After 2 *min* in the *Ni* bath, the structures show a metal coating estimated to be approximately 300 – 500 *nm* thick. The granular surface morphology observed is the result of the growth mechanism, which starts from adherent colloids on the structures. As can be seen from Figure 4.14, the colloids nearly cover the entire Silicon Grass surface, even reaching its base. While the tips are completely covered after 2 *min*, the metallization at the base is still not fully completed, showing that the film growth is faster at the top. This is also the case for electroless plating with *Ag*, where good coverage is achieved after a 10 *min* treatment, see Figure 4.15. Because no colloidal activation is needed for the *Ag* metallization, the resulting surfaces exhibit a less granular morphology.

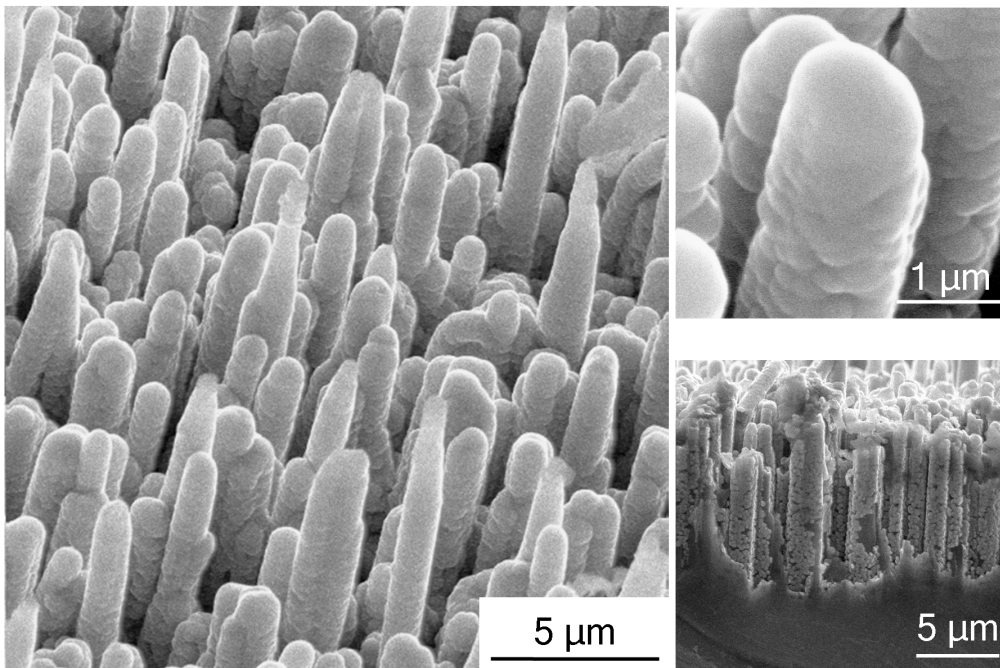


Figure 4.14: Metallized Silicon Grass by *Ni* electroless plating [Kie09].

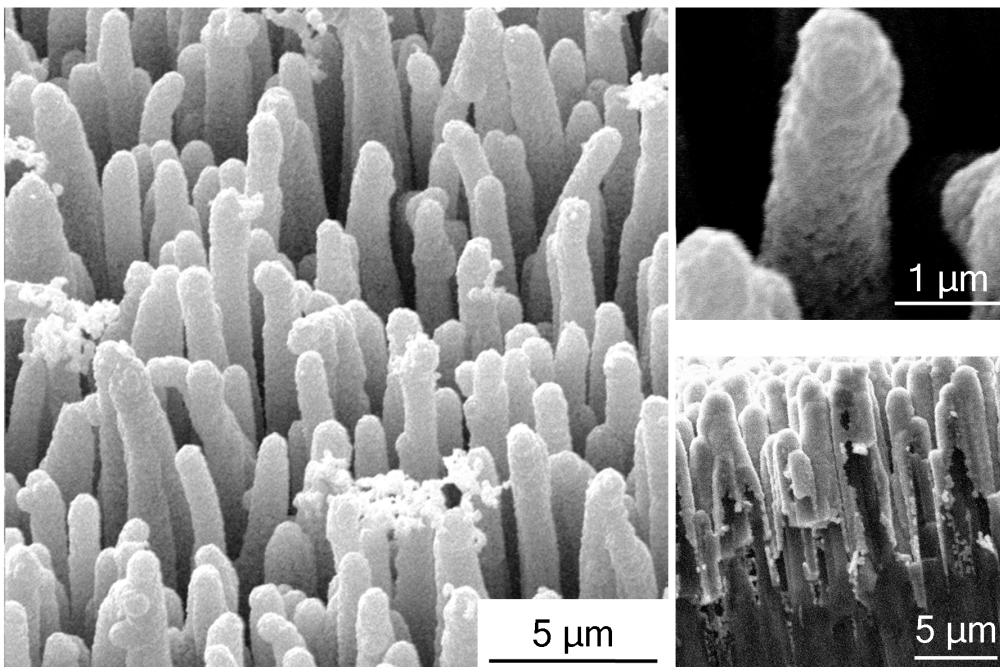


Figure 4.15: Metallized Silicon Grass by *Ag* electroless plating [Kie09].

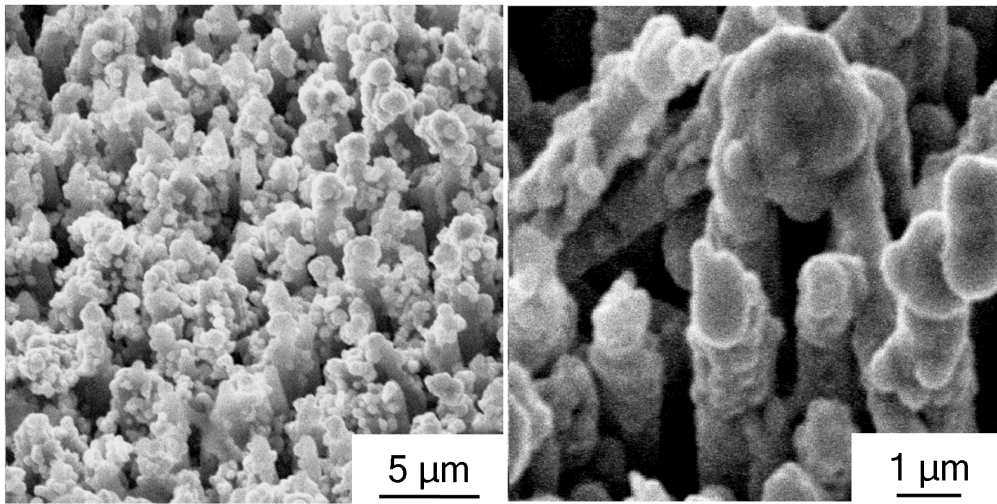


Figure 4.16: Metallized Silicon Grass by *Cu* electroless plating [Kie09].

4.3 Adapted Silicon Grass

As the previous sections of this chapter show, Silicon Grass properties can be influenced by parametrical changes and subsequent modification. Depending on the individual application, the Silicon Grass must be specifically adapted.

The following section gives examples of different Silicon Grass types used for packaging and optical applications and proves that it is possible to enhance the functionality of the Silicon Grass by choosing the appropriate geometry. In Figure 4.17 the different Silicon Grass types used in the following investigations are presented. Table 4.2 summarizes the characteristic geometrical properties.

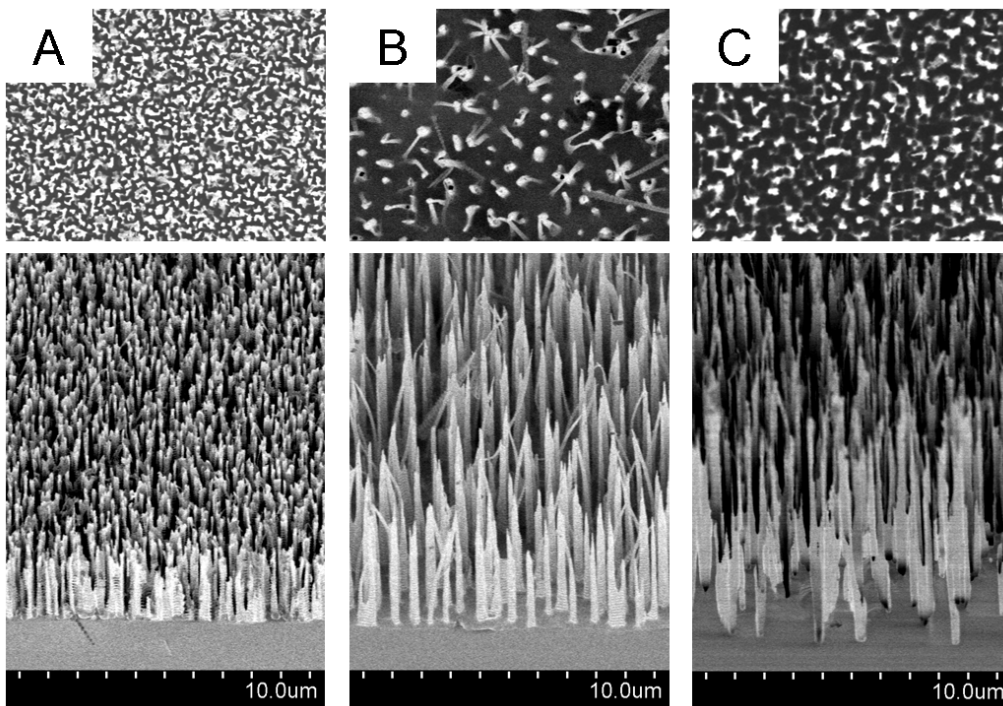


Figure 4.17: Different types of Silicon Grass.

Table 4.2: Characteristic geometrical properties of the different Silicon Grass types.

Type	Height μm	Density μm^{-2}	Mean distance nm	Sidewall profile	Structure-bulk transition
A	3.8	3.8	550	scalloped	sharp
B	5.7	1.0	1070	scalloped	sharp
C	12.4	2.1	740	smooth	gradual

4.3.1 Silicon Grass for Packaging

Silicon Grass can be used as a method of mechanical bonding between structured *Si* surfaces or to join *Si* with other materials such as polymers and ceramics (see Section 2.2.2). The method is based on a large contact area in combination with the form-fitting and interlocking of the surface structures. In order to optimize the bond and generate high retention forces, the Silicon Grass can be adapted. Given below are some important properties for good performance in this type of application:

- Large contact area
- High tensile strength of the structures
- High number of undercutting features at the structures
- Proper ratio of stiffness and flexibility of the structures

Some of the formulated requirements are contrary to one another, which indicates that an optimization is necessary. A large contact area would be generated by a high Silicon Grass density in combination with a maximized height and a strongly scalloped sidewall profile. But this will also result in very thin and flexible structures, where a scalloped sidewall profile is difficult to realize. Furthermore, the assembly by force fitting is impaired, since structures which are too flexible will not effectively penetrate each other.

Silicon - Silicon Bond

In the experiment performed, the retention forces (pull-strength) of different types of Silicon Grass in the Nano-Velcro[®] are investigated (see Figure 4.17). For the test, samples with a size of $10 \times 10 \text{ mm}^2$ are prepared. The pull test is performed with a commercial tool (Model Z050, Zwick GmbH & Co. KG). A detailed description of the procedure as well as additional investigations of the Nano-Velcro[®] are given in [Kre05] and [SFK⁺06].

The results of the pull tests are given in Figure 4.18 a) and clearly show an interdependency between the Silicon Grass geometry and the pull strength. An increase of pull strength with structure height indicates that height is an important characteristic in order to achieve high bond strengths. This is expected, since it defines the thickness of the area of interlocking features and thus the area of contact of both partners. The performance of Silicon Grass Type C can also be affected by its gradual transition from structure to bulk material which is beneficial to the stress distribution at the interface. In order to find the optimum Silicon Grass geometry for Nano-Velcro[®] applications, further testing with a wider range of different Silicon Grass types is required.

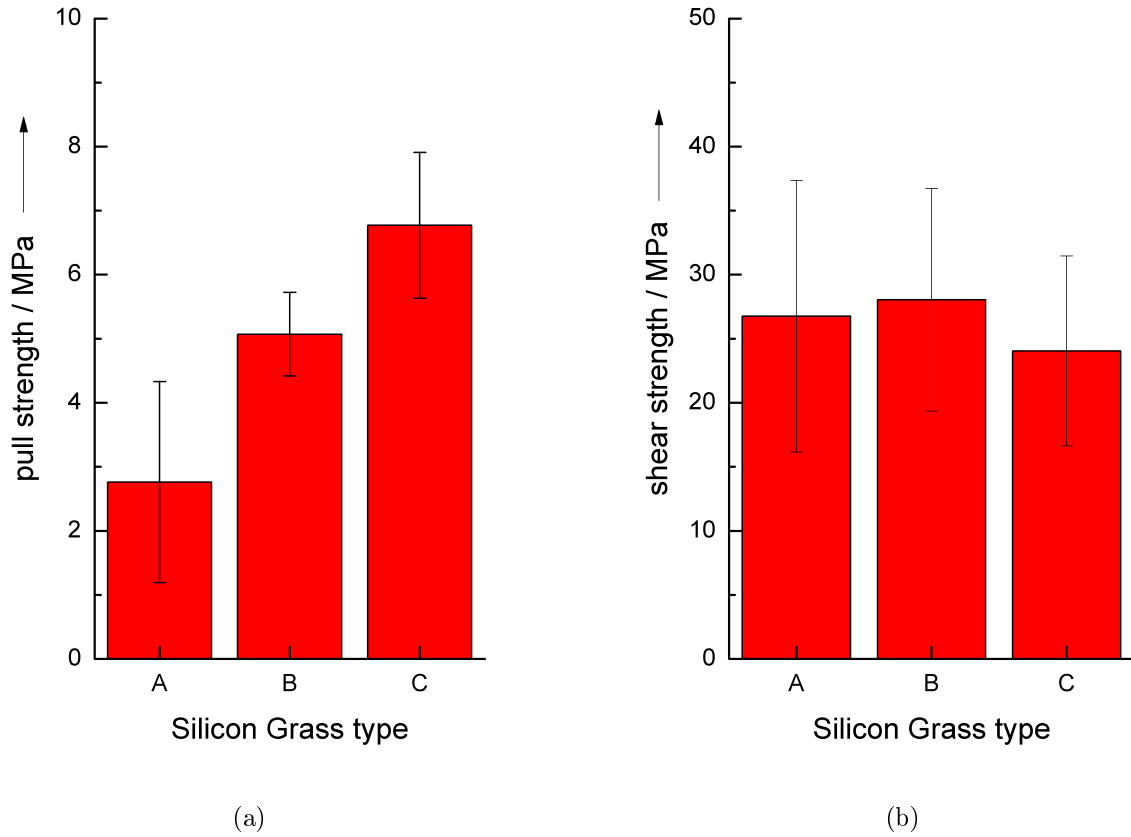


Figure 4.18: Results of the a) pull test of the Nano-Velcro[®] and b) shear test of the Silicon-Polymer bond with different types of Silicon Grass.

Silicon - Polymer Bond

In another investigation the effect of geometry on the performance of bonds between Silicon Grass and polymers is analyzed. This time, the shear strength of the bonds is examined. For this task test pylons of an epoxy-based negative resist (*SU-8 2075*, Microchem Corp.) with a diameter of $500 \mu\text{m}$ and a height of $100 \mu\text{m}$ are fabricated on the structured Silicon Grass surface. Processing of *SU-8* is optimized to ensure a complete filling of the Silicon Grass by polymer and prevent bubbles by outgassing of the polymer solvent. The created pylons are sheared off with a commercial shear tester (Model 5600 P/S, FK Delvotec) to evaluate the shear stress at the moment of failure. A detailed description of the complete investigation is given in [Mue08]. The results are shown in Figure 4.18 b).

The Silicon Grass - Polymer bonds yield a shear strength which ranges between 24 and 28 MPa and is in the order of the maximum tensile strength of the polymer material ($\sigma_{SU-8} = 60 \text{ MPa}$). This time, no clear trend can be observed but Silicon Grass type C shows a slightly reduced shear strength as compared to the other two types. The investigation of the tested samples reveals a combination of a

cohesion failure of the *SU-8* and the *Si* (see Figure 4.19). The image shows that the rupture starts inside the polymer and propagates into the *Si* after about half the diameter of the pylon. Furthermore, it is observed that it is not the Silicon Grass which is sheared off, but a chunk of *Si* is ripped out of the substrate. As *Si* has a tensile strength well above the measured values, its failure is explained by the etching damage induced during the Silicon Grass process. High energy ions cause small fissures and cracks inside the near surface material and disturb the crystal structure of the *Si* thus reducing its mechanical stability.

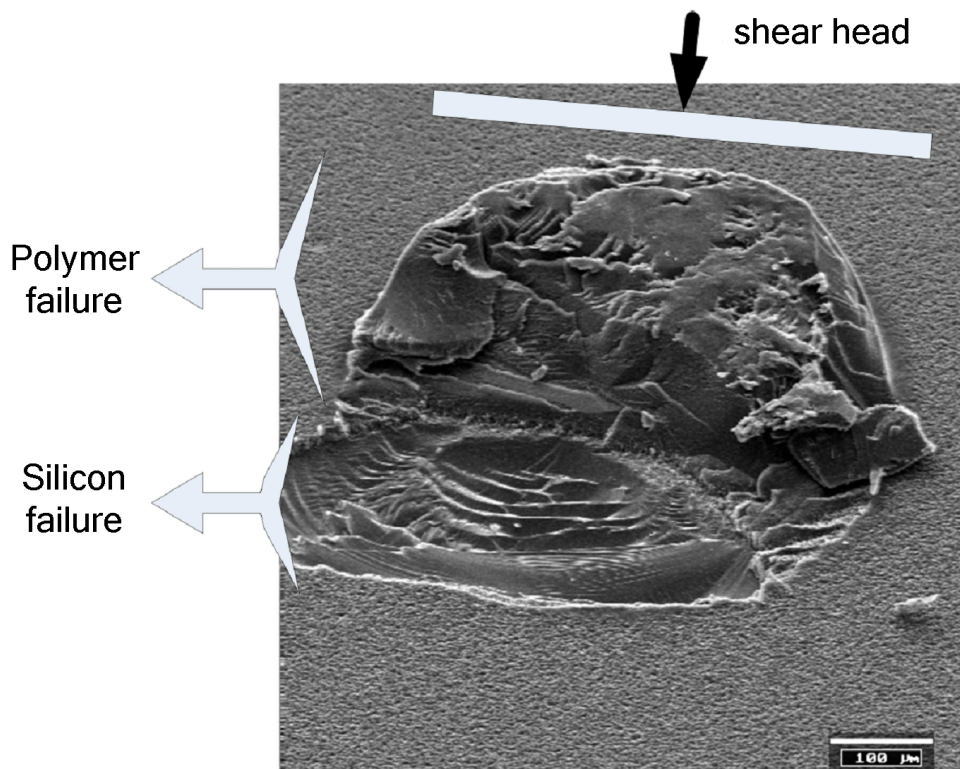


Figure 4.19: SEM image of a sheared off *SU-8* pylon.

The investigations performed show that it is possible to adapt Silicon Grass for mechanical bonding applications and achieve higher retention forces by changing Silicon Grass geometry. In the case of the pull strength, better results are achieved with higher structures which yield a greater contact area between the bonded surfaces. However, as indicated by the shear tests, it is not only the geometrical shape of the Silicon Grass which has an impact on the mechanical stability of the bond, but also the mechanical property of the bulk *Si* beneath the structures. Furthermore, it follows that it is the transition from structures to bulk, which is also important for other applications, that should be considered when optimizing Silicon Grass.

4.3.2 Silicon Grass for Infrared Applications

As discussed in Section 2.2.2, Silicon Grass can be used to enhance the performance of optical or optoelectronic devices such as silicon solar cells or photo diodes. That is why several studies discuss the optical properties of Silicon Grass in the UV, optical and near infrared (IR) range up to $1.5 \mu\text{m}$ [KBS06], [RZN⁺05], [YPG⁺06]. However, in this work, an investigation on the optical properties of Silicon Grass in the IR range from $3 - 30 \mu\text{m}$ is performed. The transmittance \mathcal{T} and reflectance \mathcal{R} of two samples with single-side Silicon Grass (types A and C, see Figure 4.17) are studied, see Figure 4.20 and Figure 4.21. The *Si* wafers used are (100), double-side polished with a thickness of $425 \pm 25 \mu\text{m}$ and a resistivity of $7 - 13 \Omega\text{cm}$ (P-type, Boron).

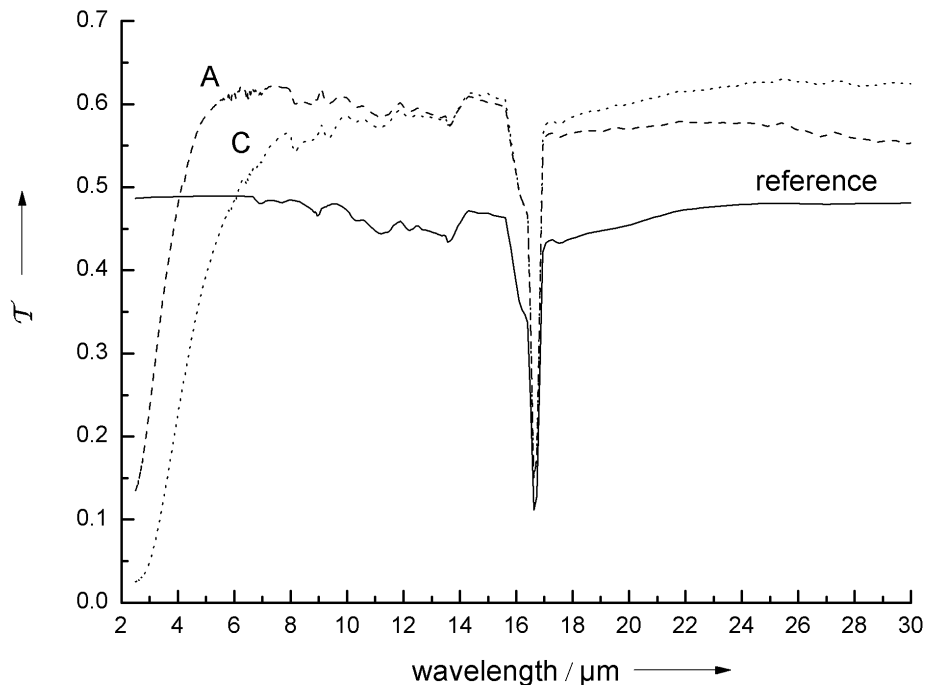


Figure 4.20: Transmission of different Silicon Grass samples.

The measurement is performed with an IR ellipsometer (SE 900, Sentech Instruments GmbH). The samples are positioned at the exit aperture, with the Silicon Grass area facing away from the detector, toward the light source (incident angle 0 degree). As a reference, an untreated, plain *Si* chip from the same wafer charge is used.

The transmission measurement shows that the surface modification turns the *Si* samples into a long-wavelength pass filter. For lower wavelengths, a strong decrease in \mathcal{T} occurs at $5 \mu\text{m}$ (A) and $8 \mu\text{m}$ (C), respectively.

For a wavelength greater $8 \mu\text{m}$, \mathcal{T} is improved for both types. It is concluded that for the long- ($8 - 15 \mu\text{m}$, LWIR) and far-wavelength ($15 - 100 \mu\text{m}$, FIR) IR, the Silicon Grass can be treated as an effective medium. It acts as a broadband anti-reflection layer by gradually matching the indices of the bulk Si to the ambient air.

\mathcal{T} of Type A is higher than that of Type C from $8 - 15 \mu\text{m}$ but lower for for wavelengths greater $15 \mu\text{m}$. This is attributed to the Silicon Grass geometry, where it is assumed that Type A with higher density is better suited for index-matching at lower wavelengths than Type C and vice versa. Other remarkable characteristics are the strong phonon absorption peak at $16.4 \mu\text{m}$ as well as the other fluctuations in the range from $6 - 25 \mu\text{m}$, which can all be attributed to lattice absorption of crystalline Si [CF54].

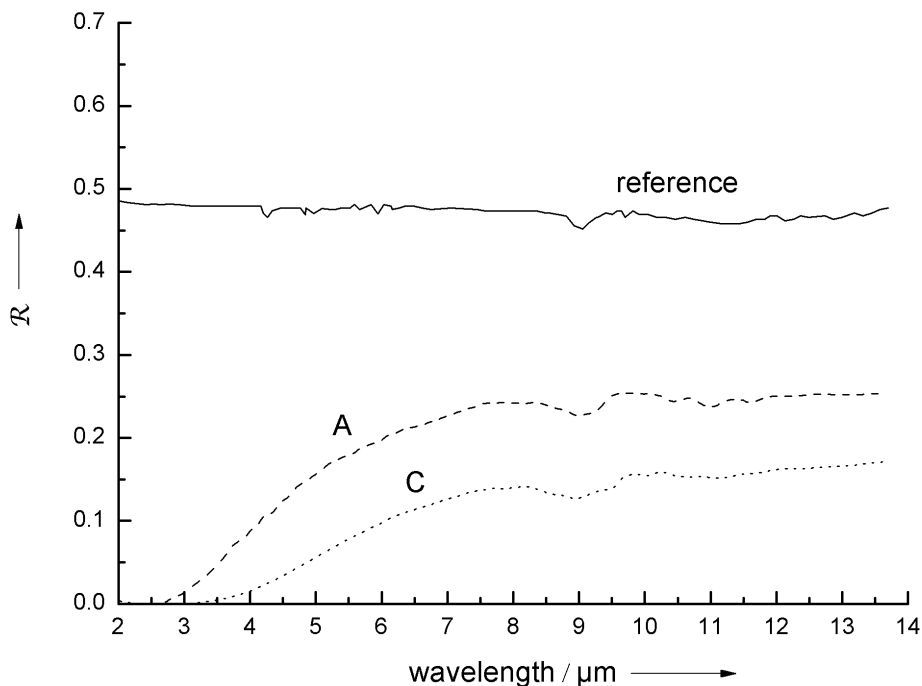
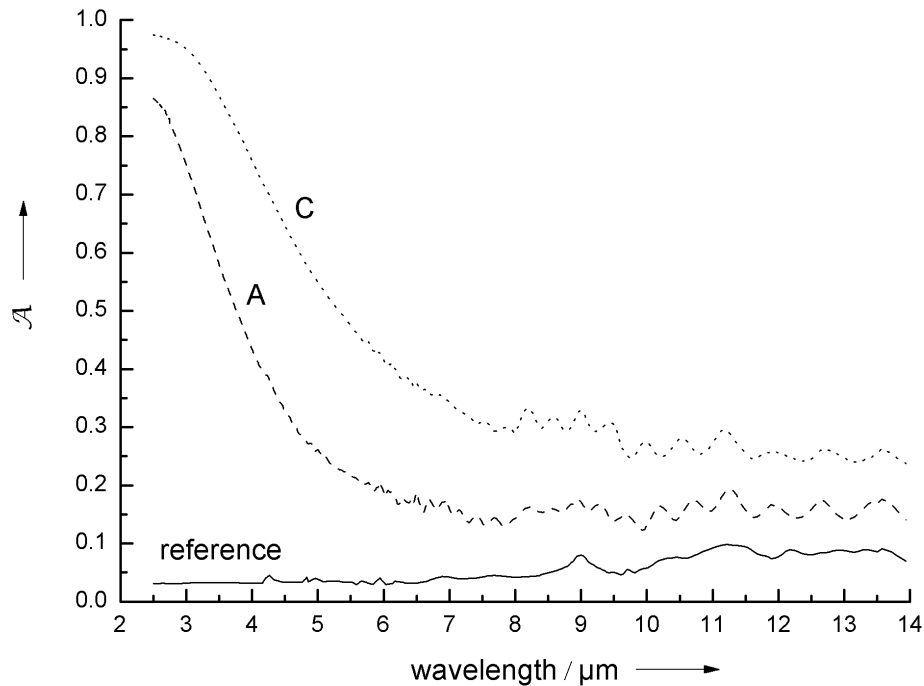


Figure 4.21: Reflection of different Silicon Grass samples. The measurement is performed with an FT-IR spectrometer (VERTEX 80v, Bruker Optik GmbH) in combination with the attached IR microscope (HYPERION 2000). As a reference, an Ag mirror is used, which is replaced by the individual samples ($2 \times 2 \text{ cm}^2$) to study the reflection normal to the surface.

In Figure 4.21 it is shown that the reflection \mathcal{R} is reduced for the whole spectrum. Below $8 \mu\text{m}$ the reflection decreases further until it reaches zero at approximately $3 \mu\text{m}$. The behavior corresponds to the transmission measurement and is explained by an increased absorption in that range. However, the geometries of the Silicon Grass can not explain this increased absorption below $8 \mu\text{m}$, as the mean distance \bar{x} of the structures is below $3 \mu\text{m}$ for both types. To determine the absorption $\mathcal{A} = 1 - (\mathcal{T} + \mathcal{R})$ of the sample, the data from both measurements is used. The plot is given in Figure 4.22.

Figure 4.22: Absorption \mathcal{A} of the samples.

The absorption of Sample \mathcal{A} is the result of the absorptions inside the Silicon Grass layer and the bulk Si :

$$\mathcal{A} = 1 - \left(e^{-\alpha_{SG}h} e^{-\alpha_{Si}(t_w-h)} \right) \quad (4.17)$$

with the attenuation coefficients α , the height of the Silicon Grass h and the wafer thickness t_w .

As the thicknesses and the attenuation coefficient α_{Si} are known, the attenuation coefficient α_{SG} can be calculated by solving Equation 4.17 for α_{SG} :

$$\alpha_{SG} = -\frac{1}{h} (\ln(1 - \mathcal{A}) + \alpha_{Si}(t_w - h)) \quad (4.18)$$

From the attenuation coefficient the extinction coefficient $k = \frac{\alpha \times \text{wavelength}}{4\pi}$ is calculated, which constitutes the imaginary part of the complex refractive index. It is plotted for wavelengths from 2 – 14 μm , see Figure 4.23.

Comparing the extinction coefficients shows that the absorption inside the Silicon Grass is orders of magnitude above that of Si . This broadband-enhanced absorption is described for a similar type of Silicon Grass, fabricated by femtosecond-pulsed laser assisted plasma etching in SF_6 [WCZ⁺01] [LLW⁺08]. Here, it is found that the high absorption arises from S impurity states induced by the fabrication process [HT03] [CCS⁺04] [KWA06].

For the c-DRIE Silicon Grass it is possible that the below-band gap absorption arises from the formation of *C* impurity surface states overlapping the *Si* band edge [MG70]. *S* can be ruled out as having a major effect because several experiments with annealed samples in N_2 and O_2 for temperatures up to $1000^\circ C$ showed no significant change in transmission, excluding adsorbed *S* at the surface. A change is expected, as at temperatures above $445^\circ C$ adsorbed *S* vaporizes in contrast to *C*, which does not sublimate until $3825^\circ C$ [Lid05]. Furthermore, no change in transmission is observed when treating the samples with O_2 plasma cleaning at elevated bias powers, which shows that the impurities can not be removed by the treatment.

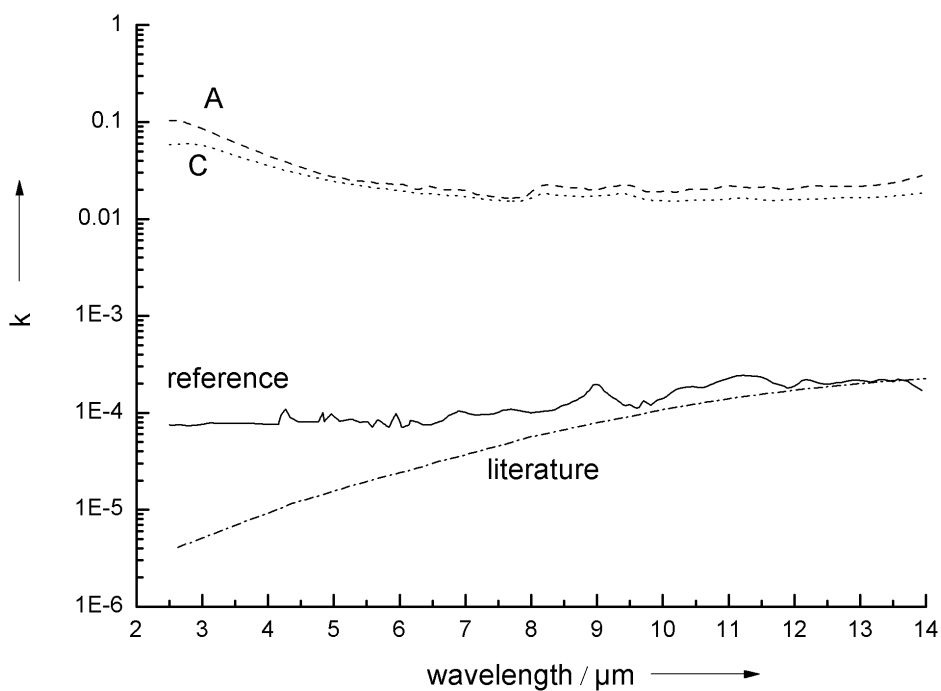


Figure 4.23: Extinction coefficient of the different Silicon Grass types.

The literature data is taken from [SKT⁺71]; carrier concentration is 10^{15} cm^{-3} .

The results show that Silicon Grass has index-matching properties and can be used to create transparent IR windows in the LWIR and FIR range. However, in order to optimize the performance, the absorption due to impurities must be limited by efficient cleaning and annealing processes. The different optical behavior of the Silicon Grass types may also be used to create long-wavelength pass filters in IR-detection devices (e.g. CO_2 gas sensors).

Further investigations are needed to fully understand the high absorption in the middle-wavelength IR (MWIR) range and clarify whether the effect can be utilized in opto-electrics. It could lead to new types of semiconductor devices (e.g. *Si*-based IR detectors).

5 Silicon Grass in Micro-Electro-Mechanical-Systems

In the following chapter, the integration of Silicon Grass in MEMS is discussed. Recommended technological processes, associated requirements and limitations as well as appropriate instructions for handling are given (Section 5.1). In order to demonstrate the integration and feasibility of Silicon Grass in MEMS, it has been used in a thermo-mechanical actuated cantilever, where it enhances the dynamic performance of the device (Section 5.2).

5.1 Integration of Silicon Grass

Because Silicon Grass is generated with a modified c-DRIE process, it can easily be integrated in CMOS fabrication process runs. Silicon Grass areas are defined by standard lithography, whereby even *KOH* etched sidewalls can be modified. Figure 5.1 exemplifies the back-end of a process run, where Silicon Grass is used to generate enlarged-surface electrical contacts in a highly integrated biosensor device.

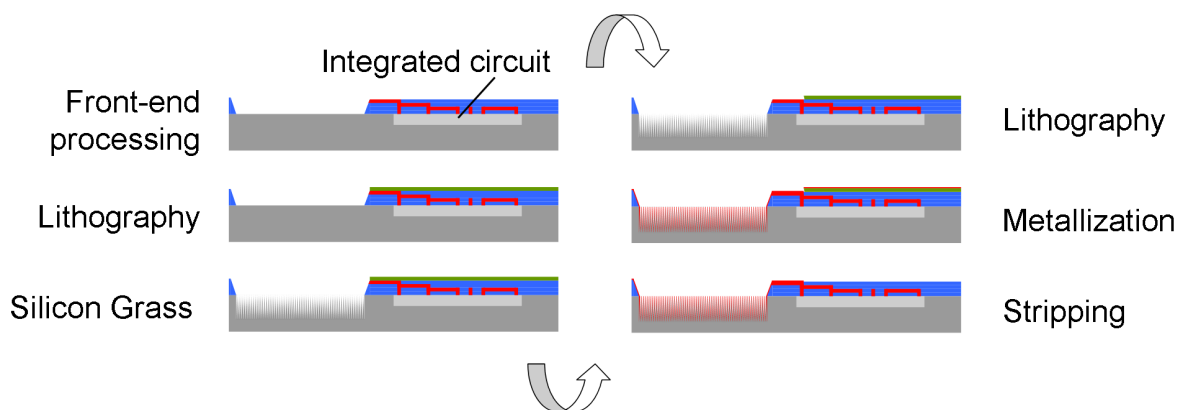


Figure 5.1: Back-end of a flow chart for a highly-integrated biosensor device with enlarged-surface electrical contacts.

The advantages of the c-DRIE fabrication of Silicon Grass are low process temperatures, simple integration and good process control for reproducible fabrication with the possibility of generating a variety of Silicon Grass types. A disadvantage is the material consumption due to the subtractive

nature of the process and the resulting restrictions for fabrication. Some requirements and limitations when processing and integrating Silicon Grass in MEMS are briefly discussed in the following.

5.1.1 Recommended Technological Processes

Removal of Carbon and Fluorocarbon Residuals

Due to the deposition of the protective FC-film within the process, the resulting Silicon Grass contains carbon and fluorocarbon residues that are found inside the trenches. These turn out to be highly resistive to standard O_2 plasma treatment or wet chemical cleaning (e.g. Caro's acid), especially in high-density Silicon Grass. A better removal can be achieved by physical sputtering in combination with O_2 plasma treatment.

Good results are achieved in the ICP-multiplex system at elevated bias power ($P_b > 20W$, $P_c = 800W$, $p = 6 Pa$, $Q_{O_2} = 45 sccm$). The duration of the process depends on the Silicon Grass type and ranges between 5 – 30 min. However, complete removal is hardly possible without affecting the *Si* structures themselves. This should be considered if high-purity *Si* surfaces are desired.

Lithography on Silicon Grass

In order to perform lithography on Silicon Grass, the following requirements and limitations must be considered.

First, in order for the resist to enter the so called WENZEL-state [Wen36], where a proper wetting and adhesion of resist is achieved, the fluor-carbon caps on the tips must be stripped off by O_2 plasma treatment. Otherwise the resist stays in the CASSIE-BAXTER-state [CB44] where poor adhesion leads to difficulties in reaching a defined thickness.

Furthermore, the lithography must be adjusted to prevent bubble formation due to outgassing of the solvent within the structures. Best results are achieved by using low viscosity resists and spinning on multiple layers with intermediate exsiccation and soft baking steps.

Next, it is found that the exposure dose must be adjusted in order to compensate for the altered optical behavior of the surface modification. For negative resists, such as *SU-8*, the exposure dose must be increased by a factor of 3–4 to achieve good cross-linking within the Silicon Grass. A detailed listing of process optimizations for joining *SU-8* and Silicon Grass is given in [Mue08].

Finally, the resolution of UV lithography is limited by the density and thickness of the particular Silicon Grass. However, in the investigations within this work, lithography on Silicon Grass is performed to define areas for its generation or removal and hence do not require resolutions below $2 \mu m$.

Fabrication of Elevated Silicon Grass

In contrast to bottom-up fabrication technologies, the top-down approach with plasma etching does not allow the fabrication of elevated Silicon Grass in one process step. To achieve this, sacrificial

Si bulk material has to be prepared previously by etching and subsequently transformed into Silicon Grass (Type A). Another possibility is etching Silicon Grass after its full wafer generation (Type B). Both procedures are depicted in Figure 5.2.

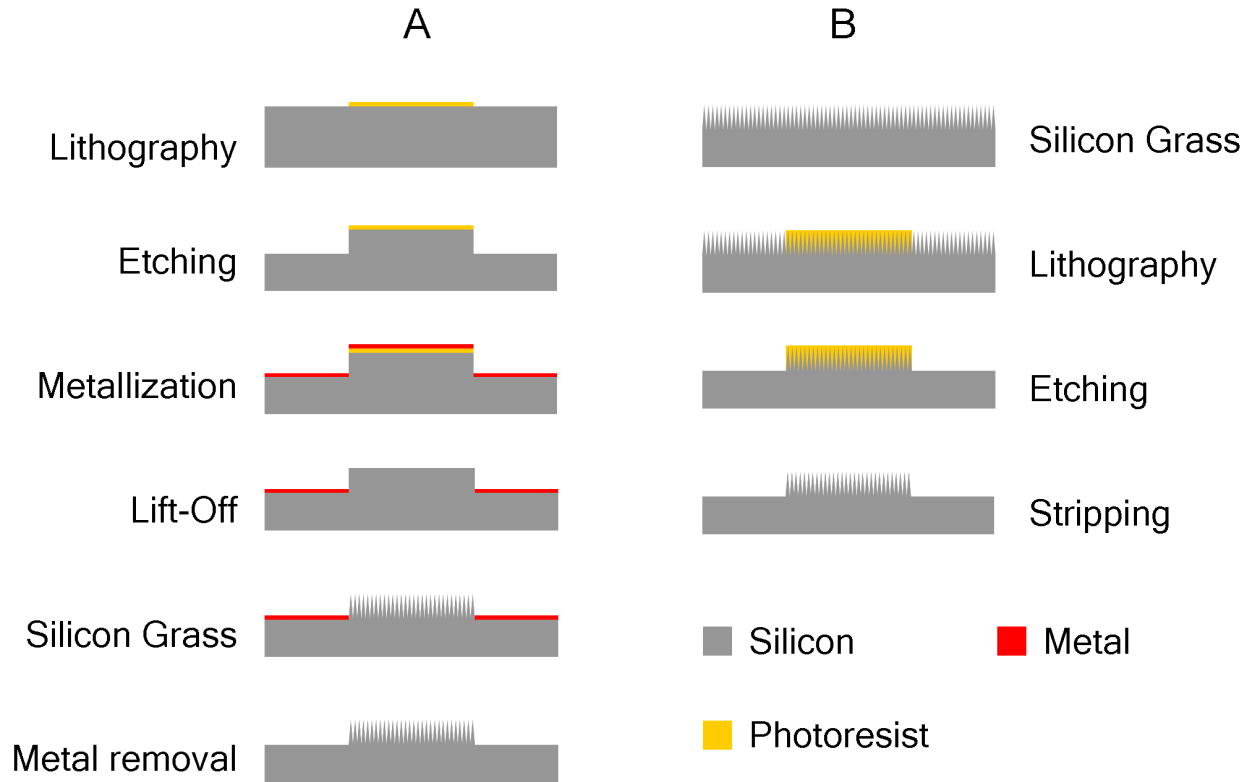


Figure 5.2: Fabrication methods of elevated Silicon Grass.

Method A involves an additional metallization step with subsequent lift-off. For etching, a plasma process which generates a negatively tapered profile (e.g. the c-DRIE) should be utilized to enable a good lift-off of the metal. Different metals such as *Au*, *Al* or *Ni* have been tested successfully in the course of this work. As mentioned in Section 3.4.4, the use of metal masks can lead to additional nanomasking via re-adsorption of sputtered metal compounds and may influence the resulting Silicon Grass. Therefore, its application should be carefully checked with regard to the desired structures and intended use.

In Method B, Silicon Grass is generated first and then etched away in the desired areas after a lithography step. Note that during this process the resist covering the Silicon Grass is also etched. therefore a sufficient thickness should be applied. Removing Silicon Grass via etching can become an intricate task due to the carbon and fluorocarbon residuals mentioned before. Therefore, a special process recipe is developed which is covered in the following.

Prevention of Silicon Grass

As explained in the introductory section, Silicon Grass generation is often unwanted. It disturbs homogeneous etching and prevents the creation of smooth trench bottoms. How Silicon Grass formation can be avoided has therefore been an important question in the RIE etching process. From the findings of this work, some guidelines are also deduced to effectively avoid the surface structure in c-DRIE processes which are summarized below. All parameter values given refer to the ICP-multiplex of the present work only:

- Keep deposition step time short, and use proper etch step time to ensure complete residual removal.
- Ramp etch step time when etching, as nanomasking by etch products becomes stronger in deeper trenches.
- Add 10 – 20 % O_2 to SF_6 to enable FC-film etching by O .
- Use high power and low pressure mode ($P_c > 650 W$, $p < 3 Pa$) to deposit high FC-ratio films, which are removed more easily.
- Use low bias power during etching ($P_b < 15 W$) to prevent attraction of the carbon dust that is formed.
- If high bias power is needed, use a time delay after deposition to flush carbon dust from the chamber prior to etching.
- Start the c-DRIE process with an etch step to remove the natural oxide layer.
- Do not use metal or metal-containing masks to prevent non volatile, sputtered mask residuals from masking.

It might be misunderstood that increased bias power leads to the prevention of Silicon Grass, as this enhances the physical abrasion of the FC-film. However, all experiments performed show that this instead increases formation. The most important aspect is to ensure an adequate level of undercutting, as lateral etching is crucial to remove the clusters.

Removal of Silicon Grass

To remove the Silicon Grass and continue etching into the bulk, a cyclic process recipe is developed. At first, a short O_2 cleaning step with applied bias voltage is used to remove remaining residuals of the Silicon Grass process. It is followed by an isotropic etching step with SF_6/O_2 to etch the Si and eliminate the structures. These two steps should be repeated sequentially until the Si is clean. Depending on the type of Silicon Grass, the interface between structures and bulk can be several microns thick, requiring prolonged etching. This must be accounted for when applying the protective

resist layer on the Silicon Grass. The isotropic etching also leads to an undercut which must be considered.

Cleaning of Silicon Grass

As the surface modification is created by a self-masking mechanism, the geometrical shape of the generated structures is statistical to a certain degree so that, for example, the diameters of the features can only be specified within a certain range. This geometrical variation leads to the decrease of density observed during structure development (see Section 4.1.2). From this follows that after generation, disintegrated needles can be present within the Silicon Grass and should be removed by H_2O in a waver rinser/dryer. This technique can also be used to remove highly fragile needles. The remaining structures, however, are stable and will only be destroyed due to external mechanical forces (e.g. scratching, wafer fragmenting, rupture of bonded parts). Therefore, when dealing with Silicon Grass some precautions are necessary to ensure safe and proper use. Some handling instructions are given in the following.

5.1.2 Health Hazards and Handling Instructions

As Silicon Grass consists of a large number of nano-sized *Si* structures which can become airborne, some considerations about safe and proper use as well as practical handling instructions are given.

Health Hazards

Because nanomaterials have been introduced in variety of different consumer products, questions about the potential health and environmental hazards of nanoparticles and nanowires arose and required timely answers. Therefore, a large number of publications have dealt with this subject in recent years [OBI09]. However, the challenge lies with the great variety of nanomaterial used, so that general information about its toxicity cannot be given. Furthermore, standardized methods are still under development for evaluating the respective hazards.

To date, no information on the potential health hazard of *Si* nanowires, or more specifically, Silicon Grass could be found. Their potential danger arises from their small sizes, reactive surfaces and high mobility. Because some types of nanoparticles are evidentially toxic and the shape of the structures is somewhat reminiscent of asbestos, precautionary principles are advised when dealing with Silicon Grass. Therefore, the following list of handling instructions is given to provide the maximum safety possible.

Handling Instructions

- Wear protective clothing (gloves, mask, safety goggles)
- Store and transport the probes with Silicon Grass in closed and labeled boxes
- Perform fragmentation or mechanical testing under a flue or within a glovebox
- Clean or dispose of equipment after use
- Dispose of Black Silicon within special containers or use spray-on adhesives to agglutinate
- Avoid contact with or mechanical rupture of Silicon Grass

Furthermore, some additional remarks concerning the design and processing technology of Silicon Grass are suggested.

- Minimize Silicon Grass areas (avoid full wafer generation)
- If full wafer generation is necessary, provide for unstructured areas at the wafer rim for safe handling with tweezers
- Use Silicon Grass in the back-end fabrication process if possible
- Use resist to cover and protect the Silicon Grass whenever possible (e.g. for dicing)

5.2 Feasibility Test - A Thermo-Mechanical Actuator with Integrated Silicon Grass

To demonstrate the integration and feasibility of Silicon Grass in MEMS, it has been used in a thermo-mechanical actuated cantilever. The device is based on *Si* and the photosensitive polymer *SU-8* and demonstrates large deflection, low-temperature operation (e.g. for sensing or manipulating biological specimens [KCL⁺03] [CKHK06]).

During long-term operation, the mechanical stress generated at the interface often results in poor adhesion and may lead to the polymer layer being peeled off. Furthermore, the dynamic performance is often limited by the low thermal conductivity of the polymer so that only low switching frequencies are achieved [JKC06]. By creating a composite material layer of *Si* and *SU-8*, combining the high thermal conductivity of *Si* ($\lambda_{Si} = 156 \text{ Wm}^{-1}\text{K}^{-1}$) and the high thermal expansion of *SU-8* ($\alpha_{SU-8} = 52 \cdot 10^{-6} \text{ K}^{-1}$), the dynamic performance of such devices greatly enhanced. An illustration is given in Figure 5.3.

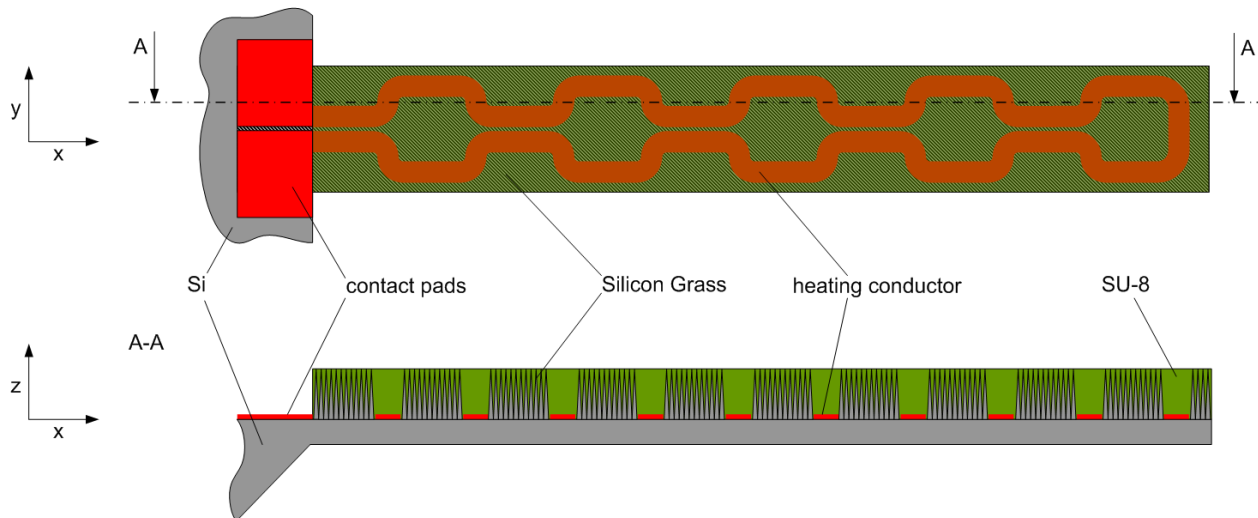


Figure 5.3: Sketch of thermo-mechanical actuated bimorph cantilever based on *Si* and *SU-8* with integrated Silicon Grass for enhanced performance.

A similar concept for *Si/SU-8* based cantilevers is proposed in [WDLS08] where a silicon comb-structure with embedded *SU-8* is used to increase deflection and dynamic performance. The concept of improved thermal conductivity and rigidity of *SU-8* through integration of *Si* structures is also used in other types of applications such as micro-grippers [DWSL06] and in-plane actuators [LDG⁺07].

5.2.1 Actuator Performance

Maximum Deflection

Deflection R^{-1} (defined as the inverse radius of the bending cantilever) can be derived by assuming a constant temperature distribution and equilibrium of forces and moments in the cross-section of the cantilever beam and is given in [Mue10]. It can be expressed as follows:

$$R^{-1} = \frac{1}{t_1 + t_2} \frac{6 \Delta T (\alpha_1 - \alpha_2) \left(1 + \frac{t_1}{t_2}\right)^2}{3 \left(1 + \frac{t_1}{t_2}\right)^2 + \left(1 + \frac{t_1 E_1}{t_2 E_2}\right) \left(\left(\frac{t_1}{t_2}\right)^2 + \frac{t_2 E_2}{t_1 E_1}\right)} \quad (5.1)$$

The indices refer to the Si layer (1) and the $SU-8$ layer (2), respectively. The above expression describes the exact deflection for bimorph cantilevers and, in contrast to the commonly used STONEY formula, is valid at arbitrary thickness combinations.

Deflection can also be derived by another mathematical approach, based on the principle of minimized total energy, which is covered in [GCG⁺00]. Here, a unified theory is formulated that allows the calculation for multiple layers as well as for different actuation principles. The formula is given below:

$$R^{-1} = \frac{6 \Delta T (\alpha_1 - \alpha_2) (t_1 + t_2)}{t_1 t_2 \left[\left(\frac{t_2}{t_1}\right)^2 \frac{E_2 (1-\nu_1)}{E_1 (1-\nu_2)} + 4 \frac{t_2}{t_1} + 6 + 4 \frac{t_1}{t_2} + \left(\frac{t_1}{t_2}\right)^2 \frac{E_1 (1-\nu_2)}{E_2 (1-\nu_1)} \right]} \quad (5.2)$$

The method represents a more exact way, because it also accounts for the POISSON'S ratio ν of the materials and should be applied when these differ from one another. As $\nu_{Si} = 0.26 \dots 0.28 \approx \nu_{SU-8} = 0.22 \dots 0.33$, both of the given formulae can be applied.

Thermal Network Model

To understand how the integration of Silicon Grass brings about a dynamic performance enhancement, the heat flows inside the cantilever are considered (Figure 5.4) and a thermal network model is set up, see Figure 5.5 a).

Because the low thermal conductivity of $SU-8$ ($\lambda_{SU-8} = 0.3 \text{ Wm}^{-1}\text{K}^{-1}$) affects the heat flow in and out of its thermal mass, the vertical conductive resistance of the $SU-8$ layer is split into two equal thermal resistances $R_{th,2,cd,v}$. Similarly, this split is also performed for the Si with $R_{th,1,cd,v}$.

In Figure 5.6 the total lateral and vertical conductive resistances of the corresponding $SU-8$ and Si volumes, as well as the total convective and radiative resistances of the respective surfaces are plotted for lengths from $100 \mu\text{m} < l < 10000 \mu\text{m}$ with width $w = 100 \mu\text{m}$ and the thicknesses $t_2 = 35 \mu\text{m}$ and $t_1 = 10 \mu\text{m}$.

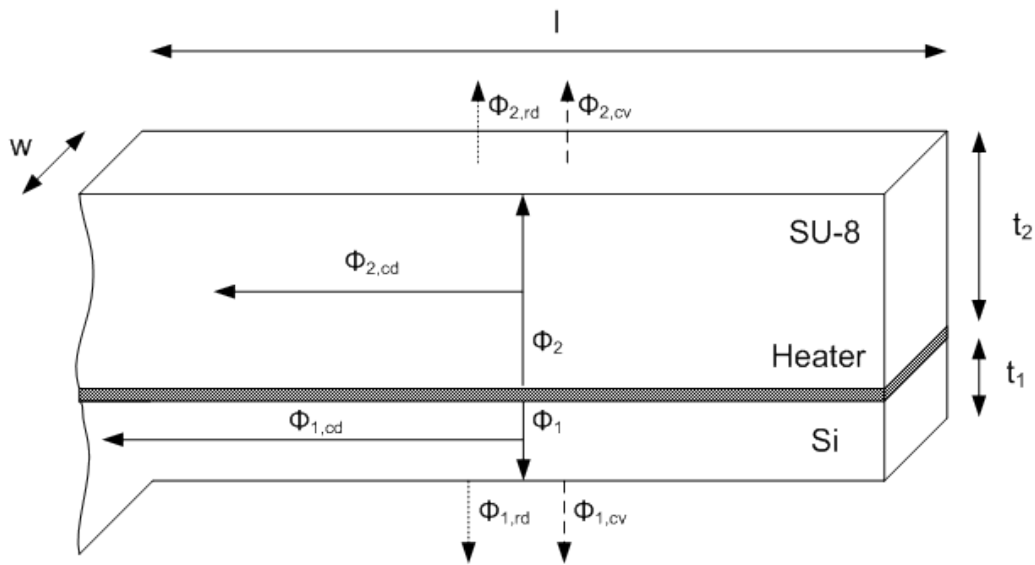


Figure 5.4: Sketch of the layer construction with heat flows for the $Si/SU-8$ cantilever. The indices (1) and (2) refer to Si and $SU-8$; (cd), (cv) and (rd) to conduction, convection and radiation, respectively.

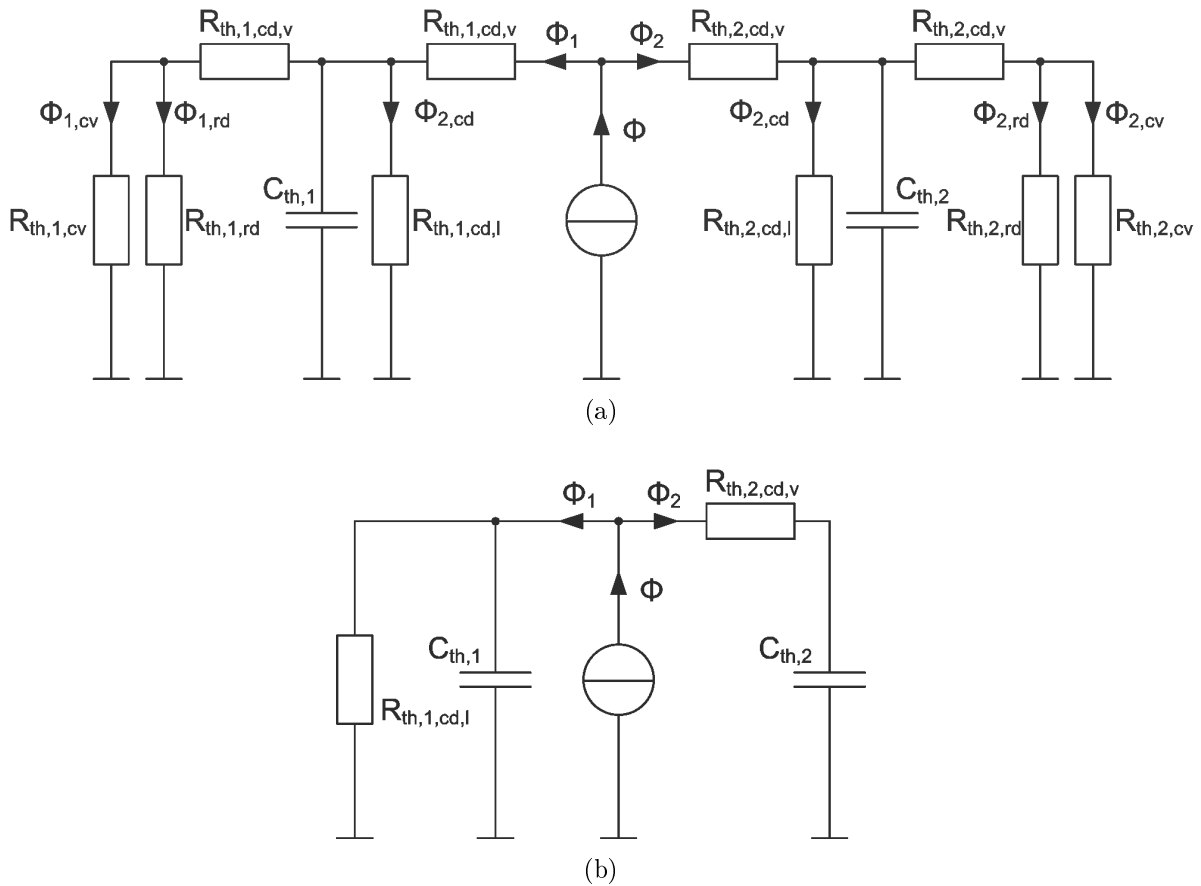


Figure 5.5: a) Thermal network model and b) same model after simplification.

The indices (l) and (v) refer to lateral and vertical conduction, respectively.

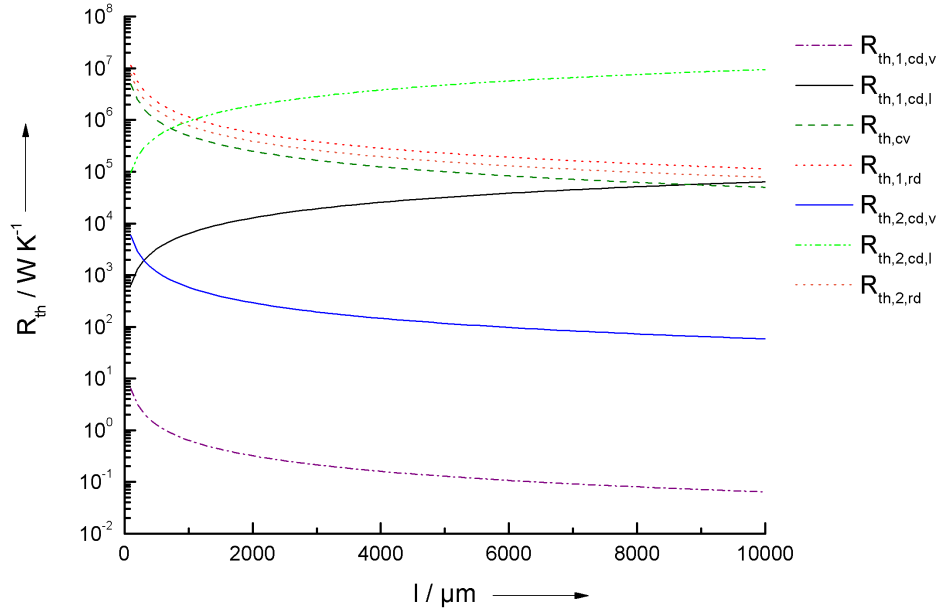


Figure 5.6: Plot of the thermal resistances for $100 \mu m < l < 10000 \mu m$ at $200^\circ C$.

The resistances are calculated according to [GD06].

From the comparison the following simplifications are derived:

- The vertical conductive resistance of Si , $R_{th,1,cd,v}$ is several orders of magnitude smaller than the others and can be neglected.
- The lateral conductive resistance in the $SU-8$ layer $R_{th,2,cd,l}$ is found to be much larger than that in Si , thus $\phi_{2,cd}$ can be neglected.
- At temperatures below $200^\circ C$, conductive and radiative resistances only significantly affect the heat flow for $l > 5000 \mu m$ and therefore $\phi_{1,cv}$, $\phi_{1,rd}$, $\phi_{2,cv}$ and $\phi_{2,rd}$ are all assumed zero.
- The vertical conductive resistance in $SU-8$ can be assumed zero for cantilever lengths above $2000 \mu m$, but when $l < 300$, where $R_{th,2,cd,v} > R_{th,1,cd}$, it significantly affects the heat flow in the assembly.

From these simplifications it is deduced that for temperatures below $200^\circ C$ and cantilever lengths below $2000 \mu m$ the thermal network model above can be reduced to the one given in Figure 5.5 b).

The integration of Silicon Grass decreases $R_{th,2,cd,v}$ and thus reduces the effective thermal resistance of the system. Heating is defined by $R_{th,2,cd,v}$ (as C_1 is charged instantly), while for cooling $R_{th,1,cd}$ and $R_{th,2,cd,v}$ are in serial connection. The dynamic behavior of the device is expressed by the thermal

time constant τ , which is calculated from the product of effective thermal capacity $C_{th,eff}$ and effective thermal resistance $R_{th,eff}$.

$$\tau = C_{th,eff} R_{th,eff} \quad (5.3)$$

The time constant for heating is calculated as follows:

$$\tau_{heat} = C_{th,2} R_{th,2,cd,v} = \rho_2 c_2 t_2 w l \frac{t_2}{\lambda_2 w l} = \frac{\rho_2 c_2}{\lambda_2} t_2^2 \quad (5.4)$$

with the densities ρ and the specific heat capacities c .

The time constant for cooling is defined by both resistances $R_{th,1,cd}$, $R_{th,2,cd,v}$ and capacitances $C_{th,1}$ and $C_{th,2}$. In the case where $l > 2000 \mu m$, then $R_{th,1,cd} \ll R_{th,2,cd,v}$ and τ_{cool} can be approximated with:

$$\begin{aligned} \tau_{cool} &= (C_{th,1} + C_{th,2}) R_{th,1,cd,l} = (\rho_1 c_1 t_1 w l + \rho_2 c_2 t_2 w l) \frac{l}{\lambda_1 t_1 w} \\ &= \frac{l^2}{\lambda_1 t_1} (\rho_1 c_1 t_1 + \rho_2 c_2 t_2) \end{aligned} \quad (5.5)$$

However, to benefit from the effects of the Silicon Grass, a design with $l < 300 \mu m$ is considered, where $R_{th,1,cd} \approx R_{th,2,cd,v}$. Then if $C_{th,1} < C_{th,2}$, τ_{cool} can be approximated with:

$$\begin{aligned} \tau_{cool} &= C_2 (R_{th,1,cd,l} + R_{th,2,cd,v}) \\ &= \rho_2 c_2 t_2 w l \left(\frac{l}{\lambda_1 t_1 w} + \frac{t_2}{\lambda_2 l w} \right) \\ &= \frac{\rho_2 c_2}{\lambda_1} \frac{t_2}{t_1} l^2 + \frac{\rho_2 c_2}{\lambda_2} t_2^2 \end{aligned} \quad (5.6)$$

Finally, the time constant for one full cycle τ_{cyc} and the operating frequency $f = \tau_{cyc}^{-1}$ can be calculated. Usually $\tau_{heat} < \tau_{cool}$, hence $\tau_{cyc} = 2\tau_{cool}$. For the two cantilevers shown in Figure 5.11 $\tau_{cyc,a} = 9.6 s$ and $\tau_{cyc,b} = 0.72 s$. For a cantilever with $l = 100 \mu m$, $b = 20 \mu m$, $t_1 = 5 \mu m$ and $t_2 = 15 \mu m$, $\tau_{cyc} = 4.0 ms$.

Figure 5.7 plots the operating frequency f and the maximum deflection R^{-1} for varying thickness ratio $t_1 t_2^{-1}$ as well as for varying length l of the cantilever. It shows that the thickness ratio greatly affects both system parameters.

First, if the thickness of the *Si* layer becomes smaller, the heat flow during cooling is constrained, thus decreasing f . Second, a maximum deflection is reached for a specific thickness ratio depending on the E-moduli of the materials and design restrictions. These design restrictions are given by either a fixed t_1 , a fixed t_2 or the total thickness of the beam $t_{beam} = t_1 + t_2$. For the plot in Figure 5.7 the *SU-8* layer thickness is fixed at $t_2 = 15 \mu m$.

Furthermore, the inversely quadratic influence of l on f is demonstrated and shows that cantilevers must be short in order to enter the *kHz* operating range. It is the thermal capacity of the *SU-8* layer that is most affective.

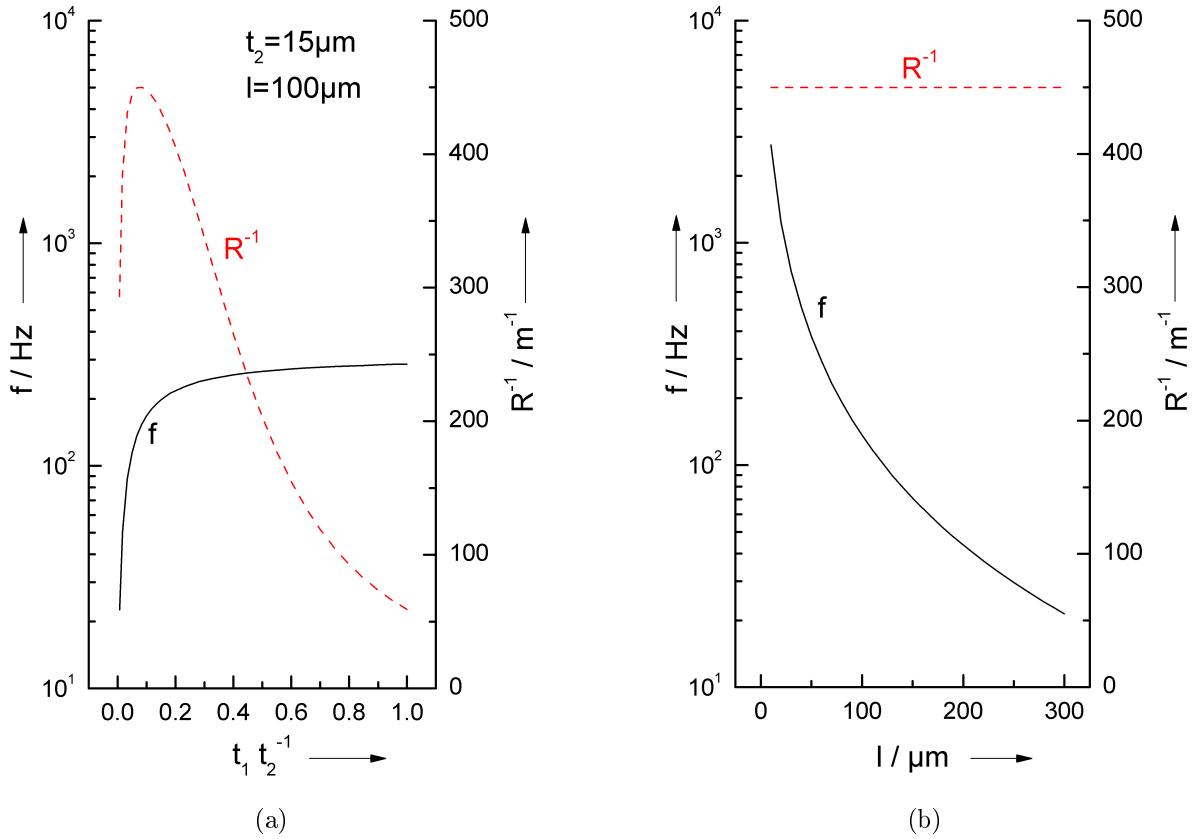


Figure 5.7: Influence of a) varying thickness ratio $t_1 t_2^{-1}$ and b) cantilever length l on the operating frequency f and the maximum deflection R^{-1} .

5.2.2 Influence of Silicon Grass on the Thermal Properties and Performance

Thermal Model

The integration of Silicon Grass introduces a change of λ because the thermal conductivity is increased by the Si structures. In order to approximate λ_{SG} , a mathematical approach is used, which is detailed in the following.

λ_{SG} can be calculated by λ_2 and the ratio of the thermal resistances:

$$\lambda_{SG} = \frac{R_{th,2}}{R_{th,SG}} \lambda_2 \quad (5.7)$$

with

$$R_{th,2} = \frac{t_2}{\lambda_2 A} \quad (5.8)$$

To find $R_{th,SG}$ an example is considered where the Silicon Grass needles have a cone-shaped geometry and are surrounded in the polymer matrix of the $SU-8$. The model with the equivalent thermal network is sketched in Figure 5.8.

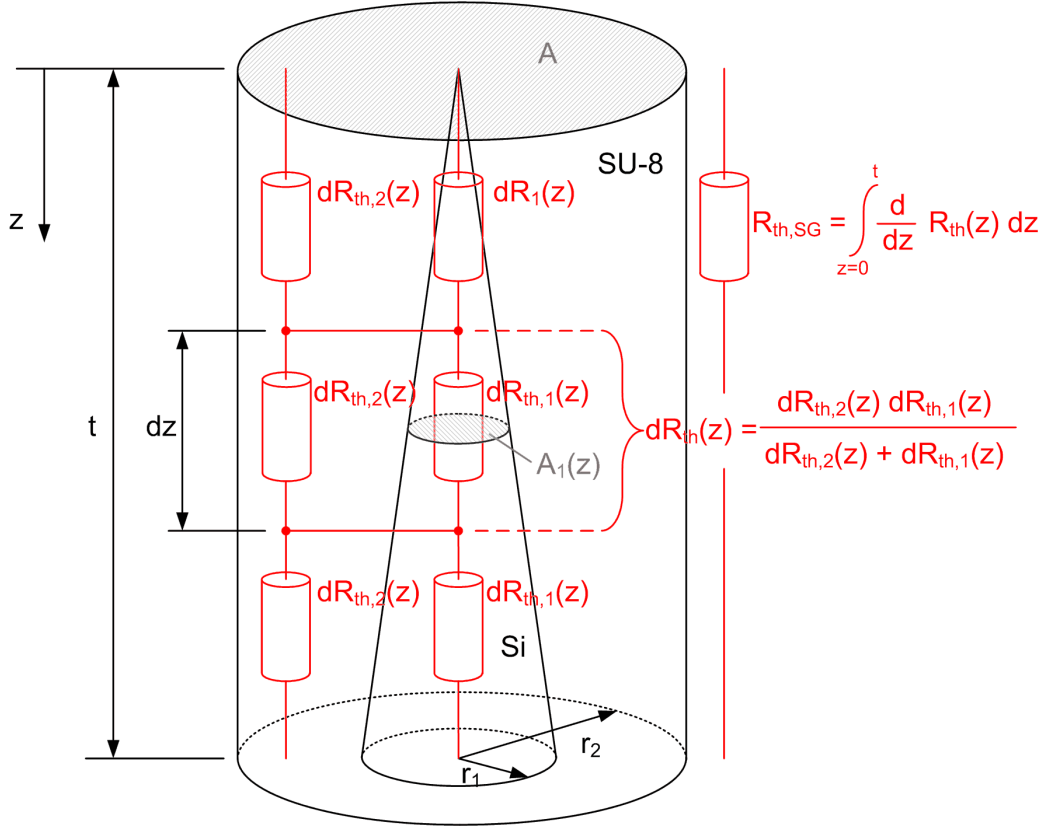


Figure 5.8: Sketch of the model with the equivalent thermal network to calculate λ_{SG} .

Since $r_2 \ll t$ with $r_2 \approx \frac{\bar{x}}{2} = 0.25 \dots 0.5 \mu m$ (\bar{x} mean distance of the Silicon Grass), the lateral thermal resistances are neglected.

$R_{th,SG}$ is calculated by integrating the infinitesimal resistances $\frac{d}{dz} R_{th}(z)$ from $z = 0$ to t :

$$R_{th,SG} = \int_{z=0}^t \frac{d}{dz} R_{th}(z) dz \quad (5.9)$$

where $dR_{th}(z)$ is calculated from the parallel circuit of $dR_{th,1}(z)$ and $dR_{th,2}(z)$

$$dR_{th}(z) = \frac{dR_{th,1}(z) dR_{th,2}(z)}{dR_{th,1}(z) + dR_{th,2}(z)} \quad (5.10)$$

$dR_{th,1}(z)$ and $dR_{th,2}(z)$ are calculated by:

$$dR_{th,1}(z) = \frac{dz}{\lambda_1 A_1(z)} \quad (5.11)$$

and

$$dR_{th,2}(z) = \frac{dz}{\lambda_2 (A - A_1(z))} \quad (5.12)$$

Insertion of 5.11 and 5.12 into 5.10 and simplification resolves into

$$dR_{th}(z) = \frac{dz}{\lambda_1 A_1(z) + \lambda_2 (A - A_1(z))} \quad (5.13)$$

At a given z the cross-section of the *Si*, $A_1(z)$, is constant, hence the derivative of $dR_{th}(z)$ is

$$\frac{d}{dz} R_{th}(z) = \frac{1}{\lambda_1 A_1(z) + \lambda_2 (A - A_1(z))} \quad (5.14)$$

Finally $\frac{d}{dz} R_{th}(z)$ must be integrated from $z = 0$ to t (Equation 5.9), taking into account the geometrical change of $A_1(z)$

$$A_1(z) = \left(r_1 \frac{z}{t} \right)^2 \pi \quad (5.15)$$

which results in

$$\begin{aligned} R_{th,SG} &= \int_{z=0}^t \frac{1}{\lambda_1 \left(r_1 \frac{z}{t} \right)^2 \pi + \lambda_2 \left(r_2^2 \pi - \left(r_1 \frac{z}{t} \right)^2 \pi \right)} dz \\ &= \frac{t}{\pi r_2 r_1 \sqrt{\lambda_2 (\lambda_1 - \lambda_2)}} \arctan \left(\frac{r_1 (\lambda_1 - \lambda_2)}{r_2 \sqrt{\lambda_2 (\lambda_1 - \lambda_2)}} \right) \end{aligned} \quad (5.16)$$

The parameters in Equation 5.16 can now be exchanged to relate them to the Silicon Grass parameters height h and density D discussed in the previous chapters. Substituting for r_2 with the half of the mean distance of the Silicon Grass $\frac{\bar{x}}{2} = \frac{1}{2\sqrt{D}}$ (see Equation 4.6) and for t with the Silicon Grass height h . The quantity r_1 becomes the base radius of the needles r_b . After substitution 5.16 and 5.8 is inserted in 5.7 and simplified to get λ_{SG} :

$$\lambda_{SG} = 2r_b \sqrt{D} \frac{\sqrt{\lambda_2 (\lambda_1 - \lambda_2)}}{\arctan \left(2r_b \sqrt{D} \frac{(\lambda_1 - \lambda_2)}{\sqrt{\lambda_2 (\lambda_1 - \lambda_2)}} \right)} \quad (5.17)$$

The thermal conductivity of the composite with Silicon Grass with dimensions $h = 15 \mu m$, $D = 1 \mu m^{-2}$ and $r_b = 250 nm$ is calculated to be $\lambda_{SG} = 2.3 W m^{-1} K^{-1}$. This shows that the thermal conductivity can be increased by a factor of $\Lambda = \frac{\lambda_{SG}}{\lambda_2} \approx 8$.

If a cylindrical shape is used for the *Si* structures to approximate the thermal conductivity, even greater factors are the result ($\lambda_{SG} = 33 W m^{-1} K^{-1}$ with $\Lambda > 110$, with equivalent geometry). As the real geometry of the Silicon Grass cannot be defined exactly, but lies between the cone-shaped and cylindrical geometry, the thermal conductivity is assumed to be at least as high as given by Equation 5.17. However, this thermal model is only valid for Silicon Structures where the height of the features h is significantly larger than their mean distance \bar{x} .

Dynamic Enhancement

The model shows that Silicon Grass strongly increases the thermal conductivity of the $SU-8$ layer. In order to visualize the dynamic enhancement, the maximum operating frequencies of the cantilevers are compared. This is displayed in Figure 5.9, where the ratio of operating frequency Φ of different cantilevers is plotted against the ratio of the thermal conductivities Λ to demonstrate the dynamic improvement due to integrated Silicon Grass.

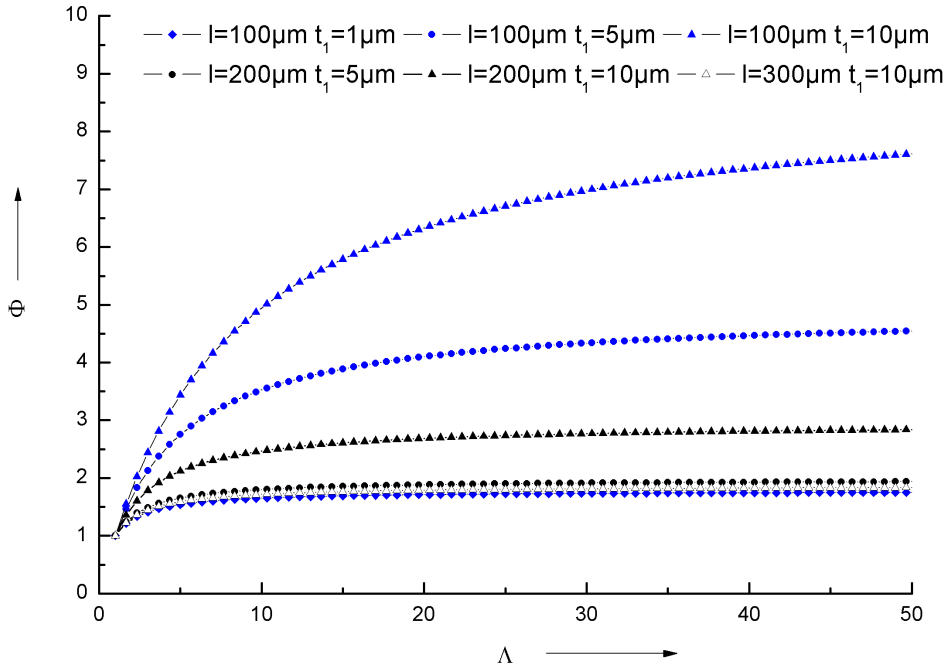


Figure 5.9: Dynamic enhancement given by the ratio of maximum operating frequency Φ as function of the ratio of the thermal conductivities Λ for different cantilevers.

The thickness of the $SU-8$ layer is $15 \mu m$.

The graph shows that the highest enhancement can be achieved for ‘short’ cantilevers with ‘thick’ Si layers. For $l = 100 \mu m$ and $t_1 = 10 \mu m$, cantilevers can operate up to seven times faster when Silicon Grass is integrated.

Furthermore, it is seen that Φ increases strongly for low values of Λ . After that, a further increase of Λ leads to no significant increase of the operating frequency f . In reference to the findings from the previous section, where $\Lambda > 8$, it is stated that the standard Silicon Grass is well suited to enhance devices with this geometrical layout.

5.2.3 Technology

In the following, the technological realization of the cantilever is discussed briefly. Figure 5.10 shows a simplified flowchart.

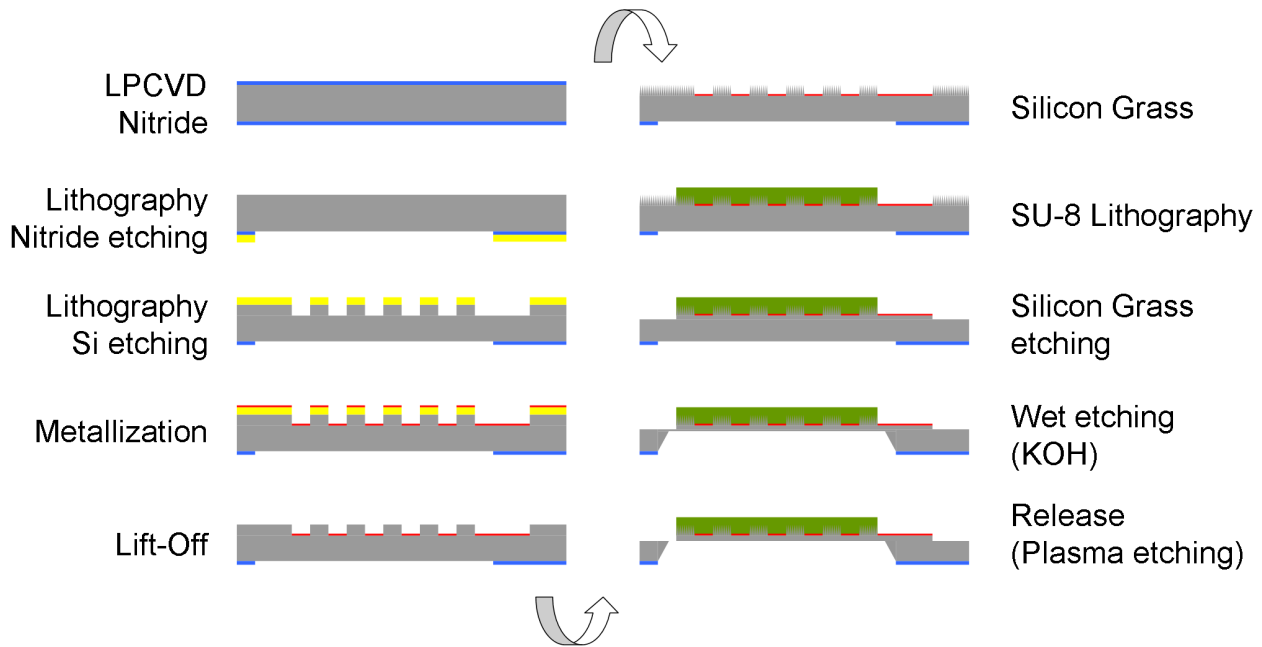


Figure 5.10: Simplified technological flowchart for the fabrication of the thermo-mechanical actuated bimorph cantilever.

At first, a 100 nm nitride layer is generated via LPCVD as a mask for the later wet chemical etching in KOH . The layer is structured either by wet chemical or plasma etching. Flat alignment is crucial in this first lithography step, as the wet chemical etching and deflection of the cantilever depend on crystallographic orientation.

After this, c-DRIE etching follows, creating the sacrificial Si blocks for the Silicon Grass process and metallization. The metallization is performed with Ni (300 nm) and an additional Cr (10 nm) adhesion layer to create the heating conductor and provide an etch mask for the following Silicon Grass generation.

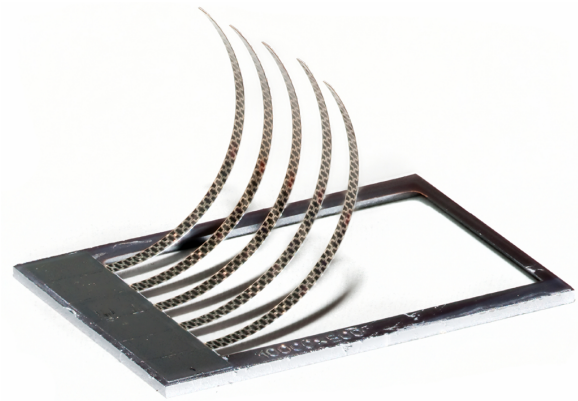
Next, the $SU-8$ lithography is carried out with a spin-on of multiple layers of $SU-82005$ and $SU-82010$ with intermediate exsiccation and soft baking steps to guarantee a good filling of the Silicon Grass with polymer. The exposure dose is increased to 500 mJ/cm^2 instead of 160 mJ/cm^2 for an increased crosslinking.

Silicon Grass etching with the described sequential process (see Section 5.1.1) follows. Due to the lateral etching of the isotropic process, an undercut of the mask has to be considered.

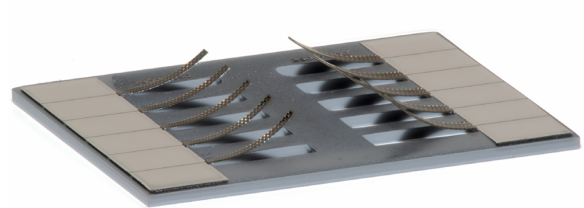
The Si layer thickness of the cantilever is then defined by c-DRIE etching, and one-sided wet chemical etching in KOH is subsequently performed until a layer of $10\text{ }\mu\text{m}$ remains.

Finally, plasma etching from the backside is used, until the cantilevers are released.

Figure 5.11 shows the fabricated cantilevers in different geometrical layouts. The detailed flowchart is given in the appendix A. Additional explanations about the design, of the technological processes as well as a functional characterization is found in [Mue10].



(a) $10.000 \times 500 \mu m$



(b) $2.500 \times 500 \mu m$

Figure 5.11: Cantilevers fabricated with different geometrical layouts [Mue10].

6 Summary and Outlook

In this final chapter, the key findings of the investigations performed are summarized and briefly discussed with respect to the intended goal of this work (Section 6.1). After that, an outlook is given in which follow-on studies are suggested and some promising future aspects and applications of the nano-scale surface modification Silicon Grass are also covered (Section 6.2).

6.1 Summary

Silicon Grass is a nano-scale surface modification which is formed by self-organizing processes in plasma etching. It can be actively used to enable new functionalities or enhance the performance of MEMS, BioMEMS or MOEMS. Its low-cost generation with standard MEMS fabrication equipment makes it a promising research subject.

The goal of this work is the investigation of the formation, modification and application of Silicon Grass from the c-DRIE process. In this regard, the central aspect is the reproducible and controlled generation as well as the selected modification of the Silicon Grass intended to fit specific applications.

Chapter 3 introduces a formation theory of nanomasking, the self-organized mechanism which initiates Silicon Grass generation. It is derived from the findings of various investigations which are covered in this chapter.

In the c-DRIE process, nanomasking is caused by various mechanisms. In order to reproducibly generate it on *Si*, a variant must be selected which can be governed. This can be achieved by the controlled abrasion of the deposited inhibiting film in the etching step.

For this purpose, monitoring the 703.8 nm emission line of *F* by OES is a useful indicator for finding the appropriate process window for nanomasking. The method enables reproducible initiation, even for varying process conditions, and will help to transfer the process to other systems.

Different morphological and chemical studies by SEM, AFM, XPS and AES show that the leftover material consists of carbon-rich, filament-like clusters with a low FC-ratio ($R_{FC} = 0.38$) and hence exhibits a high thermal and chemical resistance. Sputtered metal compounds from the chamber as well as adsorbed *S* are ruled out as the source of nanomasking in the c-DRIE.

The initial morphology of the nanomask is defined by the morphology and laterally varying chemical composition of the deposited FC-film, but can also be influenced by the process parameters deposition step time τ_{dep} , coil power P_c and bias power P_b to generate different types of nanomasks. A process

analysis shows that densities can vary between $14.1 \mu\text{m}^{-2}$ and $31.9 \mu\text{m}^{-2}$. Deposition step time τ_{dep} is identified to be the most influential parameter affecting the morphology of the nanomask.

Various influences on nanomask formation and morphology are investigated. Here, the phenomenon of carbon dust formation in C_4F_8 polymerizing plasmas is most important, as it greatly affects the morphology when the macro molecules are incorporated in the FC-film. In addition to the carbon dust formation, the influence of O_2 addition, natural oxide, contamination and masking are also discussed.

In Chapter 4 the formation and subsequent modification of the structures are covered.

Silicon Grass is produced by continued etching of the Si in the presence of a nanomask. Once a certain surface roughness is introduced, the morphology develops into the needle-like structures. By investigating the progression of Silicon Grass formation, it is shown that the characteristic geometrical features of the structures (structure height h , density D and profile) undergo significant changes during the process. Furthermore, it is found that, depending on the applied process parameters, the resulting profiles and sidewall morphology of the Silicon Grass can be changed. Here, the influence of the two important process parameters deposition step time τ_{dep} and bias power P_b during etching is investigated. It is found that height and density of the Silicon Grass can be varied by a change of τ_{dep} , while P_b has a strong influence on the profile of the structures.

To prepare the features for certain applications, they must be metallized by subsequent processes. In this chapter the metallization techniques (PVD and electroless plating) are investigated. It is shown that the metallization techniques provide only poor coverage of the structures and hence enhanced metallization techniques should be considered.

Finally, the chapter discusses two exemplary applications: mechanical bonding and IR applications, and it is shown that an adaption of Silicon Grass to specific applications is feasible. Here, the suitability of different Silicon Grass types is investigated. If Silicon Grass for bonding applications is desired, the height as well as the transitional region between structures and bulk Si are important. Furthermore, it is found that Silicon Grass has index-matching properties and exhibits broad-band anti-reflecting properties in the LWIR and FIR range. In the NIR and MIR range it shows an unusual level of absorption dependent upon the specific Silicon Grass geometry. The effect should be investigated in future works.

Chapter 5 discusses the integration of Silicon Grass in MEMS. General information about possible integration methods, associated requirements and limitations are given. These range from recommended and/or useful technological processes e.g. the generation of elevated Silicon Grass to appropriate instructions for handling or general design rules.

The possible integration and feasibility of Silicon Grass in MEMS is demonstrated by the technological realization of a thermo-mechanical actuated cantilever. Here, a theoretical investigation shows that the implementation of Silicon Grass leads to a dynamic performance enhancement of the device by introducing an eight-fold increase in thermal conductivity of the compound material in respect to pure

$SU-8$. Depending on the geometrical layout, the maximum operating frequency can be increased by a factor of up to seven times in comparison to an identical cantilever without integrated Silicon Grass.

6.2 Outlook

The presented work establishes fundamental understanding of the Silicon Grass generation in the c-DRIE process and provides the basis for further investigations. These are recommended to deepen the understanding and improve the ways to generate, utilize and optimize the surface modification. In the following, possible additional studies for nanomasking and following structure etching with focus on improving the Silicon Grass for selected applications are covered. In concluding remarks, the important role of ‘Micro-Nano-Integration’ for the utilization of nanotechnology in commercial applications is discussed.

The reproducible and homogeneous initiation of nanomasking, even for various process conditions, is crucial for the implementation of Silicon Grass in different fabrication processes. The etching system utilized should therefore enable a high etching homogeneity, as a radially varying etch rate not only leads to an inhomogeneous initiation but also inhomogeneous structure etching, producing different Silicon Grass geometries. In this context, the influence of secondary effects such as mask geometry and material or carbon dust formation should be eliminated or at least limited.

It is also found that due to the nanomasking by C , leftover carbon and fluorocarbon residues cannot be prevented. Therefore generating Silicon Grass with a minimum of inhibitor material is a goal. Here, a two-step Silicon Grass generation process is suggested: initial nanomask generation via a short process consisting of several cycles and subsequent structure etching with another etching recipe. This etching should then be optimized in order to cause a minimum undercut to prevent the removal of the formed structures, but also to use as little inhibitor as possible. Here, other systems or etching techniques (e.g. cryo-etching) can be used, where other passivation chemistries are utilized. In this regard, it is also beneficial to cause nanomasking by sequencing the process with SF_6/O_2 and using SiO_2 as inhibitor, because it is easier to remove in comparison to C .

Another important research subject should be the utilization of Silicon Grass with adaption to specific applications. Because of the number of different applications of nanostructured surfaces, the properties required often differ from one another. For all applications the structures should exhibit good mechanical stability and flexibility to prevent their disintegration either during processing or their later use. But when comparing the Silicon Grass requirements of e.g. the Nano-velcro[®] and a BioMEMS micro-reactor, it becomes clear that unique sets of optimal combinations of length, thickness, and density of the Silicon Grass exist for both applications. Whereas for the micro-reactor the structures should be as high and as dense as possible to maximize the reactive area, the Nano-Velcro[®] would benefit from pyramidal-shaped structures with a moderate height and density. If, however, the reactor requires

a metallized surface, the Silicon Grass must also be created in order to ensure a proper coverage by enhanced metallization techniques such as ionized PVD or oblique angle deposition. Therefore, the focus should lie on Silicon Grass geometry control in respect to specific applications.

In this work, two examples for adapted Silicon Grass are given: IR optical applications and Silicon Grass bonding, where in both cases a change in geometry leads to different characteristics. In the first case, the strong below-bandgap absorption should be investigated in greater depth to clarify whether it leads to a useful opto-electronic effect. In the other case, a wider selection of Silicon Grass types should be tested in order to improve retention forces and improve long-term stability of the bond.

Another important prospect of Silicon Grass is general sensor enhancement by utilizing the surface enlargement of the structures. Here, bio-sensors (micro-balance measurement) as well as mass-flow sensors (temperature distribution measurement) are particularly considered. In the first case, the number of bio-molecules which can adhere to a resonating element equipped with Silicon Grass can be greatly enhanced. In the latter case, the surface enlargement will greatly improve the convective heat flow from the element, thus increasing the temperature gradient.

Finally, actuators based on the nano-structure are also possible. As an example, a pico-liter microfluidic pump is considered that uses specially coated and electrically contacted Silicon Grass to cycle between the CASSIE-BAXTER and WENZEL states of the fluid on top of the structures. The associated volume change is utilized as the pump stroke and is realized without any moving parts of the device.

The utilization of nanostructures in micro-systems ('Micro-Nano-Integration') is a promising prospect for putting nanotechnology to use in modern day applications. But since most nanotechnology fabrication technologies are bottom-up techniques which have a certain degree of 'randomness' to them, future research projects must focus on controlled generation, manipulation and intelligent integration. Here, Silicon Grass is a good example of this controlled generation and integration.

Effective ways to control and/or manipulate the nanostructures in their nano-scale environment must be found. How is it possible to position and align carbon nano-tubes on their designated electrical contacts without the use of inefficient and costly serial manipulation? The only conceivable way to realize this is the utilization of mass-parallel nano-manipulation by self-organizing processes induced by external fields. That is why self-organizing mechanisms in nano-electronic fabrication processes must be investigated in future works.

Bibliography

- [AA08] AMIROV, II ; ALOV, N. V.: Formation of microstructures on silicon surface in a fluorinated plasma via the cyclic etching-passivation process. In: *High Energy Chemistry* 42 (2008), Nr. 2, S. 132–136
- [AML86] ANDERSON, H. M. ; MERSON, J. A. ; LIGHT, R. W.: A Kinetic-Model for Plasma-Etching Silicon in a SF₆/O₂ Rf Discharge. In: *IEEE Transactions on Plasma Science* 14 (1986), Nr. 2, S. 156–164
- [And07] ANDERS, A.: Metal plasmas for the fabrication of nanostructures. In: *Journal of Physics D-Applied Physics* 40 (2007), Nr. 8, S. 2272–2284
- [AS08] AMIROV, II ; SHUMILOV, A. S.: The mechanism of formation of microneedles on the silicon surface in fluorinated plasma via the cyclic etching-deposition process. In: *High Energy Chemistry* 42 (2008), Nr. 5, S. 399–403
- [aTM08] AMRANI, A. E. ; TADJINE, R. ; MOUSSA, F. Y.: Microstructures Formation by Fluorocarbon Barrel Plasma Etching. In: *International Journal of Plasma Science and Engineering* 2008 (2008), S. 5
- [BK08] BALONIAK, T. ; KEUDELL, A. von: Anomalous roughness scaling of well-ordered amorphous fluorocarbon films deposited from an octafluorocyclobutane plasma. In: *Plasma Processes and Polymers* 5 (2008), Nr. 7, S. 653–660
- [BS03] BESSER, R. S. ; SHIN, W. C.: Deep reactive ion etching characteristics of a macromachined chemical reactor. In: *Journal of Vacuum Science & Technology B* 21 (2003), Nr. 2, S. 912–915
- [BTH⁺98] BURGERS, A.R. ; TOOL, C.J.J. ; HYLTON, J.D. ; WEEBER, A.W. ; VERHOLEN, A.G.B.J. ; GARDENIERS, J.G.E. ; BOER, M.J. d. ; ELWENPOEK, M.C.: Silicon solar cells textured by reactive Ion Etching and processed with screen printing. (1998)
- [CB44] CASSIE, A. B. D. ; BAXTER, S.: Wettability of porous surfaces. In: *Transactions of the Faraday Society* 40 (1944), S. 546 – 551

- [CC04] CHUNG, C. K. ; CHIANG, H. N.: Inverse RIE lag of silicon deep etching. Cambridge : Nano Science & Technology Inst, 2004, S. 481–484
- [CCS⁺04] CROUCH, C. H. ; CAREY, J. E. ; SHEN, M. ; MAZUR, E. ; GENIN, F. Y.: Infrared absorption by sulfur-doped silicon formed by femtosecond laser irradiation. In: *Applied Physics a-Materials Science & Processing* 79 (2004), Nr. 7, S. 1635–1641
- [CCW⁺04] CROUCH, C. H. ; CAREY, J. E. ; WARRENDER, J. M. ; AZIZ, M. J. ; MAZUR, E. ; GENIN, F. Y.: Comparison of structure and properties of femtosecond and nanosecond laser-structured silicon. In: *Applied Physics Letters* 84 (2004), Nr. 11, S. 1850–1852
- [CF54] COLLINS, R. J. ; FAN, H. Y.: Infrared Lattice Absorption Bands in Germanium, Silicon, and Diamond. In: *Physical Review* 93 (1954), Nr. 4, S. 674
- [CKHK06] CHO, Y. H. ; KIM, B. ; HONG, S. K. ; KANG, J. J.: Fabrication and characterization of thermally actuated bimorph probe for living cell measurements with experimental and numerical analysis. In: *Journal of Mechanical Science and Technology* 20 (2006), Nr. 3, S. 297–309
- [CNRW06] CHEUNG, C. L. ; NIKOLIC, R. J. ; REINHARDT, C. E. ; WANG, T. F.: Fabrication of nanopillars by nanosphere lithography. In: *Nanotechnology* 17 (2006), Nr. 5, S. 1339–1343
- [CSW⁺07] CIMALLA, V. ; STUBENRAUCH, M. ; WEISE, F. ; FISCHER, M. ; TONISCH, K. ; HOFFMANN, M. ; AMBACHER, O.: Suspended nanowire web. In: *Applied Physics Letters* 90 (2007), Nr. 10, S. 3
- [CW89] COBURN, J. W. ; WINTERS, H. F.: Conductance Considerations in the Reactive Ion Etching of High Aspect Ratio Features. In: *Applied Physics Letters* 55 (1989), Nr. 26, S. 2730–2732
- [d'A90] D'AGOSTINO, Riccardo: *Plasma deposition, treatment, and etching of polymers*. Bari : Academic Press, Inc., 1990
- [DLM⁺07] DIXIT, P. ; LIN, N. ; MIAO, J. M. ; WONG, W. K. ; TEO, K. C.: Concept and Analytical analysis of Silicon micro/nanopillars based 3-D stacked microchannel heat sink for advanced heat dissipation applications. New York : IEEE, 2007 (Electronic Components and Technology Conference), S. 1149–1154
- [DMT⁺05] DUSSART, R. ; MELLHAOUI, X. ; TILLOCHER, T. ; LEFAUCHEUX, P. ; VOLATIER, M. ; SOCQUET-CLERC, C. ; BRAULT, P. ; RANSON, P.: Silicon columnar microstructures induced by an SF₆/O₂ plasma. In: *Journal of Physics D-Applied Physics* 38 (2005), Nr. 18, S. 3395–3402

-
- [DWSL06] DUC, T. C. ; WEI, J. ; SARRO, P. M. ; LAU, G. K. K.: Integrated silicon-polymer laterally stacked bender for sensing microgrippers. New York : IEEE, 2006, S. 662–665
- [FdP+08] FISCHER, M. ; DETORRES, H. B. ; PAWLOWSKI, B. ; MACH, M. ; GADE, R. ; BARTH, S. ; HOFFMANN, M. ; MUELLER, J.: Silicon on Ceramics - A New Concept for Micro-Nano-Integration on Wafer Level. Boca Raton : Crc Press-Taylor & Francis Group, 2008, S. 157–160
- [FMM+09] FISCHER, C. ; MENEZES, J. W. ; MOSHKALEV, S. A. ; VERISSIMO, C. ; VAZ, A. R. ; SWART, J. W.: Fabrication of high-aspect ratio silicon nanopillars and nanocones using deep reactive ion etching. In: *Journal of Vacuum Science & Technology B* 27 (2009), Nr. 6, S. 2732–2736
- [FZ07] FAN, J. G. ; ZHAO, Y. P.: Spreading of a water droplet on a vertically aligned Si nanorod array surface. In: *Applied Physics Letters* 90 (2007), Nr. 1, S. 3
- [GCG+00] GEHRING, G. A. ; COOKE, M. D. ; GREGORY, I. S. ; KARL, W. J. ; WATTS, R.: Cantilever unified theory and optimization for sensors and actuators. In: *Smart Materials & Structures* 9 (2000), Nr. 6, S. 918–931
- [GD06] GERLACH, Gerald ; DOETZEL, Wolfram: *Einfuehrung in die Mikrosystemtechnik: Ein Kursbuch fuer Studierende*. 1. Auflage (Februar 2006). Hanser Fachbuchverlag, 2006
- [GS06] GHARGHI, M. ; SIVOTHTHAMAN, S.: Formation of nanoscale columnar structures in silicon by a maskless reactive ion etching process. In: *Journal of Vacuum Science & Technology A* 24 (2006), Nr. 3, S. 723–727
- [Har59] HARTLEY, H. O.: Smallest Composite Designs for Quadratic Response Surfaces. In: *Biometrics* 15 (1959), Nr. 4, S. 610–624
- [HFW+98] HER, T. H. ; FINLAY, R. J. ; WU, C. ; DELIWALA, S. ; MAZUR, E.: Microstructuring of silicon with femtosecond laser pulses. In: *Applied Physics Letters* 73 (1998), Nr. 12, S. 1673–1675
- [HG97] HWANG, G. S. ; GIAPIS, K. P.: On the origin of the notching effect during etching in uniform high density plasmas. In: *Journal of Vacuum Science & Technology B* 15 (1997), Nr. 1, S. 70–87
- [HSUM98] HAYAKAWA, T. ; SUZUKI, T. ; UESUGI, T. ; MITSUSHIMA, Y.: Mechanism of residue formation in silicon trench etching using a bromine-based plasma. In: *Japanese Journal of Applied Physics Part 1* 37 (1998), Nr. 1, S. 5–9
- [HT03] HARMER, S. ; TOWNSEND, P. D.: The role of laser surface patterning for enhanced optical absorptance of 'black silicon'. In: *Journal of Modern Optics* 50 (2003), Nr. 2, S. 185–197

- [HYO⁺08] HIMMERLICH, M. ; YANEV, V. ; OPITZ, A. ; KEPPLER, A. ; SCHAEFER, J. A. ; KRISCHOK, S.: Effects of X-ray radiation on the surface chemical composition of plasma deposited thin fluorocarbon films. In: *Polymer Degradation and Stability* 93 (2008), Nr. 3, S. 700–706
- [JBU⁺09] JANSEN, H. V. ; BOER, M. J. ; UNNIKRISHNAN, S. ; LOUWERSE, M. C. ; ELWENSPOEK, M. C.: Black silicon method X: a review on high speed and selective plasma etching of silicon with profile control: an in-depth comparison between Bosch and cryostat DRIE processes as a roadmap to next generation equipment. In: *Journal of Micromechanics and Microengineering* 19 (2009), Nr. 3, S. 41
- [JdE96] JANSEN, H. ; DEBOER, M. ; ELWENSPOEK, M.: The black silicon method 6: High aspect ratio trench etching for MEMS applications. New York : I E E E, 1996 (Proceedings: IEEE Micro Electro Mechanical Systems Workshop), S. 250–257
- [JDLE95] JANSEN, H. ; DEBOER, M. ; LEGTENBERG, R. ; ELWENSPOEK, M.: The Black Silicon Method - a Universal Method for Determining the Parameter Setting of a Fluorine-Based Reactive Ion Etcher in Deep Silicon Trench Etching with Profile Control. In: *Journal of Micromechanics and Microengineering* 5 (1995), Nr. 2, S. 115–120
- [JKC06] JEUNG, Won K. ; KIM, Yong J. ; CHOI, Seog M.: Large Displacement Out-Of-Plane Bimorph Actuator for Optical Application. In: *Key Engineering Materials* Experimental Mechanics in Nano and Biotechnology (2006), S. 3
- [JKJ⁺07] JI, L. ; KIM, J. K. ; JI, Q. ; LEUNG, K. N. ; CHEN, Y. ; GOUGH, R. A.: Conformal metal thin-film coatings in high-aspect-ratio trenches using a self-sputtered rf-driven plasma source. In: *Journal of Vacuum Science & Technology B* 25 (2007), Nr. 4, S. 1227–1230
- [KBE⁺07] KRISCHOK, S. ; BLANK, C. ; ENGEL, M. ; GUTT, R. ; ECKE, G. ; SCHAWOHL, J. ; SPIESS, L. ; SCHREMPEL, F. ; HILDEBRAND, G. ; LIEFEITH, K.: Influence of ion implantation on titanium surfaces for medical applications. In: *Surface Science* 601 (2007), Nr. 18, S. 3856–3860
- [KBS74] KOBAYASHI, H. ; BELL, A. T. ; SHEN, M.: Plasma Polymerization of Saturated and Unsaturated-Hydrocarbons. In: *Macromolecules* 7 (1974), Nr. 3, S. 277–283
- [KBS06] KOYNOV, S. ; BRANDT, M. S. ; STUTZMANN, M.: Black nonreflecting silicon surfaces for solar cells. In: *Applied Physics Letters* 88 (2006), Nr. 20, S. 3
- [KCL⁺03] KIM, B. ; COLLARD, D. ; LAGOUGE, M. ; CONSEIL, F. ; LEGRAND, B. ; BUCHAILLOT, L.: Thermally actuated probe arrays for manipulation and characterization of individual bio-cell. New York : IEEE, 2003, S. 1255–1258

-
- [Kep08] KEPPLER, Angela: Oberflächeneigenschaften und Modifizierung von Polymeren und organischen Funktionsschichten fuer opto-fluidische Mikrosysteme. Diploma Thesis (2008), Ilmenau University of Technology
- [KF99a] KIIHAMAKI, J. ; FRANSSILA, S.: Deep silicon etching in inductively coupled plasma reactor for MEMS. In: *Physica Scripta T79* (1999), S. 250–254
- [KF99b] KIIHAMAKI, J. ; FRANSSILA, S.: Pattern shape effects and artefacts in deep silicon etching. In: *Journal of Vacuum Science & Technology A* 17 (1999), Nr. 4, S. 2280–2285
- [KGCG08] KOKKORIS, G. ; GOODYEAR, A. ; COOKE, M. ; GOGOLIDES, E.: A global model for C4F8 plasmas coupling gas phase and wall surface reaction kinetics. In: *Journal of Physics D-Applied Physics* 41 (2008), Nr. 19, S. 12
- [Kie09] KIESEWETTER, Anja: Elektrische Kontakte auf nanostrukturiertem Silicium. Project Thesis (2009), Ilmenau University of Technology
- [Kii00] KIIHAMAKI, J.: Deceleration of silicon etch rate at high aspect ratios. In: *Journal of Vacuum Science & Technology A* 18 (2000), Nr. 4, S. 1385–1389
- [KL05] KARABACAK, T. ; LU, T. M.: Enhanced step coverage by oblique angle physical vapor deposition. In: *Journal of Applied Physics* 97 (2005), Nr. 12, S. 5
- [KM00] KANECHIKA, M. ; MITSUSHIMA, Y.: Silicon needles fabricated by highly selective anisotropic dry etching and their field emission current characteristics. In: *Japanese Journal of Applied Physics Part 1* 39 (2000), Nr. 12B, S. 7111–7114
- [KNK⁺07] KIM, W. ; NG, J. K. ; KUNITAKE, M. E. ; CONKLIN, B. R. ; YANG, P. D.: Interfacing silicon nanowires with mammalian cells. In: *Journal of the American Chemical Society* 129 (2007), Nr. 23, S. 7228–7229
- [Kre05] KREMIN, Christoph: Kombiniertes form- und kraftschlüssiges Fügeverfahren fuer Silizium. Diploma Thesis (2005), Ilmenau University of Technology
- [KSM02] KANECHIKA, M. ; SUGIMOTO, N. ; MITSUSHIMA, Y.: Control of shape of silicon needles fabricated by highly selective anisotropic dry etching. In: *Journal of Vacuum Science & Technology B* 20 (2002), Nr. 4, S. 1298–1302
- [KWA06] KIM, T. G. ; WARRENDER, J. M. ; AZIZ, M. J.: Strong sub-band-gap infrared absorption in silicon supersaturated with sulfur. In: *Applied Physics Letters* 88 (2006), Nr. 24, S. 3
- [LBMM05] LEE, C. ; BAE, S. Y. ; MOBASSER, S. ; MANOHARA, H.: A novel silicon nanotips antireflection surface for the micro sun sensor. In: *Nano Letters* 5 (2005), Nr. 12, S. 2438–2442

- [LDB⁺04] LABELLE, C. B. ; DONNELLY, V. M. ; BOGART, G. R. ; OPILA, R. L. ; KORNBLIT, A.: Investigation of fluorocarbon plasma deposition from c-C₄F₈ for use as passivation during deep silicon etching. In: *Journal of Vacuum Science & Technology A* 22 (2004), Nr. 6, S. 2500–2507
- [LDG⁺07] LAU, G. K. ; DUC, T. C. ; GOOSEN, J. F. L. ; SARRO, P. M. ; KEULEN, F. van: An in-plane thermal unimorph using confined polymers. In: *Journal of Micromechanics and Microengineering* 17 (2007), Nr. 7, S. S174–S183
- [Leo08] LEOPOLD, S.: Untersuchungen zum Mechanismus der Mikromaskierung bei der Herstellung von nanostrukturierten Siliciumoberflaechen in reaktiven Tiefenaetzprozessen. Diploma Thesis (2008), Ilmenau University of Technology
- [LHE⁺07] LAWS, G. M. ; HANDUGAN, A. ; ESCHRICHT, T. ; BOLAND, P. ; SINCLAIR, C. ; MYHAIJLENKO, S. ; POWELEIT, C. D.: Process characterization of inductively coupled plasma etched silicon nanopillars by micro-Raman. In: *Journal of Vacuum Science & Technology B* 25 (2007), Nr. 6, S. 2059–2063
- [Lid05] LIDE, David R.: *CRC Handbook of Chemistry and Physics*. Internet Version 2005 <http://www.hbcpnetbase.com>. Boca Raton, FL : CRC Press, 2005
- [LJW06] LAI, S. L. ; JOHNSON, D. ; WESTERMAN, R.: Aspect ratio dependent etching lag reduction in deep silicon etch processes. In: *Journal of Vacuum Science & Technology A* 24 (2006), Nr. 4, S. 1283–1288
- [LL05] LIEBERMANN, M. A. ; LICHTENBERG, A. J.: *Principles of Plasma Discharges and Materials Processing*. 2nd Edition. John Wiley & Sons Inc., 2005
- [LLW⁺08] LIU, Y. ; LIU, S. ; WANG, Y. ; FENG, G. ; ZHU, J. ; ZHAO, L.: Broad band enhanced infrared light absorption of a femtosecond laser microstructured silicon. In: *Laser Physics* 18 (2008), Nr. 10, S. 1148–1152
- [LS72] LIEPINS, R. ; SAKAOKU, K.: Submicron Polymer Powder in Electrodeless Radio Frequency-Induced Plasma-Initiated Polymerization. In: *Journal of Applied Polymer Science* 16 (1972), Nr. 10, S. 2633
- [LS96] LAERMER, Franz ; SCHILP, Andrea: US-Patent: Method of Anisotropically Etching Silicon. US005501893A (1996), Robert Bosch GmbH
- [LW80] LEHMANN, H. W. ; WIDMER, R.: Dry Etching for Pattern Transfer. In: *Journal of Vacuum Science & Technology* 17 (1980), Nr. 5, S. 1177–1183
- [MC08] MARTIN, M. ; CUNGE, G.: Surface roughness generated by plasma etching processes of silicon. In: *Journal of Vacuum Science & Technology B* 26 (2008), Nr. 4, S. 1281–1288

-
- [MG70] MAISSEL, Leon I. ; GLANG, Reinhard: *Handbook of Thin Film Technology*. June. Mcgraw-Hill (Tx), 1970
- [MIU04] MORIYA, T. ; ITO, N. ; UESUGI, F.: Capture of flaked particles during plasma etching by a negatively biased electrode. In: *Journal of Vacuum Science & Technology B* 22 (2004), Nr. 5, S. 2359–2363
- [Mon99] MONTEIRO, O. R.: Novel metallization technique for filling 100-nm-wide trenches and vias with very high aspect ratio. In: *Journal of Vacuum Science & Technology B* 17 (1999), Nr. 3, S. 1094–1097
- [MRS⁺05] MARTY, F. ; ROUSSEAU, L. ; SAADANY, B. ; MERCIER, B. ; FRANÇAIS, O. ; MITA, Y. ; BOUROUINA, T.: Advanced etching of silicon based on deep reactive ion etching for silicon high aspect ratio microstructures and three-dimensional micro- and nanostructures. In: *Microelectronics Journal* 36 (2005), Nr. 7, S. 673–677
- [MSSB95] MOULDER, John F. ; STICKLE, William F. ; SOBOL, Peter E. ; BOMBEN, Kenneth D.: *Handbook of X Ray Photoelectron Spectroscopy: A Reference Book of Standard Spectra for Identification and Interpretation of Xps Data*. Reissue. Physical Electronics, 1995
- [Mue08] MUELLER, Lutz: Kopplung polymerer Werkstoffe mit nanostrukturiertem Silicium. Project Thesis (2008), Ilmenau University of Technology
- [Mue10] MUELLER, Lutz: Entwurf und Herstellung eines thermomechanischen Funktionselements auf der Basis von Silicium und SU-8. Diploma Thesis (2010), Ilmenau University of Technology
- [MWM⁺06] MOLONEY, A. M. ; WALL, L. ; MATHEWSON, A. ; HEALY, G. ; JACKSON, J. C.: Novel black silicon PIN photodiodes. Bellingham : SPIE: Int. Soc. Optical Engineering, 2006, S. B1190–B1190
- [OBI09] OK, Z. D. ; BENNEYAN, J. C. ; ISAACS, J. A.: Nanotechnology Environmental, Health, and Safety Issues: Brief Literature Review Since 2000. New York : IEEE, 2009 (IEEE International Symposium on Sustainable Systems and Technology-ISSST), S. 50–54
- [ORP90] OEHRLEIN, G. S. ; REMBETSKI, J. F. ; PAYNE, E. H.: Study of Sidewall Passivation and Microscopic Silicon Roughness Phenomena in Chlorine-Based Reactive Ion Etching of Silicon Trenches. In: *Journal of Vacuum Science & Technology B* 8 (1990), Nr. 6, S. 1199–1211
- [OSJ86] OEHRLEIN, G. S. ; SCHAD, R. G. ; JASO, M. A.: Mechanism of Silicon Surface Roughening by Reactive Ion Etching. In: *Surface and Interface Analysis* 8 (1986), Nr. 6, S. 243–246

- [PG76] PEARSE, R.W.B. ; GAYDON, A.G.: *The identification of molecular spectra*. 4th Edition. New York : John Wiley & Sons, Inc., 1976
- [PKL⁺94] PARK, H. H. ; KWON, K. H. ; LEE, J. L. ; SUH, K. S. ; KWON, O. J. ; CHO, K. I. ; PARK, S. C.: Characterization and Removal of Silicon Surface Residue Resulting from Chf₃/C₂f₆ Reactive Ion Etching. In: *Journal of Applied Physics* 76 (1994), Nr. 8, S. 4596–4602
- [RDM⁺08] ROURNANIE, M. ; DELATTRE, C. ; MITTLER, F. ; MARCHAND, G. ; MEILLE, V. ; BELLEFON, C. de ; PIJOLAT, C. ; TOURNIER, G. ; POUTEAU, P.: Enhancing surface activity in silicon microreactors: Use of black silicon and alumina as catalyst supports for chemical and biological applications. In: *Chemical Engineering Journal* 135 (2008), S. S317–S326
- [RKB⁺05] RENTSCH, J. ; KOHN, N. ; BAMBERG, F. ; ROTH, K. ; PETERS, S. ; LUDEMANN, R. ; PREU, R.: Isotropic plasma texturing of mc-Si for industrial solar cell fabrication. New York : IEEE, 2005 (IEEE Photovoltaic Specialists Conference), S. 1316–1319
- [RKK⁺08] RHEE, H. ; KWON, H. ; KIM, C. K. ; KIM, H. ; YOO, J. ; KIM, Y. W.: Comparison of deep silicon etching using SF₆/C₄F₈ and SF₆/C₄F₆ plasmas in the Bosch process. In: *Journal of Vacuum Science & Technology B* 26 (2008), Nr. 2, S. 576–581
- [RL95] RANGELOW, I. W. ; LOSCHNER, H.: Reactive ion etching for microelectrical mechanical system fabrication. In: *Journal of Vacuum Science & Technology B* 13 (1995), Nr. 6, S. 2394–2399
- [RP90] RYAN, K. R. ; PLUMB, I. C.: A Model for the Etching of Silicon in SF₆/O₂ Plasmas. In: *Plasma Chemistry and Plasma Processing* 10 (1990), Nr. 2, S. 207–229
- [RSB98] ROBBIE, K. ; SIT, J. C. ; BRETT, M. J.: Advanced techniques for glancing angle deposition. In: *Journal of Vacuum Science & Technology B* 16 (1998), Nr. 3, S. 1115–1122
- [RTM⁺86] RANGELOW, I. W. ; THOREN, P. ; MASSELI, K. ; KASSING, R. ; ENGELHARDT, M.: Secondary effects of single crystalline silicon deep-trench etching in a chlorine-containing plasma of 3-dimensional capacitor cells. In: *Microelectronic Engineering* 5 (1986), Nr. 1-4, S. 387–394
- [RZN⁺05] RUBY, D. S. ; ZAIDI, S. ; NARAYANAN, S. ; YAMANAKA, S. ; BALANGA, R.: RIE-texturing of industrial multicrystalline silicon solar cells. In: *Journal of Solar Energy Engineering-Transactions of the Asme* 127 (2005), Nr. 1, S. 146–149
- [SCC⁺03] SHEN, M. Y. ; CROUCH, C. H. ; CAREY, J. E. ; YOUNKIN, R. ; MAZUR, E. ; SHEEHY, M. ; FRIEND, C. M.: Formation of regular arrays of silicon microspikes by femtosecond laser irradiation through a mask. In: *Applied Physics Letters* 82 (2003), Nr. 11, S. 1715–1717

-
- [SFK⁺06] STUBENRAUCH, M. ; FISCHER, M. ; KREMIN, C. ; STOE BENAU, S. ; ALBRECHT, A. ; NAGEL, O.: Black silicon - new functionalities in microsystems. In: *Journal of Micromechanics and Microengineering* 16 (2006), Nr. 6, S. S82–S87
- [SFK⁺07] STUBENRAUCH, M. ; FISCHER, M. ; KREMIN, C. ; HOFFMANN, M. ; MULLER, J.: Bonding of silicon with filled and unfilled polymers based on black silicon. In: *Micro & Nano Letters* 2 (2007), Nr. 1, S. 6–8
- [SFV⁺09] STUBENRAUCH, M. ; FROBER, U. ; VOGES, D. ; SCHILLING, C. ; HOFFMANN, M. ; WITTE, H.: A modular BioMEMS platform for new procedures and experiments in tissue engineering. In: *Journal of Micromechanics and Microengineering* 19 (2009), Nr. 7, S. 6
- [SHJ⁺04] STANDAERT, Tefm ; HEDLUND, C. ; JOSEPH, E. A. ; OEHRLEIN, G. S. ; DALTON, T. J.: Role of fluorocarbon film formation in the etching of silicon, silicon dioxide, silicon nitride, and amorphous hydrogenated silicon carbide. In: *Journal of Vacuum Science & Technology A* 22 (2004), Nr. 1, S. 53–60
- [SKA⁺07] SAINIEMI, L. ; KESKINEN, H. ; AROMAA, M. ; LUOSUJARVI, L. ; GRIGORAS, K. ; KOTI-AHO, T. ; MAKELA, J. M. ; FRANSSILA, S.: Rapid fabrication of high aspect ratio silicon nanopillars for chemical analysis. In: *Nanotechnology* 18 (2007), Nr. 50, S. 7
- [SKT⁺71] SCHUMANN, Jr P. A. ; KEENAN, W. A. ; TONG, A. H. ; GEGENWARTH, H. H. ; SCHNEIDER, C. P.: Silicon Optical Constants in the Infrared. In: *Journal of The Electrochemical Society* 118 (1971), Nr. 1, S. 145–148
- [SLS00] SCHNELL, M. ; LUDEMANN, R. ; SCHAEFER, S.: Plasma surface texturization for multicrystalline silicon solar cells. New York : IEEE, 2000 (IEEE Photovoltaic Specialists Conference), S. 367–370
- [SST98] STOFFELS, W. W. ; STOFFELS, E. ; TACHIBANA, K.: Polymerization of fluorocarbons in reactive ion etching plasmas. In: *Journal of Vacuum Science & Technology A* 16 (1998), Nr. 1, S. 87–95
- [SWK⁺97] SIEMROTH, P. ; WENZEL, C. ; KLIMES, W. ; SCHULTRICH, B. ; SCHULKE, T.: Metallization of sub-micron trenches and vias with high aspect ratio. In: *Thin Solid Films* 308 (1997), S. 455–459
- [SZM⁺06] SCHNARRENBERGER, M. ; ZIMMERMANN, L. ; MITZE, T. ; VOIGT, K. ; BRUNS, J. ; PETERMANN, K.: Concept for an alternative solder-free flip-chip technique on SOI using black-silicon. New York : IEEE, 2006, S. 191–193

- [TCCG99] TESSIER, P. Y. ; CHEVOLLEAU, T. ; CARDINAUD, C. ; GROLEAU, B.: An XPS study of the SF6 reactive ion beam etching of silicon at low temperatures. In: *Nuclear Instruments and Methods in Physics Research Section B* 155 (1999), Nr. 3, S. 280–288
- [THKK97] TADA, T. ; HAMOUDI, A. ; KANAYAMA, T. ; KOGA, K.: Spontaneous production of 10-nm Si structures by plasma etching using self-formed masks. In: *Applied Physics Letters* 70 (1997), Nr. 19, S. 2538–2540
- [TSFG89] THOMAS, D. J. ; SOUTHWORTH, P. ; FLOWERS, M. C. ; GREEF, R.: An Investigation of the Roughening of Silicon(100) Surfaces in Cl2 Reactive Ion Etching Plasmas by Insitu Ellipsometry and Quadrupole Mass-Spectrometry. In: *Journal of Vacuum Science & Technology B* 7 (1989), Nr. 6, S. 1325–1332
- [TT01a] TAKAHASHI, K. ; TACHIBANA, K.: Molecular composition of films and solid particles polymerized in fluorocarbon plasmas. In: *Journal of Applied Physics* 89 (2001), Nr. 2, S. 893–899
- [TT01b] TAKAHASHI, K. ; TACHIBANA, K.: Solid particle production in fluorocarbon plasmas. I. Correlation with polymer film deposition. In: *Journal of Vacuum Science & Technology A* 19 (2001), Nr. 5, S. 2055–2060
- [TT02] TAKAHASHI, K. ; TACHIBANA, K.: Solid particle production in fluorocarbon plasmas II: Gas phase reactions for polymerization. In: *Journal of Vacuum Science & Technology A* 20 (2002), Nr. 2, S. 305–312
- [VHHR99] VOLLAND, B. ; HUDEK, F. S. ; HEERLEIN, H. ; RANGELOW, I. W.: Dry etching with gas chopping without rippled sidewalls. In: *Journal of Vacuum Science & Technology B* 17 (1999), Nr. 6, S. 2768–2771
- [VHKR01] VOLLAND, B. E. ; HEERLEIN, H. ; KOSTIC, I. ; RANGELOW, I. W.: The application of secondary effects in high aspect ratio dry etching for the fabrication of MEMS. In: *Microelectronic Engineering* 57-8 (2001), S. 641–650
- [VLOK04] VASENKOV, A. V. ; LI, X. ; OEHRLEIN, G. S. ; KUSHNER, M. J.: Properties of c-C4F8 inductively coupled plasmas. II. Plasma chemistry and reaction mechanism for modeling of Ar/c-C4F8/O-2 discharges. In: *Journal of Vacuum Science & Technology A* 22 (2004), Nr. 3, S. 511–530
- [WCZ+01] WU, C. ; CROUCH, C. H. ; ZHAO, L. ; CAREY, J. E. ; YOUNKIN, R. ; LEVINSON, J. A. ; MAZUR, E. ; FARRELL, R. M. ; GOTHOSKAR, P. ; KARGER, A.: Near-unity below-band-gap absorption by microstructured silicon. In: *Applied Physics Letters* 78 (2001), Nr. 13, S. 1850–1852

- [WDLS08] WEI, J. ; DUC, T. C. ; LAU, G. K. ; SARRO, P. M.: Novel electrothermal bimorph actuator for large out-of-plane displacement and force. New York : IEEE, 2008 (Proceedings: IEEE Micro Electro Mechanical Systems), S. 46–49
- [Wen36] WENZEL, Robert N.: Resistance of solid surfaces to wetting by water. In: *Industrial & Engineering Chemistry* 28 (1936), Nr. 8, S. 988–994
- [Wer89] WERNSTEDT, Juergen: *Experimentelle Prozessanalyse*. Verlag Technik Berlin, 1989
- [YKO⁺04] YANEV, V. ; KRISCHOK, S. ; OPITZ, A. ; WURMUS, H. ; SCHAEFER, J. A. ; SCHWESINGER, N. ; AHMED, S. I. U.: Influence of the RF power on the deposition rate and the chemical surface composition of fluorocarbon films prepared in dry etching gas plasma. In: *Surface Science* 566 (2004), S. 1229–1233
- [YKT⁺08] YOO, J. ; KIM, K. ; THAMILSELVAN, M. ; LAKSHMINARAYN, N. ; KIM, Y. K. ; LEE, J. ; YOO, K. J. ; YI, J.: RIE texturing optimization for thin c-Si solar cells in SF₆/O₂ plasma. In: *Journal of Physics D-Applied Physics* 41 (2008), Nr. 12, S. 7
- [YPG⁺06] YOO, J. S. ; PARM, I. O. ; GANGOPADHYAY, U. ; KIM, K. ; DHUNGEL, S. K. ; MANGALARAJ, D. ; YI, J. S.: Black silicon layer formation for application in solar cells. In: *Solar Energy Materials and Solar Cells* 90 (2006), Nr. 18-19, S. 3085–3093

List of Figures

2.1	c-DRIE process sequence.	8
2.2	c-DRIE scalloping in trench and hole etching.	9
2.3	Main reaction paths of SF_6/O_2 plasmas.	10
2.4	Main reaction paths of C_4F_8 plasmas.	11
2.5	Cylindrical and planar ICP coil configuration.	12
2.6	ICP-multiplex from STS.	13
2.7	Radial variation of etch rate of the ICP-multiplex.	15
2.8	RIE-lag, Bowing and Tilting	16
2.9	RIE and c-DRIE Silicon Grass.	19
2.10	Applications of Silicon Grass.	21
3.1	Silicon Grass formation in c-DRIE processes	26
3.2	SEM of the nanomask after one cycle.	28
3.3	SEM of the nanomask after two cycles.	28
3.4	SEM of the nanomask after five cycles.	28
3.5	SEM of the nanomask after five cycles with coarser structures (45° view).	29
3.6	AFM of the nanomask after two, five and 15 cycles.	29
3.7	Radial inhomogeneity of the nanomask.	30
3.8	XPS measurement overview of the nanomask and a solid FC-film.	32
3.9	F1s peak comparison of the nanomask and a solid FC-film.	33
3.10	C1s peak comparison of the nanomask and a solid FC-film.	33
3.11	AES analysis of the nanomask and a thin solid FC-film.	35
3.12	Elemental area-scan for C and S of the nanomask.	36
3.13	Temperature shifts occurring during Silicon Grass generation in c-DRIE etching.	37
3.14	Illustration of the early phase of the Silicon Grass generation process.	38
3.15	OES spectra of C_4F_8 at different pressure p and coil power P_c settings.	40
3.16	OES spectra of C_4F_8 at different passivation settings.	41
3.17	XPS C1s spectra of FC-films deposited at different passivation settings.	42
3.18	AFM scan of deposited FC-film.	43
3.19	Deposition rate R_{dep} as a function of coil power P_c , pressure p and substrate temperature T_s	44

3.20	Sketch of morphological change of the FC-film at the end of the etching step.	45
3.21	Change in reflection at the end of the etching step.	46
3.22	OES spectra of FC-film and oxide etching with SF_6	47
3.23	$F(703.8\text{ nm})$ and $CS(257.6\text{ nm})$ emissions during etching for the Silicon Grass and the c-DRIE process.	48
3.24	$F(703.8\text{ nm})$ and $CS(257.6\text{ nm})$ emissions during etching FC-films deposited at different passivation settings.	49
3.25	FC-film etch rate as a function of bias power P_b and corresponding bias voltage U_b . . .	50
3.26	Critical etch time τ_{crit} as function of deposition time τ_{dep} and bias voltage U_b	52
3.27	Critical etch time τ_{crit} as function of coil power P_c	53
3.28	Three-dimensional experimental space.	56
3.29	Measurement procedure.	57
3.30	Different morphologies after the five cycle nanomasking process.	58
3.31	Dependencies of τ_{dep} , P_c and P_b on nanomask density	59
3.32	SEM images of an non-uniformly etched FC-film in the vicinity of the clamping ring. .	62
3.33	SEM images of carbon dust particles after five cycles and the resulting Silicon Grass structures after 75 cycles.	62
3.34	SEM images of HF treated wafers after two cycles and 75 cycles.	63
3.35	SEM images of Silicon Grass substrates masked by Fotor resist and AlN	65
4.1	Sketch of working point progressions resulting in different Silicon Grass geometries. . .	68
4.2	Sketch of Silicon Grass property measurements.	71
4.3	Progression of Silicon Grass height h and density D throughout the process.	72
4.4	Influence of the deposition step time τ_{dep} on Silicon Grass height h and density D . . .	74
4.5	Different Silicon Grass with $\tau_{dep}/\tau_{etch} = 7\text{ s}/6\text{ s}$, $11\text{ s}/9\text{ s}$ and $15\text{ s}/12\text{ s}$	74
4.6	Influence of bias power P_b on Silicon Grass height h and density D	75
4.7	Different Silicon Grass types from processes with different values for P_b	76
4.8	Effect on sidewall scallops by a variation of physical lateral etching.	77
4.9	Sputtered Al on Silicon Grass.	79
4.10	Sputtered Ti/Au on Silicon Grass.	79
4.11	TEM analysis on Silicon Grass needle with 200 nm sputtered Al	80
4.12	TEM analysis on Silicon Grass needle with 200 nm sputtered Au	80
4.13	Effect of scalloping on the uniformity of a sputtered Au film.	81
4.14	Metallized Silicon Grass by Ni electroless plating.	83
4.15	Metallized Silicon Grass by Ag electroless plating.	83
4.16	Metallized Silicon Grass by Cu electroless plating.	84
4.17	Different types of Silicon Grass.	85



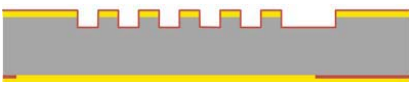
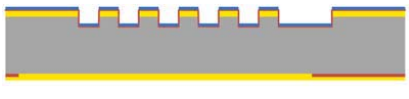
4.18	Pull test of the Nano-Velcro [®] and shear test of the Silicon-Polymer bond with different types of Silicon Grass.	87
4.19	SEM image of a sheared off <i>SU</i> –8 pylon.	88
4.20	Transmission of different Silicon Grass samples.	89
4.21	Reflection of different Silicon Grass samples.	90
4.22	Absorption \mathcal{A} of the samples.	91
4.23	Extinction coefficient of the different Silicon Grass types.	92
5.1	Back-end of a flow chart for a highly-integrated biosensor device with enlarged-surface electrical contacts.	93
5.2	Fabrication methods of elevated Silicon Grass.	95
5.3	Sketch of thermo-mechanical actuated bimorph cantilever based on <i>Si</i> and <i>SU</i> –8.	99
5.4	Sketch of the layer construction with heat flows for the <i>Si/SU</i> –8 cantilever	101
5.5	Thermal network model.	101
5.6	Plot of the thermal resistances of the cantilever.	102
5.7	Influence of a varying thickness ratio $t_1 t_2^{-1}$ and cantilever length l on the operating frequency f and the maximum deflection R^{-1}	104
5.8	Sketch of the thermal model to approximate λ_{SG}	105
5.9	Dynamic enhancement of different cantilevers.	107
5.10	Simplified technological flowchart for the fabrication of the thermo-mechanical actuated bimorph cantilever.	108
5.11	Cantilevers fabricated with different geometrical layouts.	109

List of Tables


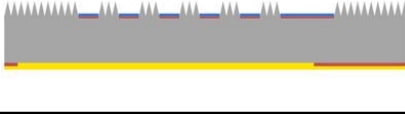
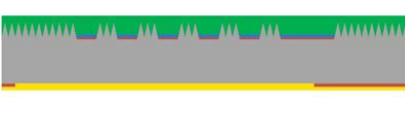


2.1	System parameters.	13
2.2	Typical geometrical properties of Silicon Grass from RIE and c-DRIE.	20
3.1	Silicon Grass generation process parameters.	27
3.2	AFM results characterizing the nanomask.	30
3.3	Comparison of process parameters of the nanomask and a solid FC-film.	31
3.4	Elemental composition of the nanomask and a solid FC-film.	34
3.5	Silicon Grass and normal c-DRIE process parameters.	48
3.6	Experimental table.	55
3.7	Calculated model parameters.	58
4.1	Sputter parameters for <i>Al</i> and <i>Au</i> of the LS 250 EF system.	78
4.2	Characteristic geometrical properties of the different Silicon Grass types.	85
B.1	Chemicals	138

Appendix A – Flowchart Cantilever

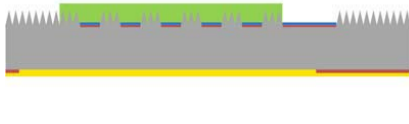

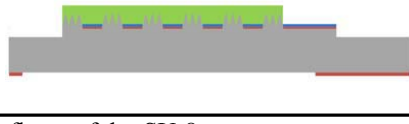
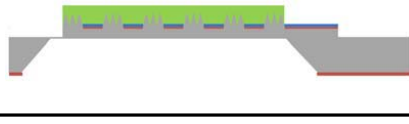
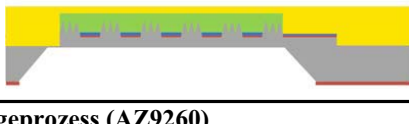
Prozessplan ZMN

Nr. 5	Nasschemie Prozess: Lack entfernen + Reinigung			
Vorgaben:	Entfernung des Schutzlacks + Caro'sche Reinigung			
Bemerkung:				
Bearbeitung:	Datum:	Name:	Gebucht:	
Nr. 6	Lithografie Prozess: Maskierung Vorderseite und Schutzlack Rückseite			
Vorgaben:	Maske: BSi_Cantilever_Metallisierung_LMueller (Halbmaske) Bottomjustage!; Lack: AZ9260; 6µm Lackdicke Rückseitenschutzlack zum Schutz vor Plasmaumgriff ICP!			
Messungen:	keine			
Bemerkung:				
Bearbeitung:	Datum:	Name:	Gebucht:	
Nr. 7	Plasmalabor Prozess: Trockenätzen (ICP)			
Vorgaben:	6' SPEC_B zur Tiefenätzung (Temperatur kontrollieren!) --> Ätztiefe kontrollieren! ca. 20µm (Messung:26µm)			
Messungen:	Messung Ätztiefe			
Bemerkung:				
Bearbeitung:	Datum:	Name:	Gebucht:	
Nr. 8	Plasmalabor Prozess: Nitridabscheidung (ICPCVD)			
Vorgaben:	ca.50nm (Rate ~15 nm/min)			
Messungen:	keine			
Bearbeitung:	Datum:	Name:	Gebucht:	
Nr. 9	Plasmalabor Prozess: Metallisierung (Bedampfen) Ardenne			
Vorgaben:	Cr: ca.10nm;; Ni: ca. 300nm (Rate ~0.25 nm/s)			
Messungen:	keine			
Bearbeitung:	Datum:	Name:	Gebucht:	
Nr. 10	Nasschemie Prozess: Lift-Off			
Vorgaben:	Aceton 10'			
Messungen:	Mikroskopie ob Metall vollständig entfernt, Messung Heizwiderstände			
Bemerkung:				
Bearbeitung:	Datum:	Name:	Gebucht:	




Prozessplan ZMN

Nr. 11	Lithografie Prozess: Schutzlack Rückseite			
Vorgaben:	Rückseitenschutzlack zum Schutz vor Plasmaumgriff ICP! (AZ1518)			
Bemerkung:				
Bearbeitung:	Datum:	Name:	Gebucht:	
Nr. 12	Plasmalabor Prozess: Erzeugung Silicon Grass (ICP)			
Vorgaben:	Standardtyp: BS2 75; vorher Anlage konditionieren: 10' BS2 mit Dummy Mit Ring!			
Messungen:	keine			
Bearbeitung:	Datum:	Name:	Gebucht:	
Nr. 13	Lithografie Prozess: SU-8 2010 Spin-On			
Vorgaben:	2 Schichten SU-8 2005 (Pipette) + 2 Schichten SU-8 2010 (direkt aus Flasche; rel. viel) ramp 10s@250rpm/s --> 2500rpm schleudern für 25s Leveling: 10min/Schicht; Softbake: SU-8 2005: 90s@90°C; SU-8 2010: 180s@95°C			
Messungen:	keine			
Bemerkung:				
Bearbeitung:	Datum:	Name:	Gebucht:	
Nr. 14	Lithografie Prozess: SU-8 Belichtung & PEB			
Vorgaben:	Maske: BSi_Cantilever_SU8_LMueller (Halbmaske) Ohne I-Linien-Filter! UV-Filter benutzen! (Glaswafer beschichtet mit SU-8) --> vorher ausmessen HardContact; Dosis: 500mJ/cm² (z.B. 120s@4,2mW); Bottomjustage! PEB: Rampe zur Stressreduktion: in 20' auf 85°C, 30' halten, in 30' auf 20°C abkühlen			
Messungen:	keine			
Bemerkung:				
Bearbeitung:	Datum:	Name:	Gebucht:	
Nr. 15	Nasschemie Prozess: SU-8 Entwicklung			
Vorgaben:	5min in PGMEA Rinse in IPA (sehr gründlich!); Spülen in Di H2O; Trocknen			
Messungen:	Sichtkontrolle Lichtmikroskop, Messung Dicke SU8 mit Fokussmessung			
Bemerkung:				
Bearbeitung:	Datum:	Name:	Gebucht:	

Prozessplan ZMN

Nr. 16	Lithografie Prozess: Schutzlack Rückseite			
Vorgaben:	Rückseitenschutzlack zum Schutz vor Plasmaumgriff ICP! (AZ1518)			
Bemerkung:				
Bearbeitung:	Datum:	Name:	Gebucht:	
Nr. 17	Plasmalabor Prozess: Trockenätzen (ICP), Entfernung restliches SG und Tiefenstrukturierung			
Vorgaben:	5' O2-Cleaning; ca. 10' Si_ISO_3 Temperatur kontrollieren! Ätztiefe kontrollieren! ca. 25µm bzw. 10µm unterhalb der Metallisierung			
Messungen:	Messung Ätztiefe; Untersuchung des SU8 auf Beschädigungen			
Bemerkung:				
Bearbeitung:	Datum:	Name:	Gebucht:	
Nr. 18	Nasschemie Prozess: Lack entfernen			
Vorgaben:	Entfernung des Schutzlacks (Rückseite) ohne Einfluss auf das SU-8			
Bemerkung:				
Bearbeitung:	Datum:	Name:	Gebucht:	
Nr. 19	Messlabor Prozess: Vermessung des Waferprofils (FRT)			
Vorgaben:	Vermessung der Waferdicke, Ermittlung der dünnsten Stelle und Dickenschwankung			
Messungen:	s.o.			
Bemerkung:				
Bearbeitung:	Datum:	Name:	Gebucht:	
Nr. 20	Nasschemie Prozess: KOH Tiefenätzen			
Vorgaben:	mit Einseitenätzvorrichtung bis ca. 10µm vorm Durchätzen (ca. 270µm, entsprechend der gemessenen Dicke)			
Messungen:	Messung der Ätztiefe (Fokussmessung Lichtmikroskop), ggf. Nachätzen			
Bemerkung:				
Bearbeitung:	Datum:	Name:	Gebucht:	
Nr. 21	Lithografie Prozess: Schutzlack Vorderseite			
Vorgaben:	Schutzlack zum Schutz vor Einflüssen des Sägeprozess (AZ9260)			
Bemerkung:				
Bearbeitung:	Datum:	Name:	Gebucht:	

Prozessplan ZMN

Nr. 22	Prozess: Vereinzelung (Sägen)		
Vorgaben:	Sägen in Einzelchips; UV-lösliche Sägefolie benutzen!		
Messungen:	keine		
Bemerkung:			
Bearbeitung:	Datum:	Name:	Gebucht:
Nr. 23	Nasschemie Prozess: Entfernung Schutzlack		
Vorgaben:	Entfernung des Schutzlackes ohne Angriff des SU-8 Vorsicht: dünne Membranen (10µm)		
Messungen:	keine		
Bemerkung:			
Bearbeitung:	Datum:	Name:	Gebucht:
Nr. 24	Plasmalabor Prozess: Freiätzen (ICP)		
Vorgaben:	20' Dil_etchy + je 5' (falls nötig); ca. 10µm bzw. bis die Cantilever vollständig freigeätzt sind; Von der Rückseite; Tragwafer verwenden; Temperaturwert beachten		
Messungen:	keine		
Bemerkung:			
Bearbeitung:	Datum:	Name:	Gebucht:

Appendix B – Chemicals

Table B.1: Chemicals [Lid05].

Formula	Name	CAS	mass (g/mol)	density (kg/m ³)*	melting point (°C)	boiling point (°C)	Description
$AgNO_3$	Silver(I)nitrate	7761-88-8	168.87	4350	212	400°C	crystal
Al_2O_3	Aluminium oxide (corundum)	1344-28-1	101.96	3970	2053	≈ 3000°C	crystal
AlF_3	Aluminium fluoride	7784-18-1	83.98	3100	≈ 2250 (220.MPa)	1276°C (sublimation)	crystal
AlN	Aluminium nitride	24304-00-5	40.99	3255	3000	-	crystal
C_2F_6	Hexafluoroethane	76-16-4	138.01	1590 (-78°C)	-100.5	-78.1	precursor gas
C_3F_6	Perfluoropropene	116-15-4	150.02	1583 (-40°C)	-156.5	-29.6	precursor gas
C_4F_6	Hexafluoro-1,3-butadiene	685-63-2	162.03	1553 (-20°C)	-132	6	precursor gas
C_4F_8	Octafluorocyclobutane	115-25-3	200.03	1654 (-20°C)	-40.19	-5.9	precursor gas
C_5F_8	Perfluorocyclopentene	559-40-0	212.04	1580 (20°C)	< -70	27	liquid, precursor gas
$C_6H_{12}O_6$	α - D-Glucose, sugar	26655-34-5	180.16	1562 (18°C)	146	-	crystal
CF_4	Tetrafluoromethane	75-73-0	88.01	3034 (25°C)	-183.6	-128	precursor gas
CHF_3	Trifluoromethane	75-46-7	70.01	672 (25°C)	-155.2	-82.1	precursor gas
CO	Carbon monoxide	630-08-0	28.01	1145 g/L	-205.02	-191.5	gas
CO_2	Carbon dioxide	124-38-9	44.01	1799 g/L	-56.56 (triple point)	-78.4 (sublimation)	gas
COF_2	Carbonyl fluoride	353-50-4	66.01	2698 g/L	-111.26	-84.57	gas
CS_2	Carbon disulfide	75-15-0	73.14	1263	-112.1	46	liquid
FO_2	Fluorine monoxide	7783-41-7	54.00	2207 g/L	-223.8	-144.75	gas
H_2O	Water	7732-18-5	18.02	997	0	100	liquid
H_2SO_5	Peroxyulfuric acid, Caro's acid	7722-86-3	114.08	-	45	-	crystal, cleaning (+H ₂ O)
HCl	Hydrogen chloride	7647-01-0	36.46	1490 g/L	-114.2	-85	gas, metal etching (+H ₂ O)
HF	Hydrogen fluoride	766439-3	20.01	818 g/L	-83.35	20	gas, SiO ₂ etching (+H ₂ O)
KOH	Potassium hydroxide	1310-58-3	56.11	2044	406	1327	crystal, Si etching (+H ₂ O)
$NaOH$	Sodium hydroxide	1310-73-2	40.00	2130	323	1388	crystal, cleaning (+H ₂ O)
NH_3	Ammonia	7664-41-7	17.03	696 g/L	-77.73	-33.33	gas
O_2	Oxygen	7782-44-7	32.00	1308 g/L	-218.79	-182.95	gas
SF_6	Sulfur hexafluoride	2551-62-4	146.06	5970 g/L	-50.7 (triple point)	-63.8 (sublimation)	precursor gas
SiF_4	Tetrafluorosilane	7783-61-1	104.08	4254 g/L	-90.2	-86	gas
SiO_2	Silicon dioxide (α -quartz)	14808-60-7	60.09	2648	573 (to β -quartz)	2950	crystal
SiO_2	Silicon dioxide (β -quartz)	14808-60-7	60.09	2533 (500°C)	867 (to tridymite)	2950	crystal
SiO_2	Silicon dioxide (tridymite)	15468-32-3	60.09	2265	1470 (to cristobalite)	2950	crystal
SiO_2	Silicon dioxide (cristobalite)	14464-46-1	60.09	2334	1722	2950	crystal
SiO_2	Silicon dioxide (vitreous)	60676-86-0	60.09	2196	1713	2950	amorph
SO_2	Sulfur dioxide	7446-09-5	64.07	2619 g/L	-75.5	-10.05	gas
SOF_2	Thionyl fluoride	7783-8	86.06	3518 g/L	-129.5	-43.8	gas

* at 20°C, p = 1 atm

Appendix C – Theses

C.1 Theses

- Silicon Grass is a nano-scale surface modification, that can be actively used to enable new functionalities in, or enhance the performance of Micro-Electro-Mechanical-Systems (MEMS), Biological MEMS (BioMEMS) or Micro-Opto-Electro-Mechanical-Systems (MOEMS). It can be cost-effectively fabricated with standard MEMS fabrication equipment.
- Silicon Grass generation in the cyclic Deep Reactive ion Etching (*c*-DRIE) process is initiated by nanomasking, a self-organized process, that can be induced under specific plasma conditions.
- Nanomasking is caused by various mechanisms. In order to reproducibly generate it on *Si*, a variant must be selected which can be governed. This is achieved by the controlled abrasion of the inhibiting film in the etching step, at a setting where etching and passivating are close to equilibrium.
- Reproducible nanomasking can be controlled using the $F(703.8\text{ nm})$ emission line by OES as an indicator for adjusting the time constants of the process.
- The nanomask consists of carbon-rich, filament-like clusters with a low FC-ratio ($R_{FC} = 0.38$) which exhibit a high thermal and chemical resistance.
- The initial morphology of the nanomask is defined by the morphology and laterally varying chemical composition of the deposited FC-film and can be influenced by varying the process parameters deposition step time t_{dep} , coil power P_c and bias power P_b .
- The phenomenon of carbon dust formation in C_4F_8 polymerizing plasmas greatly affects nanomasking when the macro molecules are incorporated in the FC-film.
- The generation and morphology of the nanomask is affected when the ratio of etching to passivating is changed. This is caused by addition of O_2 as a precursor gas, the presence of an initial natural oxide film, wafer and chamber conditions and the utilization of a mask.
- Once nanomasking has caused a certain surface roughness, the morphology develops into the needle-like structures as part of the process.

- The resulting profile of the Silicon Grass can be changed by manipulating process time, deposition step time t_{dep} and bias power P_b . It is possible to generate Silicon Grass with heights from $0.5-30 \mu m$, densities from $10-1 \mu m^{-2}$ and smooth or scalloped sidewalls.
- Subsequent modification of the Silicon Grass by metallization, thermal oxidation and coating with a fluorocarbon film is feasible for adapting the structures for specific applications.
- Silicon Grass for bonding applications benefits from a high surface area as well as a smooth transition region between structures and the bulk *Si*.
- Silicon Grass has index matching properties and exhibits broad-band anti-reflecting properties in the long-wavelength and far infrared (IR). In the short- and mid-wavelength IR it shows a high level of absorption dependent on the Silicon Grass type.
- The feasibility of Silicon Grass integration is demonstrated by the realization of a thermo-mechanically actuated cantilever based on *Si* and *SU-8*.
- Silicon Grass introduces an eight-fold increase in thermal conductivity of a compound material layer consisting of *SU-8* filled Silicon Grass in comparison with pure *SU-8*. This can be utilized to enhance the dynamic performance of thermo-mechanical devices based on a combination of *Si* and polymers.

C.2 Thesen

- Siliciumgras ist eine nano-scalige Oberflächenmodifikation, welche aktiv eingesetzt werden kann um neue Funktionalitäten zu ermöglichen oder die Effizienz von Mikro-Elektro-Mechanischen-Systemen (MEMS), Biologischen MEMS (BioMEMS) oder Mikro-Opto-Electro-Mechanischen-Systemen (MOEMS) zu verbessern. Sie kann kostengünstig mit handelsüblichen Ätzanlagen hergestellt werden.
- Die Bildung von Siliciumgras im zyklischen reaktiven Iontiefenätzprozess wird von einer Nanomaskierung initiiert, welche selbstorganisiert entsteht und unter bestimmten Bedingungen im Plasma erzeugt werden kann.
- Die Nanomaskierung wird durch verschiedene Mechanismen hervorgerufen. Um sie reproduzierbar auf *Si* zu erzeugen, muss ein Mechanismus gewählt werden, welcher sich steuern lässt. Dies wird durch den kontrollierten Abtrag des abgeschiedenen Fluor-Kohlenstofffilms (FC-Film) im Ätzschritt erreicht. Dabei befinden sich Ätzen und Passivieren in der Nähe des Gleichgewichtszustandes.
- Der Nanomaskierungsprozess kann kontrolliert werden, indem man mittels OES die Emissionslinie des Fluor $F(703.8nm)$ als Indikator nutzt, um die Zeitkonstanten des Prozesses einzustellen.
- Die Nanomaskierung besteht aus kohlenstoffreichen, filamentartigen Clustern, die ein niedriges Fluor-Kohlenstoff-Verhältnis ($R_{FC} = 0.38$) sowie eine hohe thermische und chemische Stabilität aufweisen.
- Die Morphologie der Nanomaskierung geht aus der Morphologie und der lateral variierenden chemischen Zusammensetzung des abgeschiedenen FC-films hervor und kann durch eine Änderung der Prozessparameter Passivierungsschrittdauer τ_{dep} , Spulenleistung P_c und Biasleistung P_b beeinflusst werden.
- Das Phänomen der Kohlenstoffpartikelerzeugung in C_4F_8 polymerisierenden Plasmen hat einen starken Einfluss auf den Nanomaskierungsprozess, wenn die Makromoleküle in den FC-Film eingebaut werden.
- Die Erzeugung und Morphologie der Nanomaskierung wird durch eine Änderung des Verhältnisses zwischen Ätzen und Passivieren beeinflusst. Dies wird durch das Hinzufügen von O_2 als Precursor-Gas, die Existenz eines natürlichen Oxidfilms, den Wafer- und Kammerzustand sowie durch die Verwendung einer Maske beeinflusst.
- Sobald die Nanomaskierung eine bestimmte Oberflächenrauigkeit erzeugt hat, entwickelt sich die Morphologie während des Prozesses hin zu nadelförmigen Strukturen.

- Das resultierende Profil des Siliciumgrases kann durch die Prozesszeit, Passivierungsschrittdauer τ_{dep} und Biasleistung P_b verändert werden. Es ist möglich, Siliciumgras mit einer Höhe von $0.5\text{--}30\mu\text{m}$, einer Dichte von $10\text{--}1\mu\text{m}^{-2}$ und mit glatten oder gerippten Seitewänden herzustellen.
- Die nachfolgende Modifizierung von Siliciumgras durch Metallisieren, thermische Oxidation und Beschichtung mit einem Fluorkohlenstofffilm ist realisierbar, um die Strukturen an spezielle Anwendungen anzupassen.
- Für Aufbau- und Verbindungstechniken eignet sich Siliciumgras mit einer großen freien Oberfläche und einem graduellen Übergang zwischen den Strukturen und dem *Si* Bulkmaterial.
- Siliciumgras passt die Brechzahl von Silicium zu Luft an und besitzt eine breitbandige, entspiegelnde Wirkung im Bereich des langwelligen und fernen Infrarot. Im Bereich des kurzwelligen und mittleren Infrarots zeigt es ein ausgeprägtes Absorptionsverhalten abhängig vom verwendeten Siliciumgrastyp.
- Die Durchführbarkeit einer Integration von Siliciumgras wird anhand der Realisierung eines thermo-mechanisch aktuierten Cantilevers auf der Materialbasis von *Si* und *SU-8* demonstriert.
- Durch das Siliciumgras wird eine acht-fache Erhöhung der thermischen Leitfähigkeit der Lage des Verbundstoffmaterials aus *SU-8* gefülltem Siliciumgras im Vergleich zu reinem *SU-8* erzielt. Dies kann zur Verbesserung der dynamischen Eigenschaften von thermomechanischen Funktionselementen genutzt werden, welche auf einer Materialkombination aus *Si* und Polymeren basieren.